Flow and transport of colloidal suspensions in porous media

Von der Fakultät Mathematik und Physik der Universität Stuttgart
zur Erlangung der Würde eines Doktors der Naturwissenschaften (Dr. rer. nat.)
genehmigte Abhandlung

vorgelegt von

Frank Wirner

aus Zell-Weierbach

Hauptberichter: Prof. Dr. Clemens Bechinger
Mitberichter: Prof. Dr. Wolfgang Bolse

Tag der mündlichen Prüfung: 4. Mai 2015

Physikalisches Institut der Universität Stuttgart

2015

Contents

List of Figures

Abstract

Porous media are encountered in several areas of science and technology. The list of examples where flow and transport processes inside complex pore structures are of importance is long and includes topics like groundwater flow, blood perfusion inside the human body and oil recovery. The common and interesting feature of all porous media is their highly complicated pore structure. As the Navier-Stokes equations in such a complex structure are not easily solvable, it is a demanding task to predict flow and transport properties of a porous medium.

The present thesis deals with the effect of the pore geometry on the flow and transport properties of colloidal suspensions. The porous structures used in this work are created by soft lithography. Therefore, the precise microscopic structure of these porous media is known and can be varied in a controlled way. The aqueous colloidal suspensions are used, on one hand, to visualize the flow of the fluid and, on the other hand, to directly study the transport of individual colloids.

First, the relation between the velocity of the colloids and the fluid is investigated. Since the particles are of finite size, they will alter the surrounding flow field and, thus, their velocity at their center of mass is, in general, different from the velocity of the fluid at that point. The determination of the permeability of porous structures is achieved by calibrating the relation between mean particle and mean fluid velocity by adding an additional reference channel with known permeability and, consequently, known mean fluid velocity.

Second, this calibration method is used to measure the permeabilities of two series of porous structures which are composed of randomly placed overlapping circles or ellipses (following Boolean models). An empirical expression for the permeability which makes use of purely structural parameters, namely the Euler Characteristic and the critical pore diameter, is introduced. The values predicted by this expression agree very well with the measured permeabilities. The advantage of this expression is that it does rely neither on the conductivity nor on the percolation threshold of the structures. In order to test whether the proposed empirical expression can be applied universally, two more series of porous structures, where the conducting and obstacle phase have been exchanged, are measured. It is found that for this class of structures the agreement is worse and possible explanations for the deviations are given.

Third, the distribution of transit times of small particles in porous media with different porosities is studied by a combination of experiment and simulation. Since the velocities in different parts of the porous medium vary widely and particles in structures with low porosities can also get trapped in stagnant parts from which they can only escape by diffusion, the resulting distributions can be very wide. The longest transit times of the distributions can be related to a mean escape time for the largest stagnant parts which

implies that information about the extent of stagnant parts can be gathered from the distribution. In addition, the simulations were also modified to account for particles with self-propulsion. The motility of the particles leads to an increase of the shortest observed transit times as well as to a decrease in the longest transit times.

Zusammenfassung

Poröse Medien findet man in vielen Bereichen von Wissenschaft und Technik. Die Liste von Beispielen, für die Fluss- und Transportprozesse in komplizierten porösen Strukturen von Bedeutung sind, ist lang und beinhaltet Themen wie Grundwasserfluss, Blutdurchströmung im menschlichen Körper oder Ölförderung. Das gemeinsame und interessante Merkmal aller porösen Medien ist ihre hochkomplizierte Porenstruktur. Da die Navier-Stokes-Gleichungen in solch einer komplexen Struktur nicht einfach lösbar sind, ist es eine anspruchsvolle Aufgabe, die Fluss- und Transporteigenschaften eines porösen Mediums vorherzusagen.

Die vorliegende Arbeit befasst sich mit der Auswirkung der Porengeometrie auf die Fluss- und Transporteigenschaften kolloidaler Suspensionen. Die porösen Strukturen, die in dieser Arbeit verwendet werden, werden mittels Soft Lithography hergestellt. Folglich ist die genaue mikroskopische Struktur dieser porösen Medien bekannt und kann auf kontrollierte Art variiert werden. Die wässrigen kolloidalen Suspensionen werden einerseits verwendet, um den Fluss des Fluids sichtbar zu machen und andererseits, um den Transport einzelner Kolloide direkt zu untersuchen.

Zuerst wird das Verhältnis zwischen der Geschwindigkeit der Kolloide und des Fluids untersucht. Da die Partikel eine endliche Größe haben, werden sie das sie umgebende Flussfeld beeinflussen und folglich wird sich die Geschwindigkeit ihres Schwerpunkts im Allgemeinen von der Geschwindigkeit des Fluids an diesem Punkt unterscheiden. Die Bestimmung der Permeabilität poröser Strukturen wird erreicht, indem das Verhältnis von mittlerer Teilchengeschwindigkeit und mittlerer Flussgeschwindigkeit durch Hinzufgen eines Referenzkanals mit bekannter Permeabilität und damit bekannter mittlerer Flussgeschwindigkeit kalibriert wird.

Als zweites wird diese Kalibrierungsmethode eingesetzt, um die Permeabilitäten von zwei Serien poröser Strukturen, die aus zufällig platzierten überlappenden Kreisen oder Ellipsen (Booleschen Modellen folgend) bestehen, zu bestimmen. Ein empirischer Ausdruck für die Permeabilität, der rein strukturelle Parameter benutzt, namentlich die Euler-Charakteristik und den kritischen Porendurchmesser, wird eingeführt. Die Werte, die von diesem Ausdruck vorhergesagt werden, stimmen sehr gut mit den gemessenen Permeabilitäten überein. Der Vorteil dieses Ausdrucks liegt darin, dass er weder von der Leitfähigkeit noch von der Perkolationsschwelle der Strukturen abhängt. Um zu überprüfen, ob der vorgeschlagene empirische Ausdruck universell anwendbar ist, werden zwei weitere Serien poröser Strukturen gemessen, bei denen die leitende und die Hindernisphase ausgetauscht wurden. Es wird festgestellt, dass die Übereinstimmung für diese Klasse von Strukturen schlechter ist und es werden mögliche Erklärungen für diese Abweichungen gegeben.

Als drittes wird die Verteilung von Durchlaufzeiten kleiner Teilchen in porösen Medien

mit unterschiedlichen Porositäten mit einer Kombination aus Experiment und Simulation untersucht. Da die Geschwindigkeiten in unterschiedlichen Bereichen des porösen Mediums stark variieren und Partikel in Strukturen mit niedrigen Porositäten auch in stagnierenden Bereichen, aus denen sie nur durch Diffusion wieder entkommen können, gefangen werden können, können die resultierenden Verteilungen sehr breit sein. Die längsten Durchlaufzeiten der Verteilungen können mit der mittleren Entweichzeit der größten stagnierenden Bereiche in Zusammenhang gebracht werden, was bedeutet, dass Information über das Ausmaß der stagnierenden Bereiche von den Verteilungen gewonnen werden kann. Zusätzlich wurden die Simulationen auch angepasst, um Partikel mit Selbstantrieb zu berücksichtigen. Die Motilität der Partikel führt zu einer Zunahme der kürzesten beobachteten Durchlaufzeiten sowie zur Abnahme der längsten Durchlaufzeiten.

1. Introduction and overview

A good understanding of flow and transport properties in porous media, i.e., materials consisting of a mixture of solid and void phases that are accessible to fluids, is of practical relevance in many different branches of science and technology. The definition of a porous medium obviously applies to many materials that are familiar from everyday life such as textiles, which owe their breathing properties to their pore structure. The high porosity of polystyrene, which allows it to trap large amounts of air, results in its outstanding insulating capabilities. Soil can store water, among other substances, in its pore space, whereby plants are enabled to absorb nutrients through their own capillary network. Groundwater flow and bioremediation of polluted aquifers are two more areas of general interest where knowledge of flow processes in porous media is essential. Blood perfusion throughout the human body is another example for flow in a highly complex and even dynamic porous medium, and its understanding is of huge interest for biomedical applications. Porous media are also important for technical applications. The most prominent example probably is hydrocarbon recovery, where the ability to predict how much oil or gas can be extracted at what expense from a reservoir is crucial for any company in that sector. The reservoir rocks containing the hydrocarbons are random networks of interconnected pore bodies and pore throats, which makes it very hard to estimate how much hydrocarbons can be recovered, and especially how much can be recovered by enhanced and costly techniques. The importance of poroelastic properties of building materials should also not be forgotten. If its architect had not been so unaware of the poroelastic properties of the ground underneath, the leaning tower of Pisa never would have enjoyed its current level of popularity.

The common property of all porous media is their complicated pore structure. Simple cylindrical pipes for example can be characterized by one length scale, whereas the pore space in porous media is a complex network of interconnected channels of nonuniform size and shape. This makes it very demanding to describe their structure, and in many cases the full structure is not known in the first place, as one cannot see inside a structure. But even if one knows the precise structure of a porous medium, there still is no easy way of calculating its flow and transport properties, because solving the equation for the flow of a Newtonian fluid, that is, the Navier-Stokes equation, in a large structure with disordered boundaries is virtually impossible. Therefore, one has to know which structural parameters are best suited to allow for a prediction of flow and transport properties and vice versa. This relation between the morphology and the dynamical properties of porous media is the center of interest of this thesis.

Despite the long history of research in porous media which has intensified during the last several decades, one cannot help but be surprised by the paucity of detailed knowledge of some general aspects of flow and transport in porous media, which is likely

owed to the fact that the precise structures of the considered porous media were unknown in many experiments and the transport therein was not observable on the microscopic level.

The experimental strategy in this work is to use porous structures which are created artificially by soft lithography. Thus, the microscopic details of the porous media are known and can be varied in a controlled fashion to study the effects of structural changes on the permeability, i.e., the ease for flow, and the transport of small particles. First, however, a suitable probe for the fluid flow must be found. In our studies, aqueous solutions with colloidal particles are injected into the porous media and a pressure drop is applied. The small particles are observed as they flow through the structures by conventional video microscopy. Particle tracking velocimetry is performed to reconstruct their trajectories and determine particle velocity fields.

Initially, the effect of particle size on the resulting particle velocity fields is studied, which is crucial knowledge for the study of flow properties.

Once the relation between particle and fluid velocity has been analyzed, the first aspect investigated is the relation between purely morphological quantifiers of the pore structure and the permeability of a porous medium. There are several attempts to reconstruct porous media based on limited information about their morphological properties. For sedimentary rocks this has been achieved with the help of Boolean models, which form a structure by successively adding grains of appropriately chosen shape. It was shown that the transport and mechanical properties of the reconstructed and original structure agree, if certain morphological measures, namely the Minkowski functionals, are identical. Motivated by this result an equation is introduced, which only uses purely geometrical quantities to predict the permeability of porous structures that consist of randomly placed overlapping circles or ellipses. We also test for universality of the equation by applying it to structures where void and solid phase have been exchanged, that is, structures with a totally different morphology.

Next, the effect of the pore structure and particularly the effect of stagnant areas, where the fluid is practically at rest, on the distribution of transit times of small particles is examined, which is another important aspect considering the transport in porous media. Since the particles are only diffusing inside stagnant areas, they can be trapped for very long times that are not easily accessible by an experiment. To avoid this problem, the particle velocity fields of three structures are measured experimentally and are used in an overdamped Langevin simulation to generate a large number of particle trajectories. These simulated trajectories show how the stagnant areas influence the resulting transit times and how they can be related to their geometry. In addition to these simulations of passive particles, the simulations are also modified to study the transport of active particle, i.e., particles that can propel themselves. Interestingly, their self-propulsion can lead to a decrease as well as to an increase of transit times, depending on the type of structure.

The thesis is structured as follows:

Chapter 2 gives an overview of the structural quantities, like porosity, specific surface and the Euler characteristic, that allow for a quantitative description of porous media. The accessible pore space can be divided into two parts: the backbone part, where

the fluid is flowing fast, makes the largest contribution to the total flow rate, and the stagnant parts, where the fluid is practically at rest. This distinction is important to understand the changes in flow and transport behavior that occur in a porous medium as the porosity is lowered. Critical path analysis and percolation theory, which are very handy and insightful tools for the treatment of porous media, are briefly introduced and, finally, Boolean models, which show resemblance to naturally occurring porous media and will be used for our experiments, are discussed.

Chapter 3 summarizes how the flow and transport phenomena are affected by the pore structure. The basic equations for flow of a Newtonian fluid inside an arbitrary geometry, that is, the Navier-Stokes and the continuity equation, are introduced. In case of the low flow rates in most porous media the Navier-Stokes equation can be simplified to the Stokes equation. In the Stokes regime there is a simple linear proportionality between applied pressure and the flow rate which is called Darcy's law. The proportionality constant is the permeability, which is one of the most important parameters of a porous structure and its relation to the pore structure is addressed in this work. Among the many laws that allow for a prediction of the permeability the main focus will lie on the Katz-Thompson law, that is motivated by ideas used in critical path analysis, i.e., the dominance of flow through a pore of critical diameter. The combined effect of the spatially varying velocity field imposed by the irregular pore structure and diffusion lead to the phenomenon of hydrodynamic dispersion, which is the spreading apart of initially closely localized particles as they move through the structure. The dispersion mechanisms and their influence on transport of solutes in porous media with emphasis on the role of stagnant parts are presented in the last section.

Chapter 4 deals with experimental details. Soft lithography is used to prepare samples with a well-defined structure. The movement of the small particles that are dispersed in an aqueous solution is recorded via conventional video microscopy.

Chapter 5 describes particle tracking velocimetry, which is the experimental method that is used throughout this work to capture trajectories of small tracer particles that are dispersed in an aqueous suspension. The captured trajectories are used to calculate particle velocity fields which can then be related to the velocity of the fluid. The problem is that a particle of finite size will alter the fluid around it and will not exactly follow the motion of the fluid. In other words, the particle velocity at its center of mass is not identical to the fluid velocity. The influence of the particle size in porous media is also debated in more detail. Two methods that solve the problem and enable the measurement of permeabilities of the investigated structures are introduced: The constant-head method uses a reference channel of theoretically known permeability to calibrate the particle velocity, whereas the falling-head method utilizes an exponential decay and the linear relation between applied pressure and mean particle velocity.

Chapter 6 presents the results of permeability measurements of twenty different porous structures that cover the full range of porosities. First, two series of porous structures which consist of randomly placed overlapping monodisperse circles (ROMC) or ellipses (ROME) are determined experimentally and by simulations. By also measuring the conductivities of the structures with the help of simulations, the applicability of the Katz-Thompson model is tested. Motivated by the successful prediction of trans-

port and elastic properties of porous media by Minkowski functionals, a formula for the permeability which only depends on structural parameters is introduced. The question of the universal applicability of this formula is tested by comparing its predictions with measured and simulated permeabilities of structures with totally different morphologies, in our case, ROMC and ROME structures, where the two phases have been exchanged.

Chapter 7 is devoted to the study of hydrodynamic dispersion of small tracers in ROMC structures with varying porosities. Particles that enter stagnant areas from where they can only escape by diffusion can have experimentally inaccessible transit times. Since these events are, however, of central importance for a correct determination of the transport properties of a porous structure, a semi-experimental approach is followed. So, first the velocity fields of three structures with decreasing porosities are experimentally measured. These velocity fields are employed in an overdamped Langevin simulation to obtain a large number of trajectories. The longest transit times are compared to mean escape times of stagnant areas, which are related to their geometry. In addition the simulation is modified to account for active particles, i.e., particles that can propel themselves. It is investigated how the varying motility of the particles affects their transit times.

Parts of this work have already been published:

1. "Measurement of permeability of microfluidic porous media with finite-sized colloidal tracers"
   C. Scholz. F. Wirner, Y. Lie, and C. Bechinger, Experiments in fluids **53**, 1327 (2012)

2. "Permeability of porous materials determined from the Euler characteristic"
   C. Scholz. F. Wirner, J. Götz, U. Rüde, G. E. Schröder-Turk, K. Mecke, and C. Bechinger, Physical review letters **109**, 264504 (2012)

3. "Geometrical interpretation of long-time tails of first-passage time distributions in porous media with stagnant parts"
   F. Wirner, C. Scholz, and C. Bechinger, Physical Review E **90**, 013025 (2014)

2. Structural characterization of porous media

Loosely speaking, a porous medium is a material with holes much like Swiss cheese. Materials with very simple pore space geometries like a garden hose or a cube of (let's be generous) gold with drilled, isolated holes are commonly not classified as porous media. Although it is hard to come up with a precise definition of porous media, all porous media have some properties in common, that allow them to be grouped. Of course, a fraction of the volume of the porous medium must be void space, also referred to as pore space or simply pores, that can be filled with a fluid. The most interesting and relevant questions in the study of porous media arise in connection with a fluid flow through a porous medium. Thus, porous media considered in this work are stipulated to have a large number of interconnected pores which form at least one continuous path from one end of the structure to the other, along which fluids can flow. The basic feature that makes porous media unique and distinguishes them from simple materials with holes is their often highly complicated pore geometry. The majority of porous media consist of well-connected, narrow channels of nonuniform size and shape distributed all over the material. As a consequence of the narrow channels, the ratio of surface to volume (specific surface) is very high.

The complex pore structure of disordered porous media determines their flow and transport properties. Whether it is the amount of fluid or particles flowing through a porous medium at a given pressure drop or the spreading of an initially localized drop of dye travelling downstream, all flow and transport phenomena can be explained to a large degree by the geometry of the porous medium. In contrast to flow in simpler boundaries, like circular pipes or periodic porous media, a disordered porous medium cannot be uniquely described by a small set of numbers. Even if the exact structure on a microscopic level was known and the very demanding equations in these complex boundaries could be solved, the solution would contain far too much information to be of practical use. Such being the case, nonuniform porous media are described by macroscopic pore structure and transport parameters (averages of the corresponding microscopic parameters over a length scale much larger than individual pores), e.g., porosity, specific surface or permeability. These and other quantities, which cannot simply be calculated, since the pore space morphology is often too complicated and not known in detail, can be measured in experiments.

The following sections describe the different geometrical and topological parameters, which are used to characterize complex porous media. Some experimental techniques for the measurement of the most relevant parameters are also discussed, because experiments which used these techniques first revealed the complex structure of natural porous media

and stimulated the development of more appropriate models for the pore space. The penultimate section touches some aspects of percolation theory, which help to understand porous media. The last section describes the structures, that are used in this work. The chapter was inspired by [1, 2, 3, 4], to which one may also refer for more details.

2.1. Geometrical characterization of porous media

2.1.1. Porosity

A porous medium is composed of a solid phase and a void phase (pores), where normally fluids can flow. As the term "porous" suggests, one basic parameter for the characterization of a porous medium is its porosity. Porosity ϕ is the ratio of the void volume to the total volume of a porous medium:

$$\phi = \frac{V_v}{V_{tot}} = \frac{V_v}{V_v + V_s}. \tag{2.1}$$

V_{tot} is the total volume, which is the sum of V_v, the volume of the void phase, and V_s, the volume of the solid phase. The different volumes are illustrated for an exemplary porous medium consisting of overlapping circles in Figure 2.1. The cyan domains correspond to the void volume and the black domains to the volume occupied by solid material. In simple words, the more volume is occupied by solid the lower the porosity is.

Below a certain value of ϕ, which depends on the formation process of the material, there is no continuous path of void space through the structure, i.e., fluids cannot flow through the structure any more. The corresponding critical value ϕ_c is called percolation threshold. It will be elaborated in section 2.3 and 2.4, where morphological details of the structures that were used in this work will also be given.

In Figure 2.1 there is also a small enclosed, isolated volume V_e that is not connected to the rest of the void space. It is crucial to distinguish between the part of the void space that is isolated and the part that belongs to the sample-spanning void, or simply open, space V_o of the porous medium. Principally, only the interconnected pore space can make a contribution to flow of fluids through a porous medium, whereas isolated pores can also be viewed as part of the solid phase. Therefore, it makes sense to define an open porosity[1] ϕ_o which excludes the isolated pore space:

$$\phi_o = \frac{V_v - V_e}{V_{tot}} = \frac{V_o}{V_{tot}}. \tag{2.2}$$

Representative volume

It should be noted that the measured porosity gives just an average value for the total volume that is considered. If the whole porous medium is considered, the porosity is a uniquely defined quantity, but in general the porosity, like any other quantity, depends

[1] In the literature, this quantity is often called effective porosity.

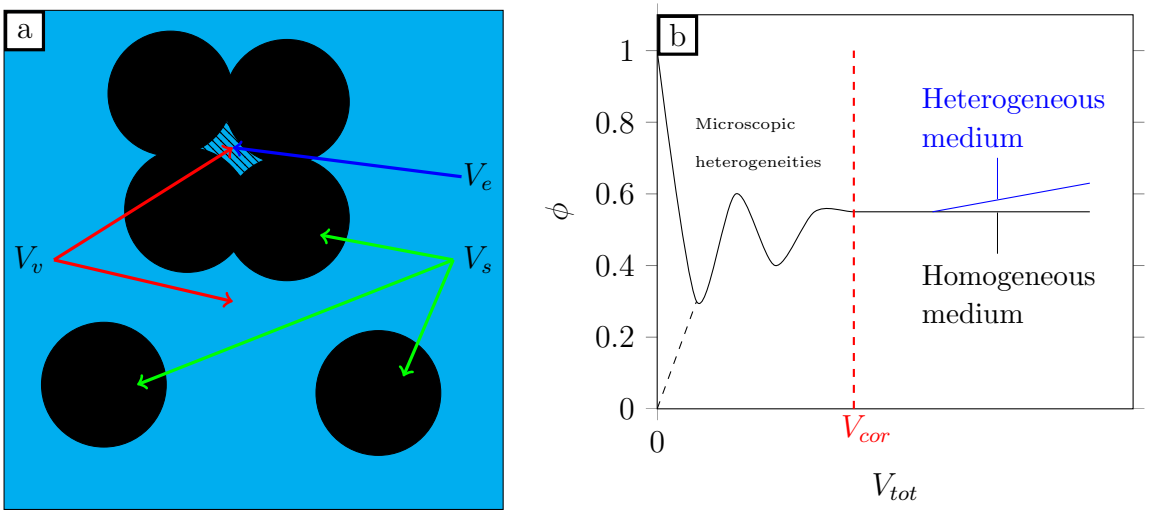

Figure 2.1.: (a) Schematic illustration of a porous medium. The total volume V_{tot} of the medium is made up of the volume of the solid parts V_s (black) and the volume of the void parts V_v (cyan). The small enclosed volume V_e (hatched) inside the solid phase, which is also part of the void space, is not connected to the sample-spanning void space. (b) Porosity as a function of the considered volume V_{tot}. For a homogeneous medium (black line) a representative value for ϕ is obtained for $V_{tot} \geq V_{cor}$, while for a heterogeneous medium (blue line) ϕ does not converge. (Reproduced from [2].)

on the size of the considered volume. The porous media that are studied in this work are disordered. Disordered media can be classified in two subgroups: macroscopically homogeneous and macroscopically heterogeneous. Evidently, if only small samples of a macroscopically homogeneous porous medium are investigated, the microscopic randomness of its pore space will manifest itself in strong fluctuations of the measured quantities for each sample. Only if the samples are larger than a certain correlation length ξ or a corresponding correlation volume[2] V_{cor}, the measured properties for different samples will not differ and yield results which are representative for the whole medium. For heterogeneous media, the correlation length ξ is larger than the length of the whole medium. Thus, there will be variations as one looks at samples of different parts of these media, which cannot be avoided by increasing the sample size. The only representative volume in that case is the whole porous medium. A system of size L below ξ can be self-similar and its properties might scale with a fractal dimension D_f, e.g., the mass of the fluid in the sample-spanning void phase scales as $M \propto L^{D_f}$. Although this might sound like quite an academic problem, the question whether a sample can be considered as representative of the whole structure, is of immense practical importance. Take, for example, a self-similar oil reservoir, where the mass of oil in a drilled hole scales as $M \propto L^{2.8}$, which implies that the density of recoverable oil decays as $L^{-0.2}$. If the oil content of the drilled hole is estimated by taking out a sample of size of 1 m of a 10 km large reservoir, the oil content would be overestimated by 84 %. So, better ask

[2] Also called representative volume.

for the fractal dimension in case somebody is trying to sell you an oil field. Therefore, whenever a measurement is carried out on a small sample, the experimenter must wonder if the results can simply be upscaled. Scanning electron microscopy and optical data of sandstones have indicated that several sandstones are fractal geometries over 3 to 4 orders of magnitude [5]. The fractal dimensions for these sandstones varied from 2.57 to 2.87 suggesting that the formation processes differ fundamentally. Studies of pore surfaces of various materials have also revealed self-similarity, which was explained by assuming an iterative formation mechanism [6].

A typical behavior of the porosity in dependence of the total considered volume for a homogeneous (black curve) and heterogeneous medium (blue curve) is shown in Figure 2.1 (b) to illustrate the difference between these two material subgroups and to define V_{cor}. The whole domain of microscopic heterogeneities which is defined by $0 \leq V_{tot} \leq V_{cor}$ shows the same qualitative behavior for homogeneous and heterogeneous materials, i.e., strong fluctuations in the porosity. Starting at the very left, where the volume is converging to a point, the porosity will be either 0 (dashed line) or 1 (solid line), according to whether the point is in the solid matrix or in the void space. As V_{tot} is increased, the fluctuations of the porosity continuously decay until a plateau is reached at V_{cor}. In case of homogeneous materials (black line) the porosity will remain constant for further increasing V_{tot} indicating a representative value ϕ. Yet, for heterogeneous materials (blue line), which might also show a plateau in some volume range, a further increase in V_{tot} will show changes in ϕ and reveal that V_{cor} cannot be defined for this material class. In this case the result of a measurement cannot be upscaled since the whole porous medium does not exhibit the same behavior as the small sample. Unfortunately, heterogeneities at different length scales persist in many natural porous media making it hard for researchers to deduce overall properties of a porous medium by just looking at a small part of it. To make matters worse, a porous medium which might appear homogeneous with respect to the porosity, can at the same time still show variations in other properties, e.g., the permeability, which quantifies how easily a fluid flow through a medium. Two media can have the same porosity but very different permeabilities. For example, one medium might just consist of one large pathway through the structure, whereas another can be composed of many finely branched capillaries. Clearly, fluid flow will behave completely different in these two structures. So, it is evident that due diligence is required if one wants to make useful statements about the properties of porous media, especially when one is dealing with heterogeneous media, which can be found among natural formations.

Porosity measurement

The porosity of natural porous media can be measured by several methods [7]. A straightforward but destructive method consists of measuring the total volume of the porous medium, this step is necessary for any method, and then grinding of the material followed by measuring the volume of the remaining solid. Employing quantitative stereology (an optical method) to determine the areal porosity of a random pore structure also gives useful results, but may not account for very small pores.

More modern imaging techniques like X-ray computed tomography (CT) have yielded detailed information about the extremely complex 3D morphology of porous media with an accuracy of only a few microns [8]. Millimeter-scale CT of Berea sandstone, which was believed to be homogeneous and have an uncorrelated pore-size distribution, has provided convincing evidence that correlated heterogeneities persist beyond one or two pore lengths and challenged the assumption used in many models of porous media that the properties of such stones are randomly distributed at the pore scale [9].

Another well-established method is mercury porosimetry [10], which has been a workhorse for the investigation of the pore space since its invention. In this method the material is first evacuated and subsequently immersed in mercury. Mercury does not wet most materials and thus will not penetrate into the pore space by itself. By application of an increasing pressure, mercury enters the pore space. The injected volume of mercury as a function of the pressure is measured. At a characteristic maximum pressure P_{max}, which is unique for the used porous sample, the mercury can fill even the smallest pores. By measuring the injected volume at this pressure, ϕ can be calculated. The drawback, though, is that such high pressures might also change the pore structure of the material.

Very interestingly, not all of the mercury is retracted when the pressure is lowered again, i.e., there is hysteresis between the injection and retraction curves. An example of a typical capillary pressure curve is shown in Figure 2.2 (a). First, the pressure P is increased along the blue curve until, at P_{max}, the whole medium is saturated with mercury, that is, the saturation ρ of the pore space equals unity. Also note that there is a rapid rise in the curve at the inflection point, which is believed to occur when the mercury first forms a sample-spanning cluster [11]. At this point the sample also forms electrical continuity across the sample, which makes it experimentally well-defined. After the intrusion process, the pressure is lowered again and the mercury retracts. During this extrusion ρ moves along the red curve which, in general, does not collapse onto the intrusion curve. When the pressure reaches zero, some mercury still stays in the pore space. Although the precise interpretation of the curves is complicated, a lot of information about the morphology of porous media can be gathered from them.

In order to qualitatively understand the curves, one has to recall that a minimum pressure, which is given by the Washburn equation (WE), $P = \frac{4\sigma cos(\theta)}{d}$, is needed to fill a capillary tube of diameter d. Here, σ is the interfacial tension between mercury and the pore surface and θ the contact angle between mercury and the pore surface. Before 1977 the pore space was mostly modelled as a bundle of nonintersecting capillary tubes of varying diameters, completely ignoring its topology. This vastly oversimplified picture of porous media probably was motivated by the similar behavior of slow fluid flow in porous media, given by Darcy's law, and the laminar flow through tubes described by the Hagen-Poiseuille equation, both of which are linear in pressure gradient. With this simple assumption and the WE, the capillary pressure curves can now be interpreted. As the pressure is increased the pores are filled one after another, starting with the largest pores, according to the WE. So, each pressure corresponds to a certain pore size. Therefore, the derivative of the curve can also give information about the pore size distribution. It was recognized that the assumption of nonintersecting tubes is

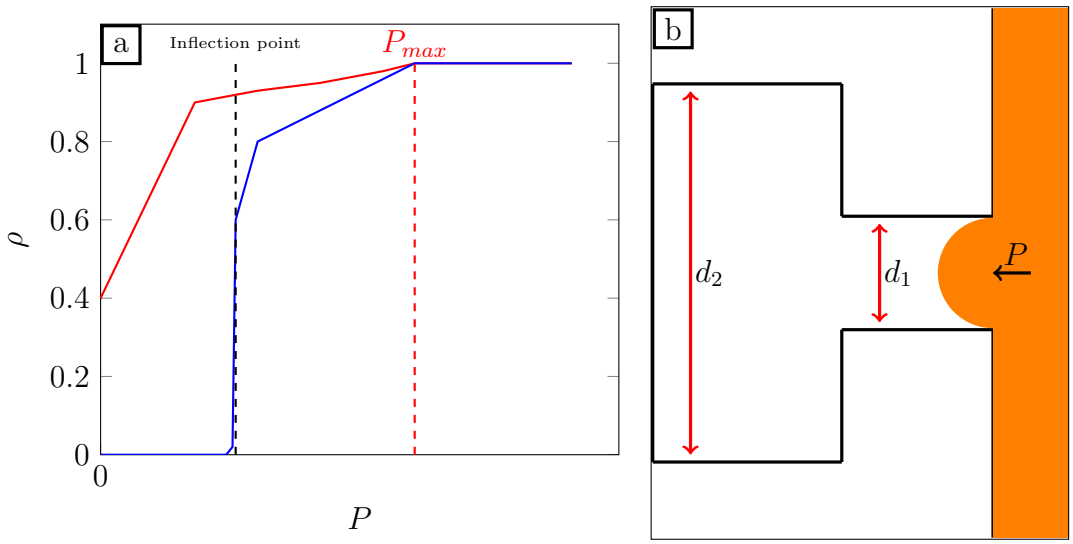

Figure 2.2.: (a) Typical capillary pressure curves for intrusion (blue curve) and extrusion (red curve) of mercury in a porous medium. At the inflection point (black dashed line), which indicates the formation of a sample-spanning mercury cluster, the saturation rises steeply and finally saturates at P_{max}, when the whole medium is filled with mercury. (b) Mercury (orange) is pushed into large capillary tube (pore) of diameter d_2 via small tube of diameter d_2. The mercury can only fill the large tube, if the critical pressure of the small tube is surpassed.

problematic, since large pores that should be filled with mercury would not be filled if they are only connected through smaller pores [12]. The consequence of this neglect is that the contribution to the pore space of large pores is underestimated and that of small pores overestimated. Yet, the goal of such experiments is to get reliable information about the morphology of the medium to, e.g., judge the potential yield of hydrocarbon reservoirs. Even though it took more than 20 years, the connection between the topology of the pore space, described by percolation theory (covered in section 2.3), and mercury porosimetry was finally fully appreciated [13, 14]. Once this seemingly simple idea of pore-space interconnectivity is taken into account, the shape of the capillary pressure curves and their hysteresis start to make more sense.

In Figure 2.2 (b) a schematic of two connected idealized pores with diameters $d_1 < d_2$ is shown. The mercury experiencing some pressure P and trying to enter the first pore is drawn in orange. As P is increased, the minimum pressure according to the WE is first reached for the second pore with d_2, but as this pore is connected to the mercury by the smaller pore, no mercury can enter. If P is further increased to the critical value of the small pore, mercury will enter the small and the large pore. This will result in a rise of the saturation in the capillary pressure curve. Now, when P is lowered again, the mercury will first retract from the small pore due to the higher critical P, while it can snap off and stay in the large pore. This is one explanation why there is hysteresis in such curves. The phenomenon of mercury porosimetry can only be understood, if both the pore geometry and the connectivity of the pores are accounted for. Therefore, it seems reasonable that any realistic model of porous media must not only include the

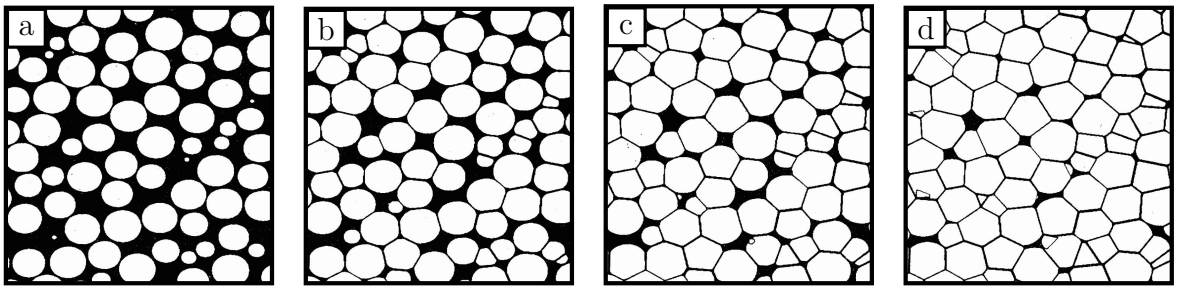

Figure 2.3.: Cross section of sample produced by the grain-consolidation model. White corresponds to the solid phase occupied by spheres and black stands for the pore space. Several stages with different porosities are shown: (a) initial configuration $\phi = 0.364$, (b) $\phi = 0.200$, (c) $\phi = 0.100$ and final stage close to the percolation threshold (d) $\phi = 0.030$. [15].

shape and size of the pores but also their interconnectedness, i.e., the topology of the pore space.

Diagenetic process

The geometrical properties of a porous medium and, in particular, their widely varying porosities can be more readily understood by looking at some basic diagenetic processes that can lead, e.g., to the formation of rocks. Accurate knowledge of the formation history of a reservoir rock, for example, can be crucial to judge its potential for hydrocarbon recovery. The solid phase of porous media often consists of grains of different size and shape. The grains can either be loosely packed, like in sand, or they can be cemented together and form a consolidated porous medium, e.g., a sandstone. A simple geometrical model for the diagenetic formation process of such consolidated structures is the grain-consolidation model [15]. The stages of the formation process are shown in Figure 2.3. Initially, the porous medium is made up of identical spheres, which are randomly distributed following a Bernal distribution [16]. The resulting initial structure with $\phi = 0.364$ is shown in Figure 2.3 (a). During cementation the pore space gets filled with material and the porosity of the structure moves towards lower values. In the grain-consolidation model, cementation is accounted for by increasing the radii of the spheres simultaneously (Figure 2.3 (b-d)). When the spheres start to overlap, they are gradually distorted. The low porosity $\phi = 0.030$ of the final structure (Figure 2.3 (d)) implies that this model can explain how a high-porosity, loosely packed structure is transformed into a porous medium whose porosity is an order of magnitude lower. The porous media that are generated with this model also show close resemblance to naturally occurring rocks (Figure 2.4) which usually have a porosity of less than 0.4. The interconnectedness of the initial grain distribution, which is an essential feature of many porous media [17], is also conserved in the grain-consolidation model.

The changes in a porous medium during cementation are time-dependent. The initially accessible pore space gets filled up with material that is transported by a fluid. Consequently, the pore space shrinks, associated with a lower rate of fluid transport,

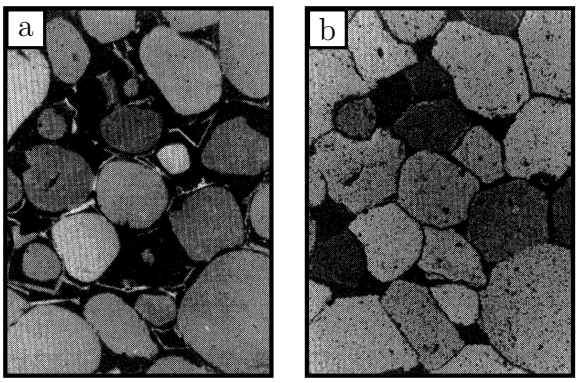

Figure 2.4.: Devonian sandstone from Illinois. (a) By means of cathodoluminescence the original loosely packed grains are uncovered. (b) Illumination with normal light shows the morphology of the pore space after cementation. [15].

which in turn lowers the rate of cementation. Following this simplified line of argument, it can be seen that the connectivity of the original pore space is preserved.

Looking at Figures 2.3 (a-d), it can also be understood that the porosity of unconsolidated materials mainly depends on the shape and size distribution of the individual grains and their packing. The holes between large grains can be occupied by smaller grains, whereby the porosity would be reduced. Thus, a porous medium composed of grains with a wider size distribution will, ceteris paribus, result in a lower porosity. By contrast, the porosity of a consolidated material is primarily determined by the degree of cementation. In general, the porosity of the pore space is determined to a large extent by the wide open regions which are connected by narrow pore throats. These small throats mainly control the transport processes of the network.

Cementation is not the only process involved in the formation of reservoir rocks. In addition, fracturing and the dissolution of rock material can lead to a substantial increase in porosity. More than half of all the pore space can be represented by such solution pores [18]. Another important mechanism is compaction. The deeper one goes into the rock, the stronger the grains are compacted, and, as a result, the lower the porosity is. Porosities of shale have been found to decrease from 0.60 to 0.06 as depth was increased from 0 to 1800 m [19].

Given the complexity of the formation processes, it comes as little surprise that materials which practically span the whole range of possible porosity values, from down to about 0.01 for limestones and shales up to 0.8 for peat soils, exist [20].

2.1.2. Backbone and stagnant parts

In the previous section the void space of a porous medium was split in two parts, the open volume V_o and the isolated volume V_e. It was argued that principally only V_o can contribute to flow through a porous medium, but things are a little more complicated. Figure 2.5 shows another example of a porous medium that is again composed of overlapping circles. Here, the white and the cyan domain are part of the sample-spanning

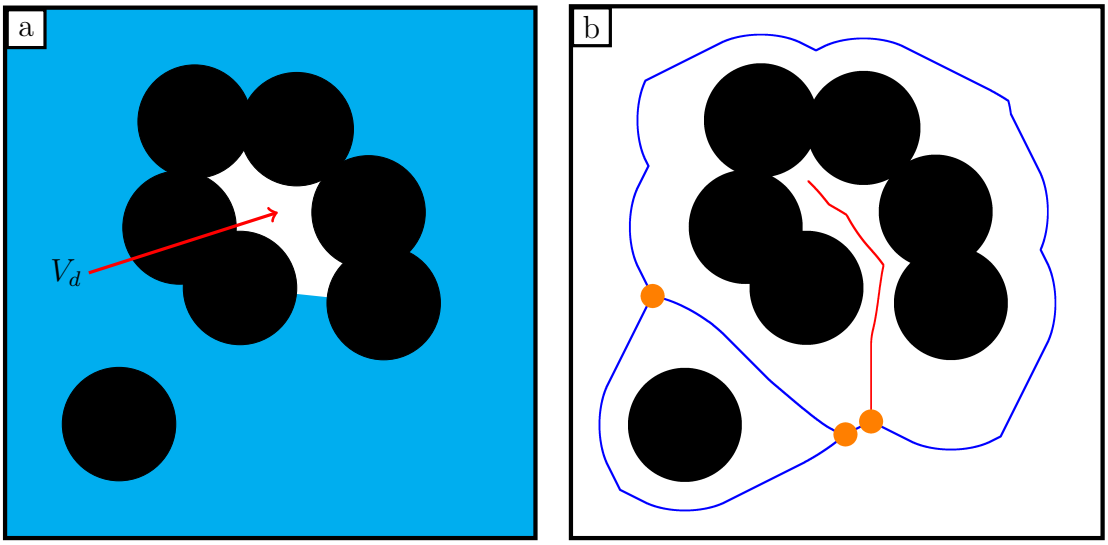

Figure 2.5.: (a) Porous medium with stagnant part (white) of volume V_d. The backbone of the structure (cyan) carries most of the flow. (b) A simplified network skeleton of the pore space. Nodes (orange circles) are connected by bonds (blue lines). The red line is only connected to one node, which means that the corresponing pore space is a stagnant part.

void space and consequently fluid transport can occur in them. Obviously, not the whole open volume of a disordered medium can contribute equally to flow, just like a bay that is connected to a river does not. There are pores which only have a single connection to the sample-spanning void space and may therefore be practically ineffective in terms of flow through the structure. Accordingly, these parts are called dead-end, quiescent or stagnant parts with a stagnant volume V_d. These parts, apart from being defined by their connectivity, can also be identified by looking at the velocity field of the structure. In a stagnant part the flow velocity or the velocity of dispersed particles will be practically zero, so that the stagnant parts can also be found by application of a velocity threshold. In chapter 7 we will see that particles will only diffuse inside such parts and not be advected in a certain direction, because there is no flow. The white domain in Figure 2.5 (a) is one of these stagnant parts. The cyan domain, which is left when all the stagnant parts are removed, dominates flow through the structure and is called backbone. In analogy to the open porosity ϕ_o, we can also define a backbone porosity ϕ_b and a stagnant porosity ϕ_d, which only factor in the backbone or stagnant part of the open pore space, respectively.

The structure of a complicated pore space can also be studied with the help of its deformation retract, which is obtained by shrinking the pore space until there is a network of bonds and nodes left [21]. The bonds intersect at the nodes. Any porous medium can principally be mapped onto such a network of bonds and nodes [22, 23, 24], an example of which is shown in Figure 2.5 (b). The nodes are represented by orange circles and the bonds by blue and red lines. The blue lines correspond to the backbone part, as these are always connected to more than one node, whereas the red line is only

connected to one node, indicating a stagnant part.

Although the stagnant parts of porous media, by definition, contribute very little to the fluid flow, they still cannot be neglected if one wants to understand how material is transported through or stored in porous media. One example where stagnant parts play a significant role is hydrodynamic dispersion, which is the spreading apart of initially adjacent particles in a porous medium similar to a diffusion process. The fundamental difference is that in addition to molecular diffusion the particles are also advected by a nonuniform flow field that is caused by the morphology of the porous medium. Particles that are travelling along the backbone can also diffuse into stagnant parts where they may be trapped for long times. This, of course, will affect the transit times of these particles or any other transported material. The distribution of transit times is a fingerprint of the porous medium studied, as it is clearly related to the morphology of the pore space. Details about hydrodynamic dispersion and the effect of stagnant parts will be discussed in 3.3 and 7.

It is also worth noting that especially in low-porosity materials whose porosity is close to the percolation threshold ϕ_c and, hence, are likely to have a low connectivity, most of the accessible space can consist of stagnant parts. Many reservoir rocks have such low porosities and trap oil in stagnant parts. Clearly, the amount of oil which can be recovered from such reservoir rocks depends on the pore space (as well as on the properties of the fluid). Comparisons of samples with identical porosity have shown a strong impact of pore-to-throat size ratio, throat-to-pore coordination number and the type of nonrandom heterogeneity on the recovery efficiencies [25]. In other words, how much oil can be extracted depends mainly on the connectivity of the pore space. Oil which is trapped in stagnant (poorly connected) areas cannot be recovered easily, whereas oil in the backbone can simply be pushed out. These issues along with other examples will also be discussed later on.

One might also think the other way round. Crude oil is believed to be formed by the decomposition of fossilized organic material [26]. During this process oil evolves as small bubbles in the water, that originally filled the pores. The small oil bubbles then travel, mainly upwards by buoyancy and capillarity, to the reservoir rock, where they finally accumulate. Of course, there has to be a barrier at some place, otherwise the oil would just travel to the surface and spread out. So, it seems logical to assume that much of the oil will end in some kind of stagnant area.

2.1.3. Specific surface

Flow and transport in porous media is all about the morphology of the pore space. The resistance to flow in porous media originates at the boundaries of the pore space where the fluid molecules exchange momentum with the molecules of the solid, which are at rest. The result is the so-called no-slip boundary condition stating that the fluid velocity at the fluid-solid interface equals the solid velocity, which is zero for resting porous media.

The magnitude of the influence of the surface on the properties of the porous medium can be quantified by the specific surface S, which is defined as the ratio of internal

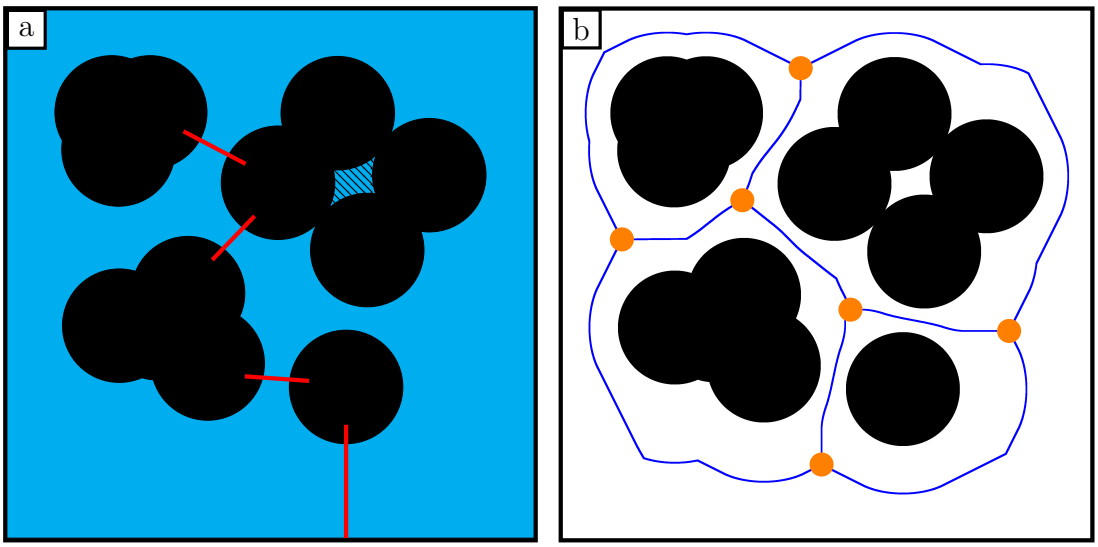

Figure 2.6.: (a) Illustration of a porous medium which is composed of two phases. The shown medium consists of four connected solid components (black) and two connected void components (cyan), one of which is enclosed in the solid phase (hatched). The Betti numbers of the pore space are $\beta_0 = 2$ and $\beta_1 = 4$. The Euler characteristic χ of the pore space equals -2, the open Euler characteristic $\chi_o = -3$ and the genus $G = 4$, which gives the maximum number of cuts that leave the pore space connected. Four cuts through the pore space, which still leave the pore space connected, are shown as red lines. (b) Nodes (orange circles) and connecting bonds (blue lines) of the corresponding network. The enclosed volume is neglected.

surface area A to the total volume V_{tot} of the porous medium:

$$S = \frac{A}{V_{tot}} \tag{2.3}$$

Similar to the porosity one could also define an open specific surface by replacing V_{tot} by V_o. S has been used to characterize transport phenomena in porous media and to predict their permeabilities [27]. It is also an important parameter for the efficiency of catalysts or filters. S is determined by the size, shape and packing of the grains forming the solid phase. Everything else being the same, S will be higher for smaller grains and for non-spherical grains [1].

2.1.4. Betti numbers, Euler characteristic, genus

In the previous paragraphs the important role of the topology of the pore space, i.e., the way the pores are connected, has already been mentioned several times. Here, we now introduce some useful topological parameters. Topological parameters of a porous structure quantify the network skeleton of porous media and can specify the mechanisms of fluid transport in the pore space. Topological parameters are invariant under deformations of the pore space and can only change, when structures break or fuse in some fashion. In other words, they ignore details of the pore shapes and sizes. There are

several methods to measure topological properties of porous media like stereology [28], which was also used to estimate the porosity, serial sectioning [22] and, most importantly, mercury porosimetry.

The connectivity of a pore space can be characterized by the Betti numbers. According to a central theorem of topology, two structures are topologically equivalent if and only if their Betti numbers are all equal [29]. The Betti numbers have been used to describe the pore space of porous rocks and predict several of their properties like permeability or residual saturation [22, 23, 30]. Many Betti numbers can be defined for a given structure, but for the structures investigated in this work, we will restrict ourselves to the first two Betti numbers.

The zeroth Betti number β_0 gives the number of connected components of a structure. If the whole structure is connected and no inclusions exist, $\beta_0 = 1$. The first Betti number β_1 is the number of holes in a structure. For a pore space, β_1 would give the number of connected solid parts in the structure. The topology of a pore space can again be studied by looking at its network skeleton, consisting of b bonds and n nodes, which is shown in Figure 2.6 (b). The nodes are represented by orange circles and the bonds by blue lines. The first Betti number can then also be defined as $\beta_1 = b - n + \beta_0$.

Another very useful parameter for the description of the pore space is the Euler characteristic χ, which is also related to the connectivity of the structure. χ is simply determined by counting the number of connected components of one phase (β_0 of that phase), which corresponds to the pore space, and subtracting the number of connected components of the other phase (β_0 of the other phase), in our case that is the solid matrix. Figure 2.6 illustrates an exemplary porous medium. The number of connected pore components is two (the connected accessible pore space plus one inclusion), the number of connected solid components is four, which gives $\chi = 2 - 4 = -2$. We also define an open Euler characteristic χ_o which does not count the enclosed void components because they do not contribute to flow. Here, $\chi_o = 1 - 4 = -3$. Therefore, $\chi_o - \chi$ gives the number of inclusions in the structure. The first two Betti numbers can be expressed in terms of the two Euler characteristics: $\beta_0 = \chi - \chi_o + 1$ and $\beta_1 = 1 - \chi_o$.

χ_0 is related to the genus G by $G = 1 - \chi_o$. The genus, which is numerically equal to β_1, gives the largest number of pore connections that one can cut without totally disconnecting any part of the pore space from the rest [21]. In our example G would amount to 4, implying that we can remove 4 interpore connections without losing the interconnectedness of the pore space, i.e., fluids would still be able to flow through the whole structure. One possible choice of such four cuts is shown as red lines. If one more cut is added, some part of the pore space will not be connected to the rest. So, G is a measure of the number of independent flow paths through a structure. The higher G or the lower χ_0[3], the better connected the structure is. One has to be careful not to automatically interpret a higher connectivity of the pore space with, say, a higher permeability of the structure. A sample with very few wide pathways and a low connectivity might have a higher permeability than one with an astronomical number of small pores and throats, even though it has a higher connectivity. One must also keep in mind

[3] As χ_0 is negative, higher G means lower χ_o.

that G is scale-dependent, it increases with increasing sample size and becomes a linear function for a sufficiently large sample, if the structure is homogeneous [21, 23, 31]. That is why it makes more sense to use the specific genus $G_V = G/V$ which is normalized by the sample volume and thus allows a comparison of different samples. For model rocks made of grains of the same size, G_V has been shown to correlate strongly with the residual saturation of a nonwetting liquid [30]. The reason is that at a higher G_V more snap-off events are needed, until an isolated blob is left, because more alternative routes for drainage are available. But despite its successes, the connectivity density, measured by G_V, also has to be taken with a grain of salt, because it depends on other characteristics of the pore structure like the mean distance between the pores [31]. A larger distance between the pores would give a lower value of G_V, although the pores might be just as well connected. Hence, G_V should be used in combination with other geometrical parameters. We will use a very similar quantity along with the critical pore size in section 6.1 to estimate the permeability of different structures.

2.2. Critical path analysis

We have just discussed topological quantifiers, which together with purely geometrical measures, like porosity and grain shapes and sizes, help to characterize a complicated porous structure. It was already stated that treating all paths through a structure on an equal footing can lead to severely flawed predictions of its properties. One insightful and practical way of accounting for the different degrees of importance of certain pathways is given by critical path analysis (CPA). The logic backing CPA is similar to the proverbial "a chain is only as strong as its weakest link".

CPA was pioneered in [32]. It was argued that the total resistance of a resistor network, where the values of individual resistances vary over a wide range, is mainly determined by resistances with conductivities higher than some critical value G_c. At this critical conductance the subset of resistances with values higher than G_c for the first time form a path which spans the entire system. Hence, transport of current in such a network is reduced to a percolation problem with threshold G_c. The path that results at G_c is called the critical path. The reasoning behind this assumption is that the network can be divided into three subsets. The first subset consists of poorly connected regions, which are formed by conductances higher than G_c. In our lingo, this subset would correspond to dead ends or stagnant parts. Even setting the conductivities of this subset to infinity, would not greatly change the overall conductivity of the network, for the current would still have to pass through conductances of order G_c to make it to the other end of the network. The second subset contains a relatively small number of conductivities of order G_c, which form a sample-spanning network, viz., the backbone of the structure. Combined with the isolated regions, they form the critical subnetwork. The remaining resistors have a low conductivity and yield only a small fraction of the total conductivity, for the simple reason that they are shorted out by the critical subnetwork. As a consequence, the total resistance is dominated by conductances of order G_c.

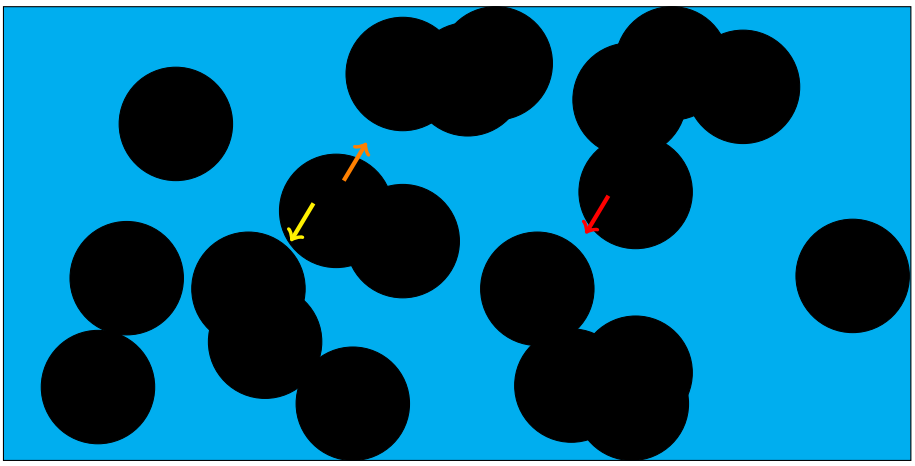

Figure 2.7.: A porous medium consisting of randomly placed circles. $\chi_o = \chi = -7$, i.e., there are several independent paths, which lead through the structure, but if one critical connection is cut, no fluid flow through the structure will be possible. This critical connection is indicated by the red arrow. The orange arrow points to another important connection, where most of the fluid will flow along. Removing this connection would only leave one path for the flow across the small throat, indicated by the yellow arrow.

Fluid flow through a porous medium can also be mapped onto such a (resistor) network. The discharge through a pore, for example, is proportional to the forth power of its radius. Consequently, in a disordered porous medium, which is made of many pores of a wide range of sizes, a large part of the pore space can make only a negligible contribution to the overall flow and transport properties of the structure. The central idea of CPA is to determine the weakest link and thereby determine the overall properties of the structure [4]. Simply put, the overall flow and transport properties should be a function of the radius of the smallest pore of sample-spanning paths which have the largest small pore, that is, the paths with the least resistance to flow. These paths are the critical paths for fluid flow. Since there may be more than one of these paths, one must also determine how frequently such paths occur. This is a big advantage compared to spatial averaging of flow properties over a large part of the sample, because all the parts with negligible effects on the investigated property are not accounted for.

For illustration purposes, an example of a porous medium is shown in Figure 2.7. Again, fluids can flow in the cyan domain. The colored arrows point at important connections through the pore space. There are several paths leading through the structure, but not all of them are equally important. If the connection at the red arrow is cut, no path will span the whole structure and, as a result, no fluid can flow. So, this connection is certainly part of the critical path and the corresponding pore, logically, is called critical pore. It is also obvious that the permeability of the structure would be greatly reduced, if the connection at the orange arrow is removed, as all the fluid would have to flow through the small throat at the yellow arrow. On the other hand, cutting the connection at the yellow arrow would have a very small effect on fluid discharge through the structure. From this we can conclude that the critical path, which determines the

flow properties of this structure, runs along the two connections indicated by the red and orange arrows. The critical pore, thus, is the one indicated by the red arrow, because it is the smallest pore of the path with the least resistance. Flow and transport properties will be functions of its pore radius.

The pore space of many reservoir rocks is characterized by a broad pore-size distribution (PSD) [33]. Investigations of fractured rocks, for instance, at the Fanay-Augères site also showed that only about 0.1% of the fractures made a significant contribution to fluid flow at large length scales, which suggests a poorly connected pore space, similar to a percolation network close to its percolation threshold [34]. Given these facts, it seems natural that CPA has been used to predict the permeability of porous rocks [35, 36, 37]. The applicability of the original CPA [32] for the determination of the relationship between the electrical conductivity and the permeability of three-dimensional pore networks was tested by comparing its results with computed actual permeability-conductivity relationships [38]. Excellent agreement was found for networks with low coordination numbers[4], which are likely to be characteristic of sedimentary rocks and soils. Yet, with increasing coordination number and decreasing broadness of the PSD the agreement worsened. This makes perfect sense, because only if the PSD is very broad and the coordination number low, the size difference between the critical pore and the larger pores will be substantial. The larger pores will then effectively be in series with the critical pore, but have a much lower resistance to flow, so that their resistance can be neglected relative to the resistance of the critical pore. We will have a more in-depth look at the Katz-Thompson law, which also uses CPA to relate the permeability of a structure with its conductivity and a critical pore radius, in 3.2.2.

CPA has also been used to describe hydrodynamic dispersion in porous media [39]. We will cover this topic in chapter 7.

2.3. Percolation theory

So far, we have introduced geometrical and topological parameters, which allow a characterization of the pore space. However, the discussion of their influence on transport processes in porous media was mainly discussed qualitatively and no general framework, which allows a deeper understanding on a quantitative basis, was presented. Such a framework and, hence, a very valuable tool for understanding and quantifying the effect of connectivity and geometry of the pore space on flow and transport properties in porous materials is percolation theory [40, 4].

Percolation theory was first used to study polymerization [41, 42], i.e., how small monomer molecules link together to form larger polymers. This process can lead to the formation of a gel, which is, in principle, an infinitely large molecule that spans the whole system. The theory was used to study the effect of the connectivity of the monomers on the properties of the resulting gel and to derive analytical expressions for

[4]The coordination number gives the number of throats that meet at a pore. It is also related to the connectivity of a structure.

these properties. Later, percolation theory in the context of fluid flow through a disordered medium was introduced [43]. Ideas from percolation theory were employed to model flow and dispersion of dye injected into a porous medium [44]. Calculated percolation properties have also been utilized to predict capillary pressure curves obtained by mercury porosimetry [13], which once more evidenced the important role of pore space interconnectivity. These and other results [14, 45, 46] made the usefulness of percolation theory seem compelling and finally resulted in a deeper understanding of the structure of porous media, which also stimulated the development of more realistic models of porous media. Several transport phenomena in porous media, like hydrodynamic dispersion, permeability, electrical conductivity [4] the distribution of oil and gas in reservoir rocks [40] have also been analyzed by percolation theory. In fact, critical path analysis of the last section, which is a result of percolation theory, provides another powerful tool.

We have already mentioned that any porous medium can be mapped onto a random network of nodes and bonds [24], which is similar to a random percolation problem. Since the network representation of a (natural) porous medium is still highly chaotic, percolation theory with its simple probabilistic approach, that, nevertheless, generates highly complicated structures, is a sensible candidate for the description of such complex topologies. The merit of percolation theory for the investigation of flow phenomena in porous media can best be appreciated by looking at one of the simplest (but still unsolved and profound) fundamental percolation problems.

In Figure 2.8 a very basic site percolation problem is illustrated. We start with an empty lattice of 100×100 sites. The individual sites of the lattice can be either occupied (open to flow), with probability p, or vacant (insulating), with probability $1 - p$. A group of nearest neighbor sites is called a cluster. All sites belonging to one cluster are connected by a continuous path of occupied sites. Figure 2.8 shows randomly generated samples[5] with occupation probabilities increasing from $p = 0.10$ to $p = 0.60$. For $p = 0.10$ there are only small clusters, mostly single occupied sites. The size of the clusters increases significantly for $p = 0.35$ and for $p = 0.60$ a cluster spans the whole sample from top to bottom and from left to right. If such a sample-spanning cluster of occupied sites is present, the system is said to be percolating. The occupation probability, above which the system is percolating, is called percolation threshold. For a finite system there is a certain probability that the system percolates for any nonzero occupation probability. For an infinitely large system of sites on a square lattice this topological transition is sharp and the corresponding percolation threshold amounts to $p_c \approx 0.5927$. Looking at the sample-spanning cluster formed for $p = 0.60$, many holes (occupied sites, which do not belong to the cluster) with different sizes exist. This occurrence of phenomena on all length scales is typical for systems close to p_c. Above p_c there is exactly one cluster that extends through the whole system, whereas below p_c there are only isolated clusters, viz., there is a phase transition at p_c.

Similar to other phase transitions, which may occur at, e.g., a critical temperature, the behavior of many basic properties related to percolation phenomena obey universal

[5] A simple MATLAB program, which assigned a random value between 0 and 1 to each pixel, was used. A consequent application of a threshold value p resulted in the wanted occupation probability.

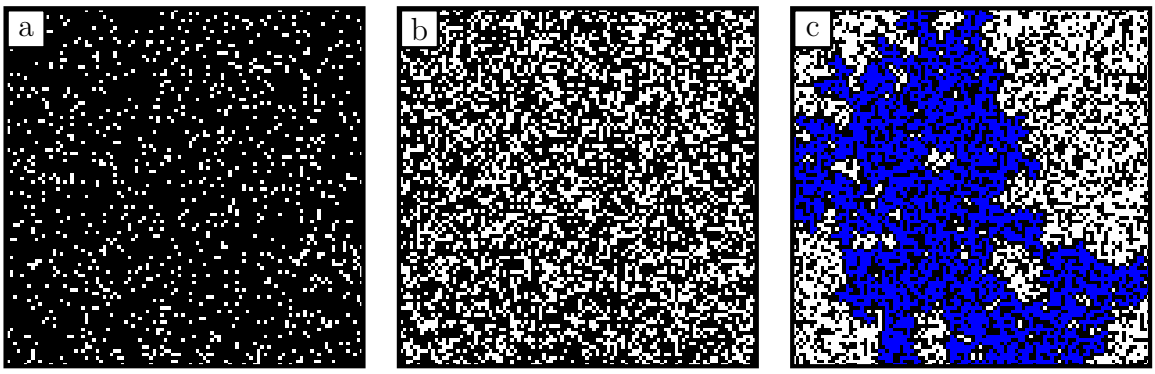

Figure 2.8.: Examples for site percolation on a 100×100 square lattice. The white pixels correspond to occupied sites, the black ones to vacant sites. The occupation probability p was varied for the three examples shown: (a) $p = 0.10$, (b) $p = 0.35$ and (c) $p = 0.60$. Only $p = 0.60$ is slightly above the percolation threshold $p_c \approx 0.5927$. The (largest) sample-spanning cluster, which is shown in blue, contains several holes of varying size.

scaling laws with critical exponents that are independent of the lattice or network studied and only depend on the dimensionality of the system. This universality even persists, if correlations between occupied sites exist and also for widely varying values of p_c. As an example for such a scaling law we look at the formerly introduced correlation length ξ, which gives the length scale[6] beyond which the system is macroscopically homogeneous for $p > p_c$:

$$\xi(p) \propto (p - p_c)^{-\nu}. \tag{2.4}$$

Here, ν is the critical exponent, which equals $4/3$ in $d = 2$ dimensions[7]. Since ν is positive, ξ diverges[8] at $p = p_c$. So, at $p = p_c$ there is no relevant physical length scale left in the system and the percolating system becomes a self-similar object on all length scales, which makes fractal analysis important. In everyday language, a system that has scale invariance will (statistically) look the same, if we zoom out. In contrast, for $p \neq p_c$, ξ will be finite and if we zoom out, the correlation length will appear smaller, that is, the system will seem to be further from the percolation threshold. Of course, all our earthly issues only involve porous media of finite extent, so that self-similarity on all length scales cannot be encountered. But that does not mean that the whole concept should be discarded. We have stated earlier (section 2.1.1) that a system is self-similar for length scales L smaller than ξ, even if $p \neq p_c$. In that regime, e.g., the total number of sites of the largest cluster scales as $M \propto L^{D_f}$, with a fractal dimension D_f. We have already seen that this can lead to a severe misinterpretation of measured data of reservoir rocks, when one is trying to simply upscale the fluid content of a small sample.

[6] For $p < p_c$ this length scale corresponds to the size of the largest cluster in the structure and for $p > p_c$ it gives the size of the largest hole.

[7] In three dimensions $\nu = 0.88$.

[8] The divergence of ξ at the percolation threshold means that the largest cluster just reaches infinite size, i.e., there is a sample-spanning cluster and the system is percolating.

In addition, the fractal nature of a porous medium also has a huge effect on transport properties, among which hydrodynamic dispersion stands out, as will be explained in the following paragraphs.

There are analogous scaling laws, that are also functions of $p-p_c$, for other percolation quantities like the accessible fraction $X^A(p) \propto (p-p_c)^{\beta_p}$, which gives the fraction of sites belonging to the sample-spanning cluster. The backbone fraction $X^B(p) \propto (p-p_c)^{\beta_B}$ is just the fraction of sites of the sample-spanning cluster that contribute to transport through the structure, neglecting the dead-end parts. The conductivity and the permeability follow similar power laws with different critical exponents.

In porous media terminology X^A corresponds to the open porosity ϕ_o and X^B to the backbone porosity ϕ_B. The critical exponents β_p and β_B are not equal. In two dimensions they amount to $\beta_p = 5/36$ and $\beta_B = 0.48$. This inequality[9] has very important consequences for transport through the structure and especially for hydrodynamic dispersion. Far off p_c, practically the whole sample-spanning cluster forms the backbone, i.e., there are very few isolated clusters and almost no dead ends. The closer we get to p_c, the larger the fraction of dead ends will be, because the critical exponent for X^B is larger than for X^A and, thus, the ratio $X^B/X^A \propto (p-p_c)^{\beta_B-\beta_p}$ approaches zero in the limit $p \to p_c$. Topologically speaking, the percolating cluster close to p_c will mainly consist of poorly connected dead ends and the backbone part will be highly tortuous. These effects result in a sharp increase of the dispersion coefficients close to p_c [47, 48, 49, 50]. Thinking again about the recoverable fluid content of reservoir rocks, further complications arise due to the presence of large dead ends. Most of the fluid can be trapped in such dead ends, from where it might not be recovered by simple means, e.g., trying to get it out by flushing with another fluid, because only the fluid in the backbone participates in flow, whereas the fluid in the dead ends stays trapped.

The aforementioned fractal dimension D_f of the cluster mass M can also be related to the critical exponents of the system. For $L < \xi$ the cluster mass scales as $M \propto X^A(p)\xi(p)^d \propto \xi(p)^{d-\beta_p/\nu}$. After replacing ξ by L, since this is the relevant length scale, we get $M \propto L^{d-\beta_p/\nu}$, from which follows $D_f = d - \beta_p/\nu$. Using the corresponding values for $d = 3$ dimensions we get $D_f \approx 2.53$, which is close to the values obtained for several sandstones [5].

Percolation theory has definitely been very useful to deepen the understanding of the structure as well as the flow and transport phenomena in porous media. Its application, however, is not straightforward, since the complete diagenetic process and, therefore, the percolation threshold of real porous media is not known and cannot be calculated unambiguously. Another problem is that far from the percolation threshold the universal behavior is lost and statistical properties of the considered structure can become dominating for the transport process. In this case, fortunately, critical path analysis, which is also formulated in terms of percolation theory, can lend a helping hand to identify the subset of the system, that makes the largest contribution to transport properties. For more details about percolation theory in combination with critical path analysis and several applications the reader is referred to [4].

[9] Also valid in three dimensions with $\beta_p = 0.41$ and $\beta_B = 1.05$.

2.4. Boolean models

Percolation theory, as briefly described in the last section, can also be extended from discrete to continuous space. Instead of just occupying sites on a lattice, objects of arbitrary shape are placed at random positions in an empty (unoccupied) space. In analogy to discrete percolation, the basic variable for continuum percolation theory will be the porosity ϕ instead of the occupation probability p. As with discrete percolation, a universal behavior for several quantities, i.e., functions of $\phi - \phi_c$, close to the percolation threshold ϕ_c will still be observed [51].

For the studies in this work we used two types of structures, both of which were generated by Boolean models, i.e., by randomly placed and oriented grains. The first type consists of randomly[10] placed overlapping monodisperse circles (ROMC) with constant radius r. For the second type randomly placed overlapping monodisperse ellipses (ROME) with constant aspect ratio $a/b = 8$, where a is the major axis and b is the minor axis, were used as individual grains.

Two exemplary series of such structures, which were created by Boolean models, are shown in Figure 2.9. The Boolean models were realized by a MATLAB program. Starting with an empty array of fixed size, pixelated versions of the grains were placed at random positions until the desired porosity ϕ or number of grains N was reached. The upper row shows ROMC structures with radius $r = 34\,px$ for increasing number of grains N or decreasing porosities down to their percolation threshold $\phi_{cc} \approx 0.32$. The lower row displays ROME structures with $a = 96\,px$ and $b = 8\,px$ down to their respective percolation threshold $\phi_{ce} \approx 0.66$. Intuitively, it is clear that structures formed by elongated grains overlap more frequently and, consequently, have a higher percolation threshold, i.e., fewer grains are required to disconnect both ends of the structure.

The diagenetic process of many porous media can be described by successively adding grains to the empty pore space, i.e., a Boolean process, that, albeit being very simple, can result in extremely complex morphologies. That is why Boolean models have frequently been used in the context of heterogeneous (porous) media, like wood fibre composites [52], porous ceramics [53] or concrete material [54], to explain the relation between the morphology of the pore space and physical properties. Samples of sedimentary rocks have been reconstructed by Boolean models with optimized parameters, which characterize the effective morphology of the porous structure. The resulting parameters were used to predict their transport and mechanical properties [55]. The accuracy of the predictions is astonishing, since the complex shape of the rock is reduced to an effective shape of the grains. Here, again, it is crucial that the sample, which is used to derive the effective shape, is large enough to include the properties of the whole medium.

One big advantage of such random structures with well-defined grains and precisely known formation process, besides their similarity to natural porous media, is that the geometrical and topological parameters can be calculated. These formerly discussed quantities, namely, porosity, surface area and Euler characteristic form a set of morpho-

[10] The probability density function for the coordinates of the grain centers is uniform over the whole sample, i.e., each position is equally likely.

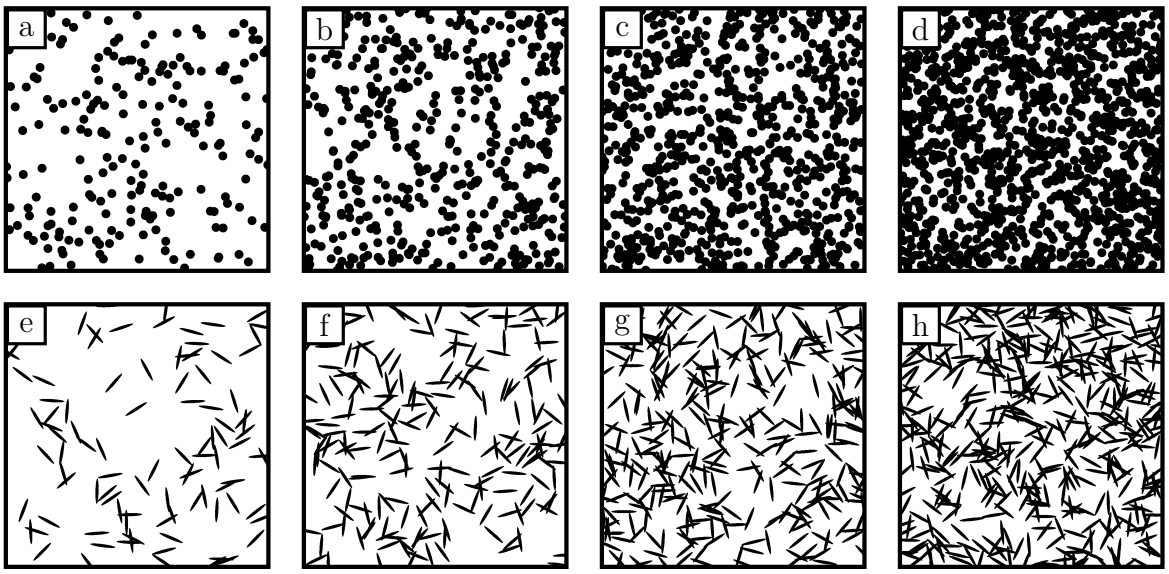

Figure 2.9.: Two series of ROMC (a-d) and ROME (e-h) structures of size $2000\,px \times 2000\,px$ with decreasing porosities (increasing number of grains N) down to their respective percolation thresholds $\phi_{cc} \approx 0.32$ and $\phi_{ce} \approx 0.66$. (a) $\phi = 0.83$, (b) $\phi = 0.66$, (c) $\phi = 0.49$ and (d) $\phi = 0.32$. (e) $\phi = 0.92$, (f) $\phi = 0.83$, (g) $\phi = 0.75$ and (h) $\phi = 0.66$.

logical measures, the so-called Minkowski functionals. These quantities are functions of the area A_0 and surface S_0 of the individual grains as well as the total number N of grains that form the structure [56, 57]:

$$\phi = \exp\left(-\frac{NA_0}{L^2}\right) \tag{2.5}$$

$$\frac{S}{L^2} = \frac{N}{L^2} S_0 \exp\left(-\frac{NA_0}{L^2}\right) \tag{2.6}$$

$$\frac{\chi}{L^2} = -\frac{N}{L^2}\left(1 - \frac{S_0^2 N}{4\pi L^2}\right) \exp\left(-\frac{NA_0}{L^2}\right). \tag{2.7}$$

These results only hold for truly continuous models. Pixelization errors, like in our structures, can lead to strong deviations even if the size of the structures is increased significantly [58]. Figs. 2.10 show results for ROMC structures with $r = 34\,px$ and ROME structures with $a = 96\,px$ and $b = 12\,px$ of size $8000\,px \times 8000\,px$. Fig. 2.10 (a) shows the porosity as a function of the number of grains N. The size parameters of the circles (black dots) and ellipses (red open squares) were chosen to result in an almost equal A_0[11] of circles and ellipses. The two curves practically collapse and follow an exponential law, just as predicted by Eq. (2.5). This is easily understood, because ϕ does not distinguish between volume enclosed by overlapping grains or volume that

[11] For the circles we get $A_{0c} = \pi r^2 \approx 3631,7\,px^2$ and for the ellipses $A_{0e} = \pi ab \approx 3619.1\,px^2$. Pixelization does not allow exact agreement.

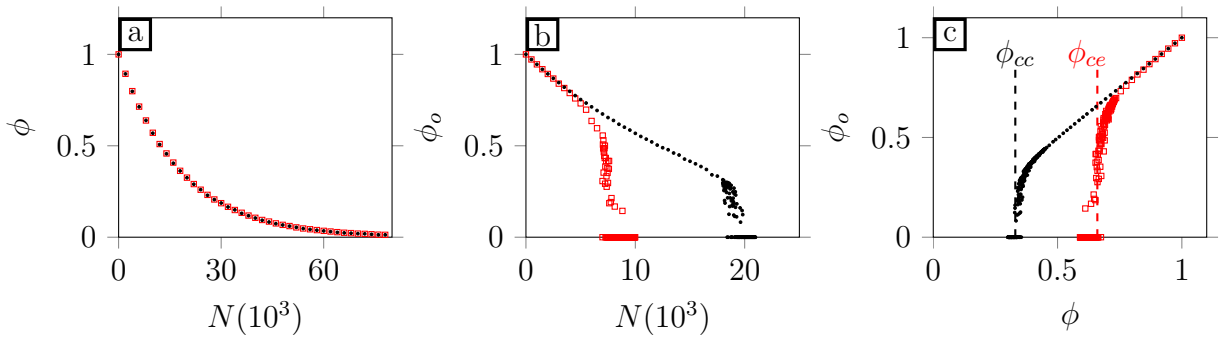

Figure 2.10.: Porosity ϕ and open porosity ϕ_o determined from ROMC ($r = 34\,px$) and ROME ($a = 96\,px, b = 12\,px$) structures. Red open squares correspond to ROME and black dots to ROMC structures. (a) ϕ vs. N, (b) ϕ_o vs. N and (c) ϕ_o vs. ϕ. In (b) and (c) the data points scatter due to the finite system size of $8000\,px \times 8000\,px$. The dashed lines in (c) indicate the percolation thresholds found in the literature [59, 60]. Close to the percolation thresholds the data points are scattering as a result of the finite size of the system.

spans the whole sample and, consequently, solely the area of the individual grains A_0 is of importance. Fig. 2.10 (b) displays quite a different behavior for the open porosity ϕ_o vs. N, which demonstrates the influence of the shape of the grains. For low N the grains do not overlap and, thus, ϕ_o depends linearly on N, just as ϕ does. For larger N grains will start to overlap and enclose some volume, which reduces ϕ_o. Fig. 2.10 (c) exhibits the same behavior for ϕ_0 vs. ϕ, but the transition at the percolation threshold is sharper because of the exponential dependence of $\phi(N)$. Both representations can be used to deduce the percolation threshold of the models. At a certain critical N_c the overlapping grains will disconnect the accessible volume of the structure and percolation will stop. For the circles this occurs at $N_{cc} \approx 19200$ corresponding to $\phi_{cc} \approx 0.336$ and for the ellipses at $N_{ce} \approx 7600$ or $\phi_{ce} \approx 0.651$, which is in good agreement with $\phi_{cc} \approx 0.32$ and $\phi_{ce} \approx 0.66$ found in the literature [59, 60]. As the correlation length of a system diverges at the percolation threshold ϕ_c, the system size should also be increased in order to avoid finite-size effects. However, any finite system and, therefore, any natural medium close to ϕ_c will be affected by finite size effects. These effects lead to a scattering of our data points close to the corresponding ϕ_c, which gives rise to a steady transition instead of an abrupt one. An infinite structure will not be percolating below its ϕ_c and will also always percolate if $\phi > \phi_c$. For a finite structure this is more difficult. There will still be a nonzero probability for percolation below ϕ_c as well as a nonzero probability that the structure is not percolating for $\phi > \phi_c$.

More details about the used structures will be provided, when the transport phenomena therein are investigated.

3. Fundamentals of flow and transport in porous media

The last chapter dealt with the parameters that characterize the static pore structure of a porous medium. The upcoming chapter is devoted to the flow and transport phenomena, that occur inside a complex porous matrix, and explains how the structure affects them. We start with the basic equations for flow of a Newtonian fluid inside an arbitrary geometry. These are the widely used Navier-Stokes equation and the continuity equation, which represent the flux of momentum and mass. Since the pore sizes of the structures used in this work, and also of many natural porous media, are on the scale of at most several micrometers, fluid flow is in the realm of microfluidics, in which the governing equation is the viscosity-dominated Stokes equation, a simplified form of the Navier-Stokes equation. The well-known dimensionless numbers, namely, Reynolds and Péclet number, that distinguish the different flow and transport regimes in porous media, i.e., whether the flow is dominated by inertia or if transport is mainly affected by diffusion, are also discussed at the appropriate time. For macroscopic samples one can again define averaged parameters, like permeability or dispersion coefficients, which have been studied intensively, both experimentally and theoretically. These quantities, which result from the microscopic processes described by the basic equations, incorporate the overall transport properties of porous media. There are several methods which are used for the estimation of the permeability. We discuss the underlying general ideas briefly and focus a little more on the afore-mentioned Katz-Thompson law that will be used in chapter 6. Diffusion, which is of importance for particle transport in porous media, especially in low-porosity structures, where a large number of stagnant areas can be found, together with the spatially varying velocity field, which is generated by the porous matrix, gives rise to hydrodynamic dispersion. The last sections address this important phenomenon and explain how it can be related to the pore space morphology.

For details and entertainment the curious reader should consult [61, 62, 3, 63].

3.1. Basic equations

The typical separation between molecules in a liquid is of the order 0.3 nm[1]. Thus, in porous media with pore sizes on the order of μm liquids can be treated as if they were continuously distributed in space. This continuity must not be taken for granted, because a porous medium might also have very small pores. For our introductory purposes, we nevertheless assume the requirements for a continuous treatment to be fulfilled.

[1]This is true for water. The separation varies for different liquids.

To know how a fluid moves at all times, we need equations, which give the three spatial velocity components $\boldsymbol{v}$, the pressure P and the density ρ at every point in space and at any time. Principally, there are also other interesting properties, such as conductivity, but we leave all of them aside and concentrate on the parameters above. We further reduce the complexity of our treatment by assuming that the fluid is Newtonian, i.e., it has a constant viscosity and is incompressible (has a constant mass density).

3.1.1. Continuity equation

The first relation, which basically represents the conservation of matter, is the hydrodynamic continuity equation:

$$\nabla\left(\rho\boldsymbol{v}\right) = -\frac{\partial\rho}{\partial t}. \tag{3.1}$$

The equation states that a mass flux $\rho\boldsymbol{v}$ out of a point will result in a reduced mass density ρ at that point. We already assumed that our fluids are incompressible, which means $\rho = const.$ and, consequently, the equation can be reduced to:

$$\nabla\boldsymbol{v} = 0. \tag{3.2}$$

This even simpler equation means that the velocity field $\boldsymbol{v}$ has zero divergence, i.e., there are no sources or sinks in $\boldsymbol{v}$. For the practitioner (3.2) is of great use to understand velocity fields. We look at, for example, a steady flow through a straight circular tube with varying diameter along its length. In that case (3.2) directly gives the average velocity across any slice of the tube. The narrower the tube, the faster the fluid must flow, as the product of area and velocity must be the same at any point[2]. Certainly, this is also true in a porous matrix, where a fluid will have to flow faster through narrow constrictions, so that (3.2) holds.

3.1.2. Navier-Stokes equation

The next important equation can be derived by starting with Newton's second law $d(\rho\boldsymbol{v})/dt = \boldsymbol{f}$ for a mass density ρ and a force density $\boldsymbol{f}$. The total differential[3] on the left-hand side can be split into two terms with partial derivatives. The force density on the right-hand side is written as the sum of three force densities. $-\nabla P$ is the pressure force, $\eta\nabla^2\boldsymbol{v}$ the viscous force due to shearing for a Newtonian liquid with constant viscosity, and $\boldsymbol{f_{ext}}$ stands for external forces, which could be gravity or an electrical force. Putting it all together, we get the Navier-Stokes equation:

$$\rho\left(\frac{\partial\boldsymbol{v}}{\partial t} + (\boldsymbol{v}\nabla)\boldsymbol{v}\right) = -\nabla P + \eta\nabla^2\boldsymbol{v} + \boldsymbol{f_{ext}}. \tag{3.3}$$

[2] Gauss' theorem states $\int\limits_V (\nabla\boldsymbol{v})\, dV = \oint\limits_{\partial V} \boldsymbol{v} d\boldsymbol{S}$, where V is a given volume and ∂V its surface. According to (3.2) both sides equal 0 and, thus, $v_1 A_1 = v_2 A_2$, with A_1 and A_2 being the area of a slice at two points, and v_1 and v_2 the average velocities in these areas.

[3] The total differential of $\boldsymbol{v}(x(t), y(t), z(t), t)$ is $d\boldsymbol{v} = \frac{\partial\boldsymbol{v}}{\partial x}dx + \frac{\partial\boldsymbol{v}}{\partial y}dy + \frac{\partial\boldsymbol{v}}{\partial z}dz + \frac{\partial\boldsymbol{v}}{\partial t}dt$. Division by dt gives $\frac{d\boldsymbol{v}}{dt} = \frac{\partial\boldsymbol{v}}{\partial x}v_x + \frac{\partial\boldsymbol{v}}{\partial y}v_y + \frac{\partial\boldsymbol{v}}{\partial z}v_z + \frac{\partial\boldsymbol{v}}{\partial t} = (\boldsymbol{v}\nabla)\boldsymbol{v} + \frac{\partial\boldsymbol{v}}{\partial t}$ with $v_{x,y,z} = \frac{d(x,y,z)}{dt}$.

$\partial \boldsymbol{v}/\partial t$ is just the acceleration of a fluid particle at a fixed point in space. Since we need the acceleration of a certain small volume of fluid during its motion, we have an additional term $(\boldsymbol{v}\nabla)\boldsymbol{v}$. One could, e.g., think of a superfluid ($\eta = 0$) flowing in a circle at a constant speed. Although $\partial \boldsymbol{v}/\partial t = \mathbf{0}$, as the velocity stays the same at each fixed point in space, a fluid element would have to be accelerated by a centripetal force during its motion, because it changes its direction at every instant.

Reynolds number

The flow of fluids is an intricate problem. To a large extent the complexity of the mathematical treatment of (3.3) arises from the non-linear term $\rho(\boldsymbol{v}\nabla)\boldsymbol{v}$, which represents inertial forces[4]. On the other hand, the non-linearity also gives rise to the richness of hydrodynamics, manifesting in, e.g., turbulent flow with chaotic vortices, whose description still is an unsolved problem. A simple and, unfortunately[5], still popular example of turbulent flow is rising cigarette smoke, which after an initial phase of laminar flow quickly becomes turbulent. Due to this complexity, solutions of (3.3) are only available for a few special cases.

The mostly small dimensions of porous media, however, can render the problem of fluid flow, or at least the equations for its description, considerably simpler, because flow at the micron scale is almost generally dominated by viscous forces, i.e., the non-linear term representing inertial forces can be neglected. The relative importance of the different terms can be quantified by dimensionless numbers.

Whether the fluidic system under consideration is in the inertial or viscous domain, can be judged by estimating the magnitude of the two corresponding forces. To this end, we introduce a length scale L and a velocity V, that characterize the system. The inertial forces are of the order $\rho(\boldsymbol{v}\nabla)\boldsymbol{v} \approx \rho V^2/L$ and the viscous forces $\eta\nabla^2\boldsymbol{v} \approx \eta V/L^2$. When the inertial forces are divided by the viscous forces, the famous Reynolds number results:

$$Re = \frac{\rho V L}{\eta} \tag{3.4}$$

For $Re \gg 1$, inertial forces dominate. This high Reynolds number regime is familiar to everyone from day-to-day life. We all know that our 130 feet motor yacht will not stop immediately, when we stop the engines, instead it will glide through the water, while its momentum is dissipating very slowly into the surrounding water. This is due to the inertial term, that is dominating in this regime. On the opposite side of the Reynolds number spectrum, that is, at $Re \ll 1$, which is the regime for bacteria and flow in microfluidic systems, the movement or flow will stop practically instantaneously, if the driving force vanishes. The motion of a bacterium will be entirely determined by the forces that it feels at that moment, the momentum it has built up is of no importance. If the propulsion stops, the bacterium stops immediately[6]. This behavior obviously totally contradicts standard intuition about the motion of macroscopic objects and,

[4] For brevity, we will not distinguish between forces and force densities.

[5] "On average, cigarette smokers die about 10 years younger than non-smokers" [64].

[6] The inertial time scale τ_i can be estimated by balancing the time-dependent term $\rho\frac{\partial \boldsymbol{v}}{\partial t}$ with the viscous

thus, exemplifies that one must be extra cautious when dealing with flow phenomena at the micron scale.

The typical length and velocity scale for the systems we used are $V \approx 1\,mm/s$ and $L \approx 5\,\mu m$. In combination with the viscosity of water at room temperature $\eta \approx 1\,mPas$ and its density $\rho \approx 1000\,kg/m^3$, a Reynolds number of less than 10^{-2} results, which makes certain that flow is in the predictable (non-turbulent) laminar regime.

Let us not forget to mention the huge practical implication of the Reynolds number. Two flow phenomena at the same Re will behave alike on their respective length and time scales. So, if we want to know how a big ship, say 130 feet long, behaves, we can build a small model of this ship, say 1.3 feet long, and increase the velocity by a factor of 100, which would result in the same Re. And yet, it is not that simple, because we have neglected the compressibility of the fluid, which can become crucial, as the velocity approaches the speed of sound.

3.1.3. Stokes equation

Judged by the estimate for the Reynolds number for our systems, we are strictly in the regime of viscous forces, that is, laminar flow. Consequently, at such low Re, the inertial term $\rho(\boldsymbol{v}\nabla)\boldsymbol{v}$ can be neglected. The linear first term $\rho\partial\boldsymbol{v}/\partial t$ gives an inertial time scale τ_i for the establishment of a steady flow. We can estimate τ_i by balancing the linear inertial term with the viscous term, which yields $\tau_i \approx \rho L^2/\eta$. This time scale is on the order of μs and, therefore, the linear term can also be left out, as long as we do not use rapidly oscillating flows, i.e., as long as any other time scale in the system is significantly larger than τ_i. Now, omitting these terms greatly simplifies (3.3) and gives the so-called Stokes equation:

$$\mathbf{0} = -\nabla P + \eta\nabla^2\boldsymbol{v} \tag{3.5}$$

This is the equation for creeping flow ($Re \ll 1$). For simplicity, the external forces were also not included. What immediately strikes the eye is that, in contrast to (3.3), the Stokes equation contains no time derivative. As a consequence, the solutions of (3.5) are symmetric in time. So, if all forces and pressures are reversed, the flow of the fluid will also be reversed. For an illustration of this time symmetry, one can use a low-Reynolds-number system, inject a blob of dye at some position and apply a pressure for some time to make the fluid flow. The dye will spread out following different streamlines. Now, if the pressure is reversed for the same time interval, the dye will take the same path again, but in the other direction. Therefore, astonishingly and totally counterintuitively, in the end the same dye blob we started with will show up again at the same position. To be precise, it will not be exactly the same, because diffusion is not symmetric in time, so its boundaries will be a little blurred. We can move the fluid back and forth, fast or slow, and still an almost identical blob will result. At high Reynolds numbers such a behavior will not be observed due to turbulent mixing which results from the non-linearity.

term $\eta\nabla^2\boldsymbol{v}$ which yields $\frac{\rho V}{\tau_i} = \frac{\eta V}{L^2}$, eventually giving $\tau_i = \frac{\rho L^2}{\eta}$. For an object of size $L = 1\,\mu m$ this would result in $\tau_i = 1\,\mu s$.

In figure 3.1 (a) streamlines around a cylinder are illustrated for two widely differing Reynolds numbers. The upper cylinder shows smooth streamlines at low Reynolds number. The streamlines do not intersect and the velocity of the fluid at any point is constant over time. If we reverse the flow, all streamlines will just reverse their direction, i.e., the flow field is mirror symmetric. This explains the effect we have discussed in the last paragraph. The flow around the cylinder in the lower part at very high Reynolds number shows a very different behavior. Behind the cylinder, the streamlines show turbulent behavior like streamline crossing and the occurrence of vortices. The use of the word "behind" already states that the symmetry is broken. If the flow is going into the other direction, the vortices will also occur on the other side of the cylinder. The experiment with the dye blob would obviously not work, as the turbulence would mix different streamlines. In between the two extreme cases shown there are an infinite number of steps, the transition from laminar to turbulent flow proceeds in a steady way with increasing Reynolds number.

Despite the loss of complexity due to inertial irrelevance, fluid flow at the micron scale poses many interesting new challenges [65, 66]. In the case of porous media the complexity of flow phenomena persists due to the disordered pore space, which does not allow for a straightforward calculation of the flow properties, albeit the basic equations (3.5) seem to be quite simple. It is not only the irregularity of the pores, but also the addition of diffusion, which will be important for the transport of particles, that turns simple creeping flow through porous media into a tough task.

Infinite parallel-plate channel

Even with the much simpler Stokes equation, solutions for flow problems inside complex boundaries are hard to calculate. We will restrict ourselves to just one example of steady state, pressure-driven flow, also known as Poiseuille flow, which is central for microfluidics and also for flow in the artificially created porous structures that are used in this work. In a microfluidic system the aspect ratios of the channels can often be so large that a good approximation of their geometry is given by an infinite[7] parallel-plate channel. As a result of the high symmetry, this problem can be solved very easily. A sketch of such a flat channel is shown in Figure 3.1. The two confining walls lie in the xy-plane and are located at $z = 0$ and $z = h$, so h is the height of the channel. The black arrow indicates a constant pressure gradient $-\nabla P$ that is applied in the x direction. The symmetry of the problem implies that only the x-component of $\boldsymbol{v}$ is nonzero and that this component v_x can only be a function of the z coordinate. Consequently, the relevant Stokes equation for this problem reads as:

$$\frac{\partial^2 v_x}{\partial z^2} = \frac{\nabla P}{\eta}. \tag{3.6}$$

We assume that the no-slip boundary condition holds, i.e., the fluid at the wall is at rest ($v_x(0) = v_x(h) = 0$). Twofold integration of v_x yields:

[7] The only boundaries of such a channel are the plates at the top and at the bottom. The aspect ratio, that is, the width-to-height ratio, therefore, is infinite.

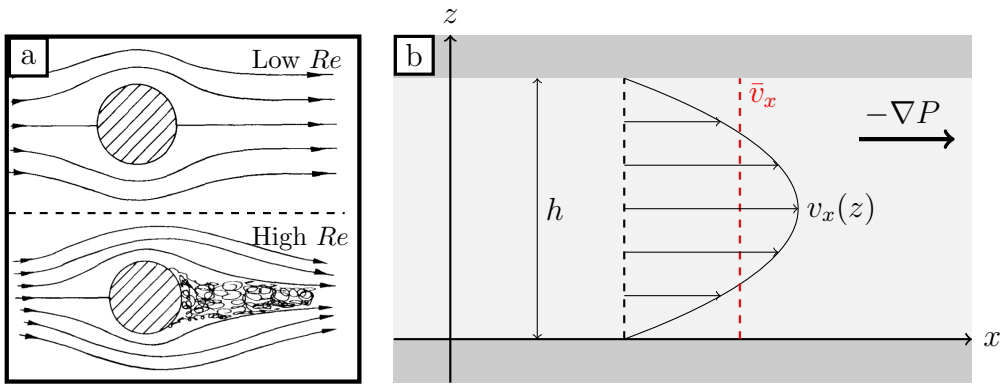

Figure 3.1.: (a) (Upper half) Flow past a cylinder at low Reynolds number. The flow is strictly laminar. (Lower half) At a higher Reynolds number the flow becomes turbulent, i.e., the streamlines are not mirror symmetric and the velocity at any point varies over time. (b) Sketch of a xz-plane in an infinite parallel-plate channel of height h bounded by two walls (darker gray), in which a flow in x-direction is generated by a constant pressure gradient $-\nabla P$. The resulting velocity profile $v_x(z)$ (solid black line) has a parabolic shape, i.e., fluid close to the center flows fastest. The red dashed line corresponds to the mean velocity $\bar{v}_x$. [63]

$$v_x = \frac{\nabla P}{2\eta} z(z-h) \tag{3.7}$$

The velocity profile is a parabola with maximum value $\hat{v}_x = \frac{-\nabla P}{8\eta} h^2$ right in the middle of the channel, at $z = h/2$. The mean value equals $\bar{v}_x = \frac{1}{h}\int_0^h v_x(z)dz = \frac{-\nabla P}{12\eta} h^2$. These values are good approximations for channels with high aspect ratios. A general analytical solution for a rectangular channel with finite aspect ratio is not known, but a solution can be written as a Fourier series [63]. Note also, that this result is very similar to the well-known Hagen-Poiseuille flow through a circular pipe. For a circular pipe of radius R, the mean flow velocity would be $\bar{v}_{circ} = \frac{-\nabla P}{8\eta} R^2$. A circle is the most compact shape, that is, it has the lowest surface-to-area ratio, which also results in the greatest ease, highest permeability, for flow. Any other shape with the same area has a larger surface that causes resistance to flow.

3.2. Permeability

3.2.1. Darcy's law

We have already seen in the previous chapter that the pore structure of porous media is much more complicated than the simple straight pipes just discussed. For this reason and the fact that the detailed pore structure of many porous media is not known in the first place, even the relatively simple Stokes equation cannot be solved. Yet, the flow of a Newtonian liquid inside a porous medium at steady-state conditions often still is in

the low Reynolds number regime, for which Darcy's law[8] is applicable:

$$Q = \bar{v}A = \frac{kA}{\eta}\frac{\Delta P}{L}. \tag{3.8}$$

Here, $\bar{v}$ is the average flow velocity, Q the volumetric flow rate, k the permeability, A the cross-sectional area of the sample and ΔP the pressure drop across a length L of the considered medium. Darcy's law relates the applied pressure to the flow rate or flow velocity by a proportionality constant, namely the permeability, that can be measured experimentally and incorporates the overall hydrodynamic conductivity of a porous medium. This is completely analogous to Ohm's law, which connects current density and applied electric field via conductivity.

Several theoretical derivations under steady-state conditions for Darcy's law, which use the Stokes and the continuity equation as well as the no-slip boundary condition, have been presented [1, 68, 69]. Thus, the validity of Darcy's law is limited by the validity of the Stokes equation, which only holds at low Reynolds numbers ($Re \leq 10$), and the validity of the no-slip boundary condition. If the pressure gradient is increased beyond a critical pressure, a transition from laminar to turbulent flow will occur and the relation between pressure gradient and velocity will cease to be linear, i.e., doubling the pressure will not suffice to double the flow rate, because more energy will be dissipated by turbulence. The value of the critical pressure will certainly depend on some characteristic length scale of the pore space. This phenomenon has also been studied numerically [70] and theoretically [71, 72].

Complications also arise at the other end of the Reynolds-number spectrum. Some researchers discuss a lower limit for the applicability of Darcy's law, where the pressure might first have to reach a threshold value until flow starts and from then on increases non-linearly before reaching the Darcy regime [73]. The reason for this are strong surface forces which might counteract some of the applied pressure in dense porous media. In addition, the no-slip boundary condition might not hold for porous media in which the pore sizes are comparable to the mean intermolecular distance of the fluid particles. In that case molecules can flow on the pore surfaces[9], which violates the no-slip condition. The different possible flow regimes are illustrated (in an exaggerated way, for clarity) by the blue line in Figure 3.2.

To avoid any confusion later on, we briefly explain the ostensibly trivial meanings of some variables that occur in (3.8). As the average velocity in (3.8) is the value that results from averaging over the whole sample, including isolated pores, stagnant parts and the solid matrix, $\bar{v}$ must not be mistaken for the average velocity of the fluid in the pore space. This average fluid velocity, which must be higher due to continuity requirements, is obtained by dividing $\bar{v}$ by the porosity ϕ. But this value, again, does probably

[8] Named after the French engineer Henry Darcy (1803-1858), who discovered the similarity between ground-water flow and creeping flow in pipes [67]. Darcy, despite his ingenuity, was not aware of the fact, that the flow rate also depends on the viscosity of the fluid. This should again remind us that things which are "clear" to us now were not obvious at all.

[9] The importance of this effect is measured by the Knudsen number $Kn = \frac{\lambda}{L}$, which relates the mean free path of the molecules λ to a characteristic length scale of the pores L.

not give the wanted information, because when talking about the velocity of the fluid, it makes perfect sense to consider only the part that is actually flowing, and, thus, to divide $\bar{v}$ by the backbone porosity ϕ_b, because only this part is actually contributing to flow. Intriguingly, this means that as one approaches the percolation threshold of the structure, where the backbone will become arbitrarily small, the corresponding value for the average backbone velocity must diverge at finite flow rates. Thus, we already see the intricacies arising from the complex pore structure. One should also understand that the permeability is a specific quantity of the porous medium, which does not depend on its size, if the medium is homogeneous. Doubling the cross-sectional area of a homogeneous medium will also double the flow rate, but the average velocity and therefore the permeability stays the same. We can use the flat channel as an example to illustrate these points. The average velocity in the flat channel amounted to $\bar{v}_x = \frac{1}{h}\int_0^h v_x(z)dz = \frac{-\nabla P}{12\eta}h^2$. We can compare this result to (3.8), where the pressure gradient $\nabla P = -\Delta P/L$ is just written another way, and get a permeability of $k = h^2/12$ for a flat channel. This is an important result that we will encounter again, when we discuss the transport properties of Boolean models in chapter 5. When we now just put two of these channels on top of each other, the permeability of the resulting structure will still be the same, but the cross-sectional area will have doubled and, accordingly, the volumetric flow rate will also be twice as large. If, however, we double the cross-sectional area by doubling the height of the channel, the permeability will increase fourfold and the flow rate even by a factor of eight[10]. We hope that with these explanations the different meanings of the variables are clarified.

Experimentally, the permeability can, in principle, be determined by measuring the flow rate Q or average velocity $\bar{v}$ at just one constant pressure drop ΔP. Such a procedure, however, could easily result in a substantial experimental error, so that it is advisable to repeat the measurement at several different ΔP and plot $\bar{v}$ versus ΔP. If the measurement is in the Darcy regime, the data points should follow a straight line, like the ones shown in Figure 3.2. Otherwise one should look for the cause of the deviation. The regression line should also pass through the origin. The slope of this line will yield the permeability[11] k. In chapter 5 we will also discuss another practical method that makes use of an exponentially decaying pressure drop to determine the permeability. This method has certain advantages, if one employs tracer particles to measure the flow velocities.

One of the main goals in the study of porous media is to predict the permeability for a given porous medium, i.e., a given pore space morphology. With other things being the same, a porous medium with higher porosity ϕ, or more precisely a larger backbone area, will have a higher permeability. Apart from such general and trivial statements, which often may be relatively useless, several expressions for the permeability of porous media have been proposed in the literature [3]. Here, we will not investigate them in

[10] The permeability is proportional to h^2, so it increases by a factor of four when h is doubled. The flow rate increases by a factor of eight, as it is proportional to $h^2 A$ and the cross-sectional area also doubles when doubling the height.

[11] The slope will correspond to $\frac{k}{L\eta}$, to be precise.

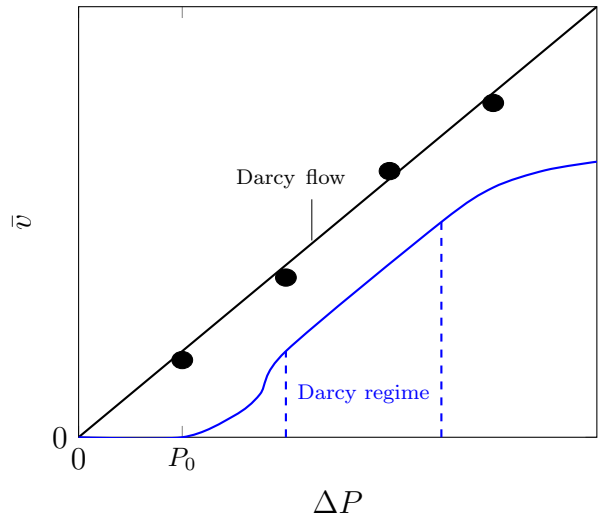

Figure 3.2.: Typical measured data points (black circles) for flow velocities $\bar{v}$ in a porous medium at different applied pressure drops ΔP. The regression line (black) shows a perfectly Darcian behavior, i.e., a linear relation between $\bar{v}$ and ΔP without offset. The blue line shows an exaggerated behavior to illustrate the different possible flow regimes. Up to a threshold pressure drop P_0 there is no flow. Next a non-linear regime follows, which ends in the linear Darcy regime. At high P a transition to turbulent flow occurs, giving rise to additional energy dissipation and, logically, a lower rate of velocity gain [73].

detail but only give a short overview of some general ideas.

There is, for example, a very elegant and instructive way to calculate the permeability as a function of the porosity for a porous medium consisting of randomly placed but not overlapping and well-separated spheres, that is, the permeability in the high-porosity limit. Imagine that the upper half of figure 3.1 (a) showed a cross section of a fixed sphere in a steady-state flow at low Reynolds number. We know that Stokes' law states that a sphere in a homogeneous flow of velocity v_0 (at infinite distance from the sphere) will feel a force $F_{drag} = 6\pi\eta a v_0$, with a being the radius of the sphere. Let us suppose that the medium consists of N spheres in a volume V. The corresponding number density of the spheres in the medium is $\rho = N/V$. Adding up the forces on all spheres and dividing by the volume leads to a pressure gradient $\nabla P = \rho F_{drag}$[12]. The volume fraction of the spheres is $\phi_2 = \rho 4\pi a^3/3$, which is related to the porosity of the medium by $\phi = 1 - \phi_2$. If the pressure gradient is put into (3.8) and the density is written in terms of ϕ_2, we finally get the so-called Stokes permeability[13] $k_S = 2a^2/(9\phi_2) = 2a^2/(9 - 9\phi)$

[12]The total force is $F_{tot} = NF_{drag}$, just number of spheres multiplied by the force on one sphere. The pressure drop caused by the spheres will then be $\Delta P = \frac{F_{tot}}{A}$, where A is the cross-sectional area of the medium perpendicular to the flow. When this pressure drop is divided by the length L of the medium, the pressure gradient $\nabla P = \frac{\Delta P}{L} = \frac{F_{tot}}{AL} = \frac{NF_{drag}}{V} = \rho F_{drag}$ results.

[13]Darcy's law states that $v_0 = \frac{k_S}{\eta}\nabla P$. We put in the pressure gradient $\nabla P = \rho F_{drag} = \rho 6\pi\eta a v_0$ and solve the equation for k_S, which gives $k_S = \frac{a}{6\pi\rho}$. The last step is to use $\phi_2 = \rho\frac{4\pi a^3}{3}$ to replace ρ and end up with the Stokes permeability $k_S = \frac{2a^2}{9\phi_2}$

[3]. This result, however, is only valid in the diluted case where the individual spheres are so far apart that they do not interact with each other. It is also apparent that the spheres that make up the medium are freely floating in space, so this whole concept has to be understood as a purely theoretical construct, which would not be observed in nature.

Starting with the diluted case for which we calculated the Stokes permeability, the assumption of non-interacting, i.e., well-separated obstacles in the structure was loosened step by step by incorporating the effect of more and more nearby obstacles, which will disturb the local flow field and lead to deviations from the diluted limit. The first exact results were reported for periodic arrays of spheres on simple lattices [74]. Obviously, such periodic structures are still a lot simpler than natural random porous media, as they can be described by at most a few numbers and the problem is solved once a solution for one elementary cell has been found. These results might help a little to understand the flow behavior in real porous media or, in general, more complex morphologies, but cannot really be used to predict their permeability in a reliable manner. The permeability of random arrays of fixed spheres were also calculated [75, 76]. These results already came a little closer to the problem of flow through a natural disordered structure, but the common problem with all of these approaches is that all these arrangements of spheres or grains of other shapes form unconsolidated materials where each individual grain is still visible. There is no overlap between individual grains and, thus, such models do not show resemblance to many consolidated natural rocks.

Here, a few words should be added about an empirical and often-quoted formula for the permeability of a porous medium. The Kozeny-Carman equation expresses the permeability k in terms of the Stokes permeability k_S as a function of the porosity:

$$\frac{k_S}{k} = \frac{10(1-\phi)}{\phi^3}. \tag{3.9}$$

Quite astonishingly, this very simple formula is in good agreement with periodic as well as random-sphere packings at low porosities ($\phi \leq 0.5$) [3, 77]. Yet, in general, (3.9) is very inaccurate for heterogeneous structures [78], which is to be expected as it is derived by assuming that the pore space consists of non-intersecting tubes, completely ignoring the interconnectedness of the pores.

We already said that a real porous medium has a more complicated structure, which often does not show much resemblance to packings of spheres. The features of such natural structures, however, can also be described by other simple models, e.g., Boolean models that were introduced at the end of the last chapter. The fundamental difference is that the individual grains are allowed to overlap and, therefore, form a consolidated and more complicated structure. The problem with such structures is that it is not straightforward to derive a general equation for their flow and transport properties. In fact, there is no exact result for the permeability of an arbitrary pore space and due to the complexity of the morphology one cannot expect a simple expression that accounts for all the features of a disordered porous medium.

An overview of the most common empirical and semi-empirical expressions for the permeability of disordered porous media can be found in the literature [1, 3, 77]. We

settle for just one interesting idea that also illustrates the difficulties that arise when trying to find a general relation for the permeability and then turn to the expression that will form the starting point for following investigations in later chapters.

For particles that diffuse in a d-dimensional porous medium, an effective diffusion constant D_e can be defined via $\langle \boldsymbol{r}^2(t) \rangle = 2dD_e t$, where $\langle \boldsymbol{r}^2(t) \rangle$ is the mean squared displacement of the particles. Einstein's relation states that the effective conductivity σ_e is proportional to the effective diffusivity, so $\sigma_e \propto D_e$. By simulating the motion of random walkers inside porous matrices numerically, the diffusivity and, hence, the conductivity can be obtained [79, 80, 81]. The results for the electrical conductivity, which were obtained with such random-walk simulations [82], were in very good agreement with experiments [83]. Our goal, however, is to find the permeability of a porous medium. The fact of the matter is that there is no general relation between permeability and electrical conductivity or diffusivity of a porous medium. This is not surprising since the equation that has to be solved in case of the diffusivity or conductivity is a scalar one (Laplace equation), whereas in the case of permeability one deals with a vector equation (Stokes equation, for our purposes). Probably the easiest way of understanding why there is a fundamental difference between electrical conduction and fluid flow is to think about liquid flowing through a circular pipe of radius r. We already know that the volumetric flow rate is proportional to r^4. On the other hand, the electric current through such a pipe is proportional to r^2, which clarifies that there cannot be a simple relation between the two phenomena for an arbitrary structure.

3.2.2. Katz-Thompson law

One widely-used and well-founded semi-empirical expression that relates the permeability of a structure and its conductivity is the Katz-Thompson equation:

$$k = c l_c^2 \frac{\sigma_e}{\sigma_0}. \tag{3.10}$$

Here, c is a constant related to the local pore geometry and l_c is the size of the critical pore. The ratio of the effective conductivity σ_e of the porous medium, saturated with some fluid of conductivity σ_0, and its bulk conductivity σ_0 is called formation factor. The formation factor is a measure of the connectivity of the pore space. The better connected the pores are, the higher the formation factor is. The critical size l_c has already been mentioned in 2.2. The Katz-Thompson law is motivated by the arguments used in critical path analysis, i.e., the idea that most of the pore space can be ignored, because only a few paths dominate the overall flow and transport properties. Effectively, the problem of flow through a porous structure is reduced to a percolation problem with threshold pore size l_c, i.e., the pore size below which there is no sample-spanning cluster of connected pores. The critical pore size l_c is the size of the smallest pore along the sample-spanning paths with the least resistance to flow. Since all the other paths have a much higher resistance to flow, especially when the pore-size distribution is broad and the coordination number is low, this size determines the magnitude of the permeability of the porous structure and, logically, has to appear in (3.10).

One strong point of the Katz-Thompson law is its practicality as both the effective conductivity σ_e and the critical pore size l_c can be measured directly and unequivocally. After saturating the porous medium with some fluid of bulk conductivity σ_0, the conductivity of the porous structure can be measured, which gives the formation factor. The critical pore size can be extracted from the capillary pressure curve, which shows a very steep rise at the inflection point where the mercury first (see again Figure 2.2) forms a sample-spanning cluster. This point is experimentally well-defined, because it also coincides with the formation of electrical continuity in the sample. By making use of the Washburn equation, a critical pore size can be calculated from the corresponding pressure. So, the Katz-Thompson model has no adjustable parameters but only uses measurable quantities. The calculated permeabilities for a set of 50 rocks ranging over 5 orders of magnitude were in very good agreement with measured values, which clearly demonstrates the merit of this model [35]. Another advantage of this model is that it does not rest on any structural information, that can only be obtained if the precise morphology of the whole considered porous medium is known. All necessary parameters can be measured and, thus, the permeability can be calculated without looking inside the porous medium.

We will use the Katz-Thompson law in section 6.2 as a starting point to derive a geometrically motivated expression for the permeability of Boolean models.

3.3. Hydrodynamic dispersion

Up to now, we have only discussed flow of one continuous fluid phase through a porous structure and the properties of fluid transport were characterized in terms of average quantities, such as mean flow velocities or the related permeabilities. Yet, in a natural setting, the more general situation involves at least one other fluid phase or small particles that are transported through the structure[14]. From an experimentalist's point of view it is also understandable that one needs some kind of probe to render the local movement of the fluid measurable, if flow inside porous media is to be investigated. This can be accomplished by using some kind of tracer, e.g., a dye or, as in this work, small particles that are dispersed in the fluid.

The resulting complexity of such multi-phase flows may be visualized by injecting a small drop of dye into a fluid that is flowing through a porous medium. The initially sharply localized dye will spread apart as it travels downstream through the structure. This spreading apart goes by the name hydrodynamic dispersion. It is the result of the combined actions of a nonuniform velocity field, which is a result of the disordered morphology of the porous medium, and molecular diffusion.

Hydrodynamic dispersion plays an important role in many fields such as enhanced oil recovery, groundwater pollution, biological processes and the in situ study of aquifers, where one method of determining the characteristics of such fluid-bearing rocks is to

[14]One could also just think about following individual particles of the fluid, i.e., individual water molecules, which would feel the varying velocity field but would also diffuse around and thereby switch to other streamlines.

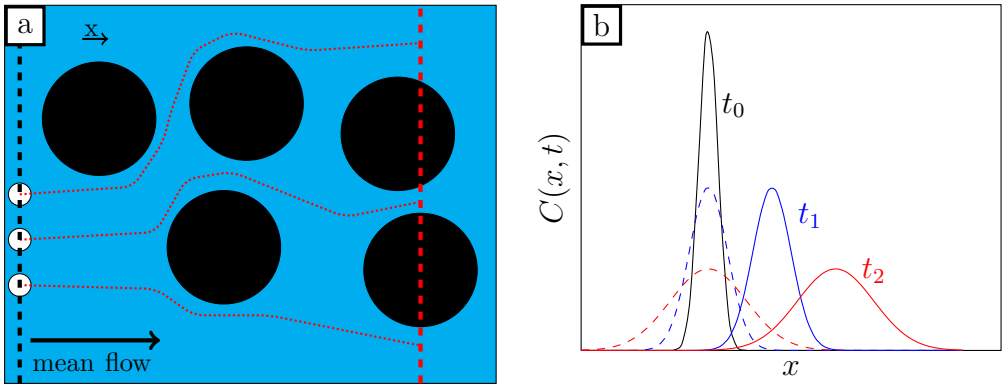

Figure 3.3.: (a) Illustration of a porous medium in which a suspension of small particles is flowing. All particle trajectories start in an entrance plane (black dashed line) and end in an exit plane (red dashed line). Their respective trajectories follow paths of different lengths and are also transported with varying velocities. Consequently, the particle front will spread out as the particles pass through the structure. The resulting first-passage time distribution quantifies longitudinal dispersion in the porous medium [85]. (b) Time development of an initial particle distribution $C(x, t_0)$. Without flow (dashed lines) the particles just spread out under the action of diffusion, but do not move on average. If a flow is present (solid lines), the distributions will also move in the direction of the mean flow with the mean flow velocity. Usually, the distributions also broaden faster when there is a flow.

inject tracer particles and measure their first-passage time distribution (FPTD) [84, 3], i.e., the distribution of transit times between an entrance and exit plane. Obviously, such a distribution will be a more sensitive measure of porous structure as, e.g., the permeability, because it includes the effect of individual particles and not just an averaged quantity. We will explain the basic transport mechanisms to get an insight into the phenomenon of hydrodynamic dispersion and thereby deepen our understanding of the role of pore space morphology for fluid flow through porous media.

3.3.1. Mechanisms of dispersion

An illustration of a porous medium is given in figure 3.3, where particles along with their respective trajectories are shown. The mean direction of flow is from left to right. As can be seen, the particles take different paths as they travel through the structure. Let us first focus on the high-velocity case, i.e., the effect of diffusion, caused by random molecular motions, can be neglected so that all particles stay on the same streamline. This regime is called mechanical dispersion. The boundaries of the porous medium will affect the transport of particles in several ways. First, the velocity on the surface of the porous matrix is zero, which leads to a varying velocity across a pore (recall figure 3.1(b)). Second, the velocity from pore to pore is also varying, since the pores have different diameters and different pressure drops across them, which can result in a highly nonuniform velocity field in the porous medium. Third, the lengths of the trajectories between entrance and exit plane also differ strongly, as streamlines can follow tortuous

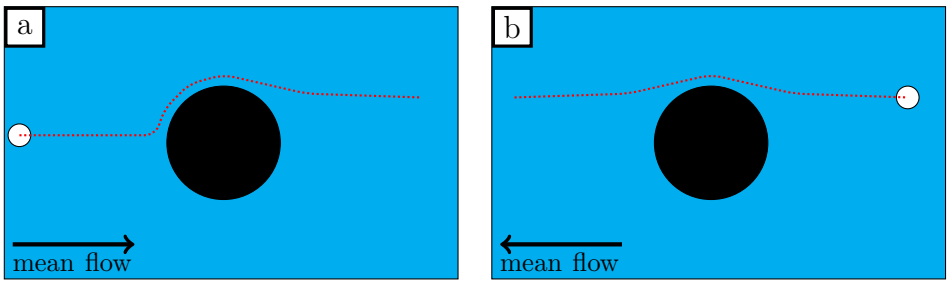

Figure 3.4.: (a) A particle that is moving to the right is displaced to another streamline due to steric repulsion. (b) If the flow direction is reversed, the particle will not move back to its initial position but follow its new streamline.

paths through the porous structure. Therefore, particles that start at the same time in an entrance plane (black dashed line) will reach the exit plane (red dashed line) after different transit times, which will result in a broad FPTD. In other words, initially adjacent particles will spread out due to the variations in velocities and trajectory lengths. This spreading is normally split up in two parts, namely, a longitudinal component in the direction of the mean flow, and a transverse component perpendicular to the mean flow direction. The FPTD quantifies the longitudinal dispersion in the porous medium. We will mainly concentrate on this aspect of dispersion and neglect transversal dispersion.

There is one more interesting aspect that concerns transport of particles through porous structures. We look at figure 7.8 which shows a particle that is passing by an obstacle. Due to the finite size of the spherical particle, its center of mass cannot come closer to the obstacle than its radius. Therefore, the particle experiences an irreversible force in the form of steric repulsion that leads to its displacement to another streamline, as illustrated in figure 7.8 (a). If the flow is reversed, as shown in figure 7.8 (b), the particle will stay on its new streamline, and, therefore, not move back to its initial position. This phenomenon can break time reversibility for particles even for creeping flow, which is described by the time reversible Stokes equation. One convincing example of this effect is particle separation [86, 87, 88]. In porous media, the streamline crossing of finite particles by steric repulsion can enhance but also hamper dispersion, depending on the pore structure and the size of the particles. Large particles might also be excluded from some parts, e.g., stagnant parts of the porous medium, by such steric effects and be transported faster through the structure as a result [89].

3.3.2. Diffusion and advection

Mechanical dispersion, as described above, is modified by the presence of molecular diffusion, which can move a small particle or a molecule from one streamline to another. In the absence of diffusion[15], a particle will just be advected by the surrounding fluid along a streamline, which it will never leave. Logically, molecular diffusion is of crucial

[15]Certainly, this is only a hypothetical thought, since there is no way to completely avoid diffusion. But at very high flow velocities, diffusion will become less important.

importance for particles that are in slowly flowing or stagnant regions of the pore space, where diffusion is the dominant or only means of transport.

If one starts with an initial distribution of particles at a certain time $C(\boldsymbol{r}, t)$[16], the time development of this distribution can be described by Fick's second law of diffusion:

$$\frac{\partial C(\boldsymbol{r}, t)}{\partial t} = D_m \nabla^2 C(\boldsymbol{r}, t). \tag{3.11}$$

The diffusion coefficient D_m is given by the Stokes-Einstein equation, $D_m = \frac{k_B T}{6\pi\eta a}$ [90].

When the initial distribution at $t = 0$ is a Dirac delta function, i.e., all particles start at the origin, the normalized solution of this equation is a Gaussian distribution:

$$C(\boldsymbol{r}, t) = \frac{1}{(4\pi D_m t)^{3/2}} \exp\left[- \frac{\boldsymbol{r}^2}{4 D_m t} \right]. \tag{3.12}$$

This equation describes the effect of molecular diffusion, which mixes different solvents or spreads particles out, even if there is no flow. Therefore, this kind of mixing is independent of the flow velocity. Figure 3.3 (b) shows how an initially sharp distribution (solid black line) broadens over time (dashed lines). If the area in which the particles or solutes are dispersed is bounded, diffusion will finally lead to an even distribution, given enough time. This is an important statement, it means that in the long-time limit a particle that starts at some specific point in a bounded porous medium, will be found with the same probability at any position in that medium. A concentration profile with a lot of bumps in it will become smoother as time goes by, that is, areas that initially had a low concentration will have a higher concentration and vice versa.

Just as we have discussed pure diffusion without any other effects, which is described by (3.11), we can look at the other extreme, where there is no diffusion and the particles or the solutes studied are only advected in a homogeneous flow field. We can write down a transport equation for that case:

$$\frac{\partial C(\boldsymbol{r}, t)}{\partial t} + \bar{\boldsymbol{v}} \nabla C(\boldsymbol{r}, t) = 0 \tag{3.13}$$

This equation just moves the initial distribution $C(\boldsymbol{r}, t)$ in the direction of $\bar{\boldsymbol{v}}$ without changing its shape. This, of course, is unrealistic in a porous medium where there are many different paths and widely varying velocities, but still the center of mass of the distribution moves with the average flow velocity.

Péclet number

The relative importance of advection and diffusion is measured by another dimensionless number, the Péclet number Pe. In order to calculate Pe, we need a characteristic length scale of the porous medium L, where often the mean diameter of an individual grain of the porous medium is used, a typical velocity V in the porous medium, and

[16] Instead of the letter C, which is normally chosen, if the spreading of a solute concentration is studied, one could also think about a probability P to find a particle around a certain position in space.

a diffusion coefficient D[17]. Now the relative strength of the two transport mechanisms can be quantified by calculating the ratio of the time it needs a particle to travel a distance L by diffusion $\tau_{diff} = L^2/D$ and the time it takes the particle to travel that same distance by advection $\tau_{adv} = L/V$. So, we get $Pe = \tau_{diff}/\tau_{adv} = LV/D$. At $Pe \ll 1$ the transport is totally dominated by diffusion, whereas at $Pe \gg 1$, diffusion is practically meaningless and advection is in control of transport. A transition from diffusive to advective transport is expected to occur at $Pe \approx 1$. Although it seems that the distinction between the two transport regimes is a no-brainer with the Pe, it is far from that, because, e.g., knowing what the relevant length scale of a porous medium is, can be a tough task, if the structure contains large stagnant parts. We will come back to this point in chapter 7.

3.3.3. Advection-diffusion equation

In the previous section we have looked at diffusion and advection separately. The hydrodynamic dispersion process of tracer particles or solutes inside a isotropic and homogeneous porous medium is typically described by an equation that combines both of these aspects, namely the advection-diffusion equation (ADE):

$$\frac{\partial C(\boldsymbol{r},t)}{\partial t} + \bar{\boldsymbol{v}}\nabla C(\boldsymbol{r},t) = D_L \frac{\partial^2 C(\boldsymbol{r},t)}{\partial x^2} + D_T \nabla_T^2 C(\boldsymbol{r},t). \tag{3.14}$$

The only difference compared to the diffusion equation, besides the addition of the transport term $\bar{\boldsymbol{v}}\nabla C(\boldsymbol{r},t)$, is that the diffusion term has been split up into two terms with two dispersion coefficients. The idea to model the dispersion as an anisotropic diffusional spreading is motivated by experimental and theoretical results [85], which showed that the longitudinal dispersion coefficient D_L normally is larger than the transversal dispersion coefficient D_T. The average fluid velocity is $\bar{\boldsymbol{v}}$[18] and ∇_T is the Laplacian in the direction transversal to the average fluid velocity. The meaning of the equation should be clear with the explanations that were given in the last paragraph. While particles that are released at some point in the medium flow downstream in a porous medium, the width of their distribution spreads longitudinally, i.e., in average fluid direction, and in the transversal direction. The width of the distribution will increase as the square root of time in both directions, just as it does in the case of normal molecular diffusion. Thus, the assumption of the ADE is that all the complexities of the inhomogeneous flow field in the porous medium together with the effect of molecular diffusion can be captured by just three parameters, D_L, D_T, and $\bar{\boldsymbol{v}}$, which can be an appropriate assumption for some natural media, but certainly not for all. In case of a medium of volume that is smaller than its correlation volume, the ADE will not be applicable, as the assumption that strong local variations in the velocity field will be averaged out during the whole

[17] We omitted the index, because the relevant coefficient could be molecular diffusivity, some effective diffusivity or one of the dispersion coefficients.

[18] For a porous medium of length L the average fluid velocity $\bar{\boldsymbol{v}}$ can be defined by $\bar{\boldsymbol{v}} = L/T$, where T is the average time it takes a particle to travel through the whole structure, i.e., the first moment of the FPTD.

passage of a particle is not fulfilled. We will also see later how the presence of large stagnant areas affects hydrodynamic dispersion.

If one starts with a sharp distribution, that is, a Dirac delta function at $\boldsymbol{r_0} = (x_0, y_0, z_0)$ and at $t_0 = 0$, one solution of (3.14) will again be a Gaussian distribution.

$$C(\boldsymbol{r}, t) = \frac{1}{(8\pi^3 D_L D_T^2 t)^{3/2}} \exp\left[-\frac{(x - x_0 - \bar{v}t)^2}{4D_L t} - \frac{(y - y_0)^2}{4D_T t} - \frac{(z - z_0)^2}{4D_T t} \right] \tag{3.15}$$

For simplicity the x axis was chosen to be in the direction of mean flow. The solution is completely analogous to the simple solution for the diffusion equation (3.11). Figure 3.3 (b) illustrates the one-dimensional time development of such a solution (solid lines). As time goes by, the concentration spreads out and moves with the average velocity $\bar{v}$. So, an observer moving with velocity $\bar{v}$ would observe normal diffusional spreading.

From equation (3.15) a FPTD for particles that start in an entrance plane at x_0 can also be calculated. The probability density that a particle which started at x_0 at $t = 0$ will cross x at t for the first time is given by:

$$p(x - x_0, t) = \frac{x - x_0}{\sqrt{4\pi D_L t^3}} \exp\left[-\frac{(x - x_0 - \bar{v}t)^2}{4D_L t} \right]. \tag{3.16}$$

If dispersion in the porous medium studied can be described by the ADE, equation (3.16) can be used to determine D_L and $\bar{\boldsymbol{v}}$.

3.3.4. Taylor dispersion

Before we move on to discuss the different dispersion regimes in porous media, we look at an instructive example for dispersion in a simple geometry. Experimentally, dispersion in a circular pipe was studied by injection of some tracer fluid more than a hundred years ago [91]. The velocity profile in a circular pipe of radius R is given by:

$$v(r) = 2\bar{v}(1 - \frac{r}{R}^2). \tag{3.17}$$

The injected tracer was found to spread out symmetrically about a plane that moves with the mean flow velocity $\bar{v}$[19]. The phenomenon was also studied theoretically [92, 93]. The interesting result was an expression for the longitudinal dispersion coefficient D_L:

$$\frac{D_L}{D_0} = 1 + \frac{R^2 \bar{v}^2}{48 D_0^2} = 1 + \frac{Pe^2}{48}. \tag{3.18}$$

D_0 is the diffusion coefficient of the tracer particles. The important point here is that the quadratic dependence of the dispersion coefficient on the mean flow velocity or the Péclet number. This relation has been shown to hold for arbitrary geometries, as long as diffusion and advection are equally strong [93].

[19] Whether the fact that in the long-time limit a tracer moves with the mean flow velocity is obvious or not has been debated. The straight answer is that by diffusion a tracer will spend an equal time span at each position, so that it will obviously move with the mean flow velocity.

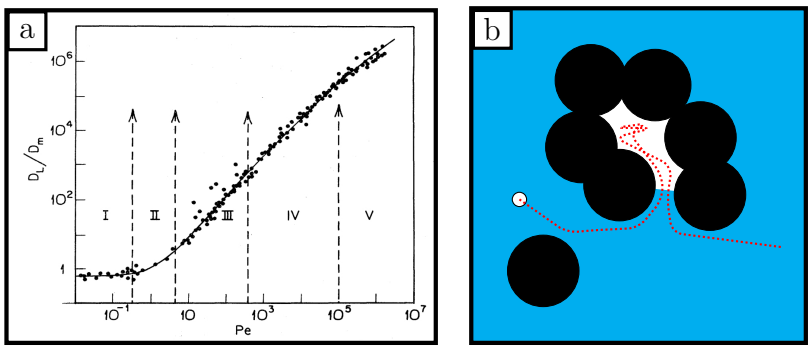

Figure 3.5.: Experimental data of measured longitudinal dispersion coefficients D_L, mainly of unconsolidated sands, versus the Péclet number Pe. The dispersion coefficients have been normalized by the molecular diffusion coefficient D_m. Five different dispersion regimes are indicated, in which D_L depends on Pe in different ways according to the dominating transport mechanisms. [85] (b) Porous medium with stagnant part (white). A particle that enters the stagnant part will not be affected by the surrounding flow and can only escape by diffusion.

3.3.5. Dispersion regimes in porous media

Dispersion in porous media has been studied experimentally as well as theoretically for many decades. Experimental data for dispersion coefficients have been obtained for unconsolidated sands and consolidated sandstones with comparable results [94].

In figure 3.5 experimental data for unconsolidated sands are collected. The dispersion coefficients have been normalized by the molecular diffusion coefficient D_m. According to the different dependences of D_L versus Pe, several dispersion regimes exist [85].

At low Péclet numbers (I), conventionally restricted to $Pe < 0.3$, diffusion dominates over the much slower transport by advection. As a result, there is also no preferred direction and dispersion becomes isotropic with dispersion coefficients that only depend on the porosity of the porous medium ϕ and its formation factor F, $D_L = D_T = D_m/(F\phi)$. After a transition zone (II), in which D_L increases with Pe in a complicated way, a power-law regime follows (III). In the forth regime (IV), where advection dominates and diffusion only mixes solutes at the nodes of the pore structure, $D_L \propto Pe$, i.e., we have mechanical dispersion. In the next regime (V), turbulent mixing starts to occur, which also implies that Pe is no longer the characterizing number.

There is also a sixth regime, the holdup regime, in which particles can get trapped in stagnant parts from where they can only escape by diffusion. This can lead to complicated FPTD with long-time tails, which cannot be explained by the ADE. It is always important to know whether the ADE is a good model for the porous medium studied. If deviations occur, e.g., formation of long-time tails, the cause must be found.

3.3.6. Deviations from the advection-diffusion equation

The hallmark of the ADE is scale-independence. In contrast, laboratory [95, 96] and field-scale experiments [97, 98] as well as simulations [99] have shown that in many cases

dispersion coefficients depend on the length and time scale of the measurement, leading to so-called anomalous transport. Therefore, anomalous transport actually is the more generic case and, thus, the ADE cannot be expected to predict dispersion in natural porous media. The complex geometry of porous media can give rise to a mixture of principal pathways, along which particles are transported by advection, and stagnant parts, wherein particles can only move slowly by diffusion (see figure 3.5). As a result one has two different time scales, one for advective and another for diffusive transport.

Due to the mentioned intricacies of porous media the ADE does not reproduce the early breakthrough and, more importantly, the long-time tails in measured and simulated FPTDs. To account for these features more advanced models have been developed. These models [100, 101, 102] use a modified form of the ADE which attributes the long-time tails to particles trapped in stagnant parts and introduces a mass transfer coefficient describing the exchange of particles between stagnant and flowing zones. Although this model yielded accurate fits to measured data [103, 49, 100, 104], the complex structure of porous media cannot be described by this simple model. Moreover, no proof for the existence of stagnant parts was given [100] and the occurence of long-time tails was alternatively explained by finite-size effects [104] or flow field heterogeneity [49, 103].

We will discuss the influence of the nonhomogeneous flow field and diffusion in stagnant parts on the FPTD in detail in chapter 7.

There are many other very interesting phenomena, which would also fit well into this chapter, but at some point we have to conclude. Yet, some aspects will be discussed at the appropriate time. The voracious reader might find consolation studying the established literature [61, 65, 105, 62, 106, 107].

4. Experimental details

In the last two chapters we discussed the basic quantities which can be used to describe a pore space and showed several examples of porous media as well as the fundamental equations and processes that govern the flow and transport inside such media with main focus on permeability and hydrodynamic dispersion. In this chapter the experimental technique for the generation of the artificial porous media, which will be used throughout this work, as well as the experimental setup will be presented. The main advantage of these artificially generated structures is that the morphology and porosity is well-defined and known so that their influence on flow and transport properties can be properly investigated, which is the main objective of this work. As a probe for the flowing fluid we will use a colloidal suspension of micron-sized particles to obtain individual trajectories by well-established video microscopy, which will be covered in the next chapter.

4.1. Sample preparation

Several methods for the fabrication of microstructures like photolithography or embossing, which is commercially used on a large scale to produce compact disks, exist [108]. For the structures used in this work a process named soft lithography will be used to generate structures of well-defined morphology.

4.1.1. Soft lithography

Soft lithography owes its name to the softness of the used polymer, polydimethylsiloxane (PDMS). The procedure to generate a sample by soft lithography consists of several simple steps [109, 108]. A short overview of the whole procedure is given in figure 4.1. First, a silicon wafer, (a), is coated with a photoresist. Next, a photomask, (b), containing the negative of the wanted structure is placed right on top of the coated silicon wafer and is illuminated by UV light. The UV light is transmitted through the transparent areas of the photomask and triggers a chemical reaction in the photoresist directly below, which makes the photoresist less soluble for the developer. The areas that have not been exposed to UV light are now, (c), removed by a developer, so that only the exposed areas remain. This is now the negative of the wanted structure. Finally, a soft polymer, which can flow at room temperature and, thus, take the shape of the remaining photoresist, (d), is poured on the wafer, and after it has cured, (e), can be peeled of and used to generate a microfluidic sample like the one shown in (f). In the following paragraphs more details for each step and about the used materials will be given and possible problems and limitations of the method will be discussed.

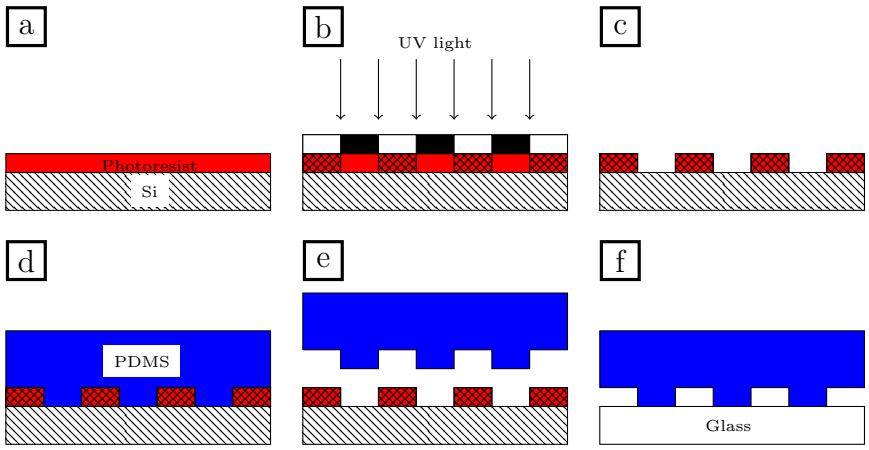

Figure 4.1.: Principal procedure for structure fabrication by soft lithography. (a) A Si wafer is coated with a photoresist. (b) A photomask that has transparent and non-transparent areas is placed on top and illuminated by UV light. (c) After developing only the exposed areas of the photoresist remain. (d) PDMS is cast on top. (e) After curing of the PDMS the PDMS can be peeled off and (f) can be used to build a microfluidic sample.

Coat

The preparation of a microfluidic sample starts with a clean silicon wafer[1]. Silicon is used because it is chemically and thermally stable. The wafer is placed on a spin-coater and 5 ml of negative photoresist[2] of a specific viscosity is spread on its surface. Next, the wafer is rotated on the spin coater in a two-step process: In the first step it is rotated at 500 rpm for 8 seconds with an acceleration of 100 rpm/s and in the second step it is rotated at 900 rpm for another 30 seconds with an acceleration of 300 rpm/s. Rotating the wafer removes excess photoresist and results in a photoresist layer of homogeneous height. The height of the layer depends on the viscosity of the photoresist and on the rotational speed. For the SU-8 2005 photoresist, which was used for most of our samples, the resulting height was about 6.5 μm. The height of the structure, which is the end product of the whole fabrication process, is a crucial parameter. Its role will be discussed in section 5.3.

After the coating is done, a soft-bake step follows during which the solvent in the photoresist vaporizes and, thereby, the photoresist layer hardens. The coated wafer is placed on a hotplate at room temperature. The hotplate is slowly heated to 97 °C over 29 minutes. After that time the heating is turned off and the wafer, still resting on the hotplate, is allowed to cool down over half an hour to about 40 °C. This is a deviation

[1] We used silicon wafers manufactured by Si-Mat in Kaufering that have a diameter of 100 mm and a thickness of 525 μm.

[2] In a negative photoresist the volume that is exposed to UV light becomes less soluble by a developer, whereas it becomes more soluble for a positive photoresist. Different negative photoresists were employed. Depending on the desired height of the structure SU-8 2002, SU-8 2005, SU-8 2007 or SU-8 2010, all products of MicroChem, was put to use.

from the standard procedure for the soft-bake step[3], as recommended in the processing guidelines, but it has produced good and reliable results.

Exposure

Since the objective of the fabrication process is a microfluidic sample with a well-defined porous structure, a photomask[4] made of quartz glass and chromium, which is composed of the wanted structures is needed. As already explained in section 2.4, pictures of the Boolean models that were used as structures were generated by a MATLAB program. These pictures together with an AutoCAD layout of the photomask were sent to the photomask manufacturer, which used electron-beam lithography to transfer the structures to the photomask. The masks were fabricated with an accuracy of $\pm 0.2\,\mu m$ and a minimum feature size of $2\,\mu m$. The shiny parts of the mask are covered by a layer of chromium. While quartz glass is transparent to UV light, chromium is opaque, so that only the parts that are not covered by chromium will transmit UV light and lead to a chemical reaction of the photoresist directly below, whereby the structure of the mask is transferred to the photoresist. One of the several photomasks that were used to produce the structures discussed in this work is shown in figure 4.2 (a). It contains 60 different structures (Boolean models). Every structure has two empty reference channels next to it. These are important for the calibration of the measured particle velocities, as we will discuss in section 5.3.

The actual exposure process is performed by putting the photomask directly on top of the coated silicon wafer. It is important to minimize the distance between photomask and photoresist layer to ensure that the structure on the mask is transferred to the photoresist as precisely as possible. Therefore, after unwanted areas of the mask have been covered by thick black paper to block the UV light, small weights are placed on top of the photomask. Next, a UV light source[5] is used to homogeneously expose the transparent part of the photomask with parallel light. The UV light leads to the activation of a photoacid generator[6]. The exposure time depends on the thickness of the photoresist layer. For our structures, exposure times were in the range of $20 - 40\,s$. The right exposure time depends on the size of the individual features of a structure. For structures with very low porosities, i.e., a large number of obstacles and, consequently few and thin paths for the fluid, the exposure time must not be too high, because such thin paths might just disappear as the individual obstacles grow together, due to diffraction effects, by exposing for too long. The same problems can also occur for structures with the opposite polarity when the exposure time is too low. After the exposure, the afore-described soft-baking step is repeated. During the heating the molecular chains at the exposed areas cross-link, which solidifies the material in these areas and makes it less soluble by the developer.

[3]The standard recommendation is to heat the wafer to 95 °C for about 2 minutes.
[4]The photomasks were manufactured by Compugraphics Jena GmbH.
[5]Dymax Blue Wave 50, $3W/cm^2$ around $\lambda = 365\,nm$.
[6]In the case of SU-8 this photoacid generator is a triarylsulfonium salt.

Development

Before proceeding, care must be taken that the wafer has cooled down to about room temperature. So, it is a good idea to leave it, e.g., in a petri dish for several minutes. Developer[7] is carefully poured on the wafer and dried with pressurized nitrogen after about 10 s. During this first rinse most of the unexposed photoresist should be washed away and only the exposed parts of the photoresist should remain. If there are still traces of photoresist on the rest of the wafer, some more developer should be used and removed again after about 10 s by pressurized nitrogen. Alternatively, the whole wafer can be put in a developer bath for the same time. In any case, developing for too long can damage the structure or even remove it completely from the wafer. If the structure is very fine and individual structure features are separated, the developer should be removed more quickly. If, on the other hand, the structure is very dense, the developer cannot easily reach every little part of the structure and, thus, such a sample must be given more time with the developer. These are just general recommendation. The tricky part is to find the right combination of exposure time and development time for every sample. For most samples, following a standard procedure that has worked for another sample will also give satisfactory results. When development is completed, a hard bake, during which the wafer is placed on the hotplate and heated slowly to 210 °C over 18 minutes, follows. This final step anneals surface cracks in the photoresist and renders the structure mechanically and chemically stable. We have reached figure 4.1 (c), i.e., the photolithographic part of the sample preparation is accomplished. The resulting structure can now be used as a master negative structure for the following replica molding. The only thing we add to the structures on the wafer are two reservoirs made of an epoxy glue[8] to allow an easier sample preparation and injection of the colloidal suspensions. An example of structures on a silicon wafer that were obtained by the steps described in the last paragraphs is shown in figure 4.2 (b). The upper two structures have already been used to build a microfluidic sample, the lower two structures are still covered by PDMS.

Replica molding

In principle, it is also possible to use the photolithographic process discussed so far to transfer a structure from a photomask directly onto, e.g., a glass slide. This glass slide containing the structure can then be covered and sealed with another glass slide on top and used as a microfluidic sample. This technique is necessary if one wants to use solvents that are not chemically compatible with the soft polymer used, but it has the disadvantage that it is hard to seal the sample and also requires a full photolithographic process for each sample.

In our studies we use the silicon wafer with the porous structures as a negative master to generate a microfluidic sample by replica molding.

[7] mr-Dev 600 from micro resist technology GmbH

[8] We used a 1:1 mixture of “5 Min. Epoxy Harz” and “5 Min. Epoxy Härter” by R+G Faserverbundwerkstoffe GmbH

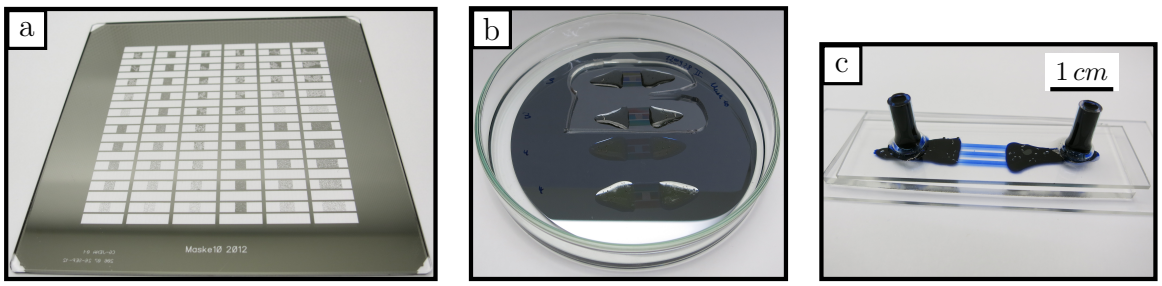

Figure 4.2.: (a) Photomask containing 60 different structures with empty reference channels. (b) Petri dish with porous structures, two of them are still covered by PDMS. Right and left of the structures and reference channels reservoirs were added by epoxy glue, which make it easier to prepare the samples and connect them to the tubes. (c) A microfluidic sample filled with dyed water.

A mixture of 10 parts (by weight) of silicon oil and 1 part of a curing agent[9] is put in a small jar and is mixed by thorough stirring with a stirring rod. If the wafer is used for the first time, the total weight of the mixture should be about 20 g[10]. The silicon wafer is placed in a Petri dish (see figure 4.1 (b)) and the mixture is poured on the wafer. There will be a large number of air bubbles in the mixture as a result of the stirring. These can simply be removed by leaving the Petri dish alone for about half an hour. The air bubbles will rise to the surface of the PDMS, where they will pop and disappear. It is obviously necessary to cover the sample during this time to avoid impurification by dust and other dirt. When the air bubbles have disappeared, the Petri dish is put in an oven at 60 °C for four hours. The wafer should be level to avoid variations in the height of the PDMS. During this time the mixture polymerizes to PDMS, i.e., the liquid mixture becomes an elastic material that can no longer flow. Temperatures above 60 °C must be avoided, because the epoxy glue is not stable above this temperature and starts to outgas.

When the PDMS has cured, two holes are punched into the reservoirs, which have been added to the structures on the wafer by the epoxy glue. These holes will serve as in- and outlet for the fluid into the reservoirs. Next, a whole PDMS structure can simply be cut out by a cutter and lifted off the wafer for further processing. Cross sections of the PDMS channels, like the one shown in figure 4.3 (a), can also be used to determine the height of the channels by optical microscopy. Such thin slices of the PDMS can be fabricated by carefully chopping the PDMS with a cutter. Since the channel is not totally flat and might also have been damaged during the preparation of the thin slices, the heights might deviate a little at different positions along the channel, so that it is advisable to measure the heights at different positions.

[9] Sylgard 184 silicone elastomer kit by Dow Corning.

[10] The wafer can be used many times in the same way. Once all the available samples on the wafer have been used, the rest of the PDMS can be cut out along the rim of the wafer with a cutter and removed. Then, one can again pour a mixture of silicon oil and curing agent on it. This time only about 15 g should be required.

[11] Credits for the SEM images belong to the Institut für Plasmaforschung. Inexcusably, I forgot the

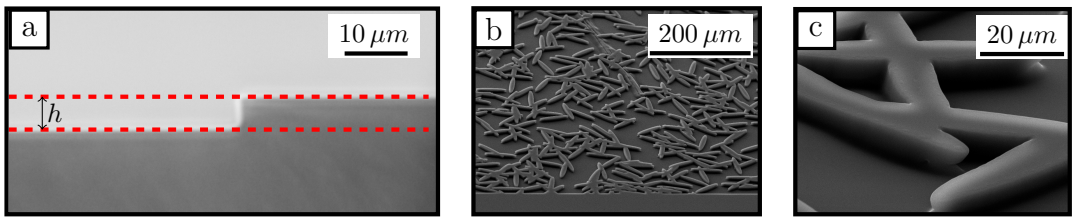

Figure 4.3.: (a) A cross-section view of a PDMS channel captured by a light microscope, which can be used to determine the height of the channel. (b) and (c) show scanning electron microscope images of a tilted PDMS structure made of randomly placed and oriented ellipses at different magnifications[11].

Preparation of the microfluidic sample

To build a microfluidic sample with the PDMS structures on the wafer, we first clean a plain microscope slide and a cover glass with two glass capillaries glued to it (see figure 4.2 (c)) with acetone and lens cleaning paper to make sure that there is no dust on the glass. These two glass parts are now put in a plasma cleaner[12]. The plasma chamber is initially evacuated and consequently filled with oxygen at a system pressure of about $0.8\,mbar$. For oxygen plasma modification of the glass parts a RF plasma power of $40\,W$ and a treatment time of $100\,s$ was used. Next, the PDMS structure is cut out, peeled off the wafer and placed (structure pointing upwards) into the plasma chamber. Again, the chamber is evacuated and filled with oxygen until the system pressure is stable at $0.8\,mbar$. The RF power is lowered to $20\,W$ for about $20\,s$[13]. During the plasma modification process, hydroxyl groups are formed on the glass surface and silanol groups are formed on the surface of the PDMS. The oxygen plasma treatment also renders the PDMS surface hydrophilic, which simplifies the injection of an aqueous colloidal suspension or dyed water. When the PDMS surface is brought into contact with the glass surface, strong covalent bonds are formed between the two surfaces. The PDMS, with the structure pointing down, is put on the microscope slide. It might take about a minute until the PDMS has bonded to the glass[14]. Next, a colloidal suspension or a dye is injected into the in- and outlet in the PDMS[15]. After that the cover glass is carefully placed on top of the PDMS to make sure that the two capillaries are connected to the in- and outlet of the PDMS. If everything is fine, the PDMS cannot be removed from the glass after the initial contact and the sample should be watertight. A microfluidic sample that has been filled with dyed water is shown in figure 4.2 (c).

name of the charming lady who operated the SEM.

[12]Zepto by Diener electronic GmbH.

[13]Measurements of contact angles of water on PDMS have been performed by Wilhelm Kiefer to make sure that the used parameters yield the best results.

[14]Experience with many samples indicates that the faster the bonding the better the sample, in terms of, e.g., particle sticking, will be.

[15]Christian Scholz found out that it is advisable to inject the suspension into in- and outlet at the same time to diminish the likelihood of a collapse of the channel due to capillary forces. By injecting at the same time, an air cushion is formed which counteracts capillary forces.

Unfortunately, this last step of the sample preparation shows a huge variation in outcomes. Samples which have been prepared, at least from the experimenter's point of view, under identical conditions, will sometimes work perfectly and at other times be totally unusable. A few points should be minded to increase the sample yield or leastwise save some time. During the whole process neither the glass surface or any of the PDMS surfaces, with exception of the rims, should be touched. Any impurity on the surface can lead to leakage or incomplete bonding of the surfaces which can easily make the sample useless. It is also recommended to have a very quick look into the structure (any microscope will suffice) after the suspension has been injected. When a lot of particles are sticking or some part of the structure has collapsed, the sample is also useless for most purposes. This will save time and also avoid wasting precious cover glasses, which have to be custom-made. Caution is also needed when the suspension is injected into the in- and outlet of the PDMS. If too much suspension is injected it will also wet the PDMS surface which will inhibit bonding to the cover glass.

A sample which has been prepared in the way described above and is functional, i.e., a large enough number of particles are flowing through the structure and no structural defects, leaks etc. are visible, can now be connected by two tubes to the fluid reservoirs and put into the experimental setup.

4.2. Experimental setup

The experimental setup is shown in figure 4.4. It consists of a conventional inverted microscope system with an additional UV light source to allow the use of fluorescent particles[16]. Depending on the requirements of the measurements or the spatial resolution, different magnifications can be used. At the lowest magnification, which has been used to capture the velocity fields that were used in chapter 7, the field of view has a size of about $4 \times 3\,mm$. To enable a detailed analysis of the particle trajectories inside the studied porous media, a high spatial as well as a sufficient temporal resolution is needed. Therefore, a high speed recording system, which can capture videos with a frame rate of up to $380\,fps$ at a resolution of $2240 \times 1724\,px$, was used[17]. At lower resolutions higher frame rates can be achieved, if needed.

For the measurements of chapter 7, the whole flow field of a porous structure of size $3860 \times 2975\,\mu m$ had to be determined using particles with a diameter of $1\,\mu m$. Since it is practically impossible to see such small particles at the required small magnification under normal light, fluorescent particles were used. The big advantage of the used fluorescent particles is that the wavelengths at which the excitation and emission spectra have their maxima differ enough to filter out just the light that is emitted by the particles.

[16]The used microscope is a Nikon Eclipse Ti with UV light source Nikon Intensilight C-HGFIE. As fluorescent particles, FluoSpheres yellow-green from Invitrogen were used.

[17]The high-speed recording system including the software is a product of GSVitec GmbH. The used camera is a Vosskühler CMC-4000. In addition, we used another system from Mikrotron with an MC 1362, which allows $500\,fps$ at $1280 \times 1024\,px$.

Using the appropriate filter[18] will allow only the light that is emitted by the small particles to reach the camera and, thus, enable an accurate detection of the particle position. The requirements for accurate particle tracking velocimetry will be covered in the next chapter.

The flow rate or the pressure gradient along the sample is controlled by the water levels in two syringes that are connected by Tygon tubes to the small capillaries on the cover glass of the sample. The tubes and the capillaries must be carefully checked for the presence of any air bubbles, which would disturb the water flow and result in unpredictable deviations in the applied pressure. The larger the difference between the water levels, the higher the pressure and, consequently, the flow rate will be. For most of our measurements, the pressure should remain constant over extended periods of time. So, the diameter of the syringes should be so large that the change in water level due the fluid flow through the sample is negligible. We will discuss these issues in the next chapter.

There is one more important thing that can help avoid a lot of potential trouble for the experimentalist. It is a very good idea to position the syringes that serve as pressure reservoirs below the level of the sample, because sometimes the tubes slip off the capillaries of the cover glass or are not completely watertight. If the syringes are below the sample, the water cannot flow into the microscope and damage it.

4.3. Determination of pore structure

One of the main objectives of this thesis is the investigation of the relation between structural and transport parameters. Therefore, it is obviously necessary to get the most accurate information about the pore structure of the investigated samples. The sample production process consists of three steps: exposure, development and replica molding. During each of these steps, inevitably, inaccuracies occur so that in the end the PDMS structure that is used for the measurements is not identical to the structure on the photomask which was exposed onto the silicon wafer. In order to get a precise picture of the PDMS structure, the investigated structure has to be imaged directly. The contrast between the solid phase and the void space of the samples was increased by injection of dyed water[19] into the sample. The dyed water flows into all of the accessible pore space and gives microscope images that are rich in contrast. One example of such a picture is shown in figure 4.5 (a). The bright, almost white, parts correspond to the solid phase and the dark areas are the void space that is filled with the dyed water. Such a picture, of course, gives a useful qualitative impression to the eye, but to get quantitatively usable information solid and void space must be clearly distinguished. Thus, a brightness threshold is applied, which results in a binary image of the structure, as shown in figure 4.5 (b), where the void phase is now white and the solid phase is black. There is some ambiguity what exactly the threshold should be, but for an homogeneously illuminated microscope picture the brightness histogram will show two well-separated

[18] B-2E (FITC) filter by Nikon.

[19] A mixture of water and methylenblue by Alfa Aesar.

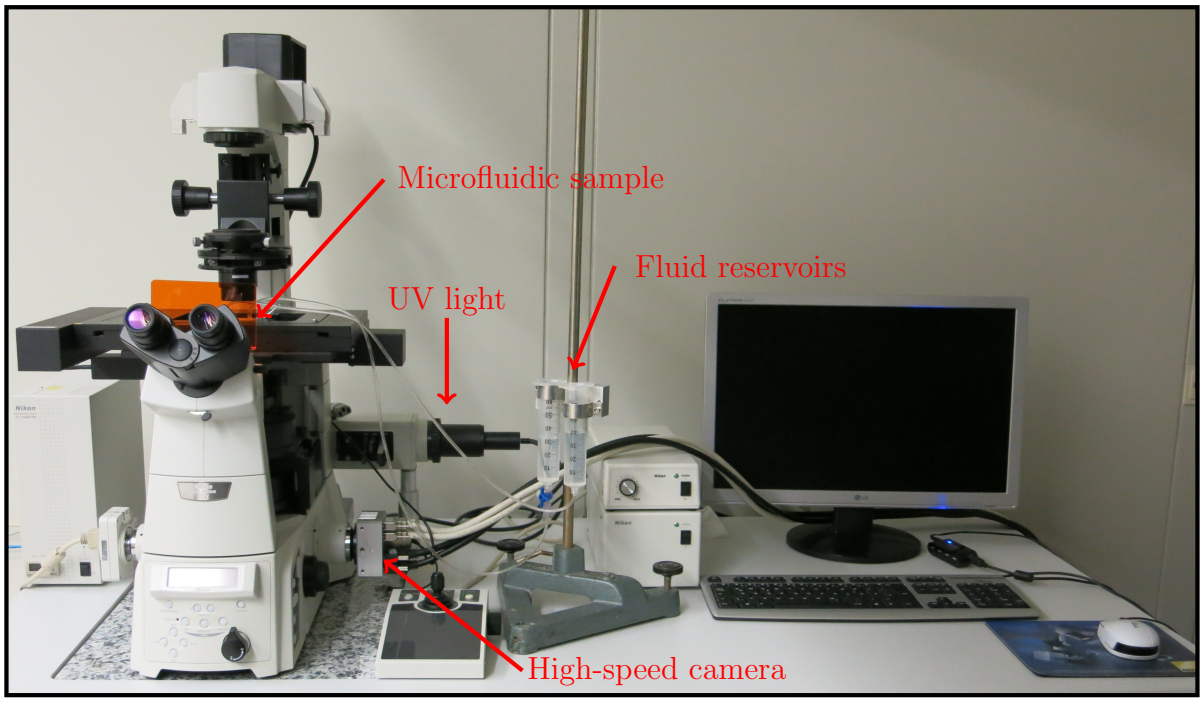

Figure 4.4.: Experimental setup: The microfluidic sample rests on the sample holder of a commercial microscope. For pressure control, two fluid reservoirs (syringes) are connected to the sample. Videos of flowing particles are captured by a high-speed recording system. A UV light source allows the use of fluorescent particles.

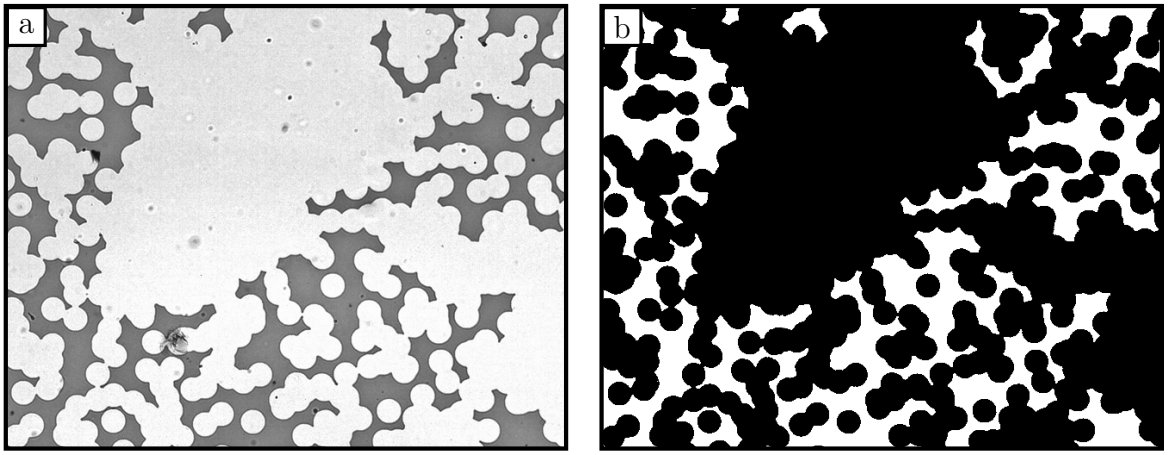

Figure 4.5.: (a) Light microscope image of a porous sample that has been saturated with dyed water to give strong contrast between porous matrix (bright) and void space (dark). (b) After application of a brightness threshold a binary image results. The effect of dirt in the sample has been corrected manually to make sure that the binary image gives an accurate description of the pore geometry.

relatively sharp maxima. The error resulting from this ambiguity, when, e.g., calculating the porosity, is small. More important for the topological characterization of the sample are the connectivity measures like the Euler characteristic. These can be very sensitive to small changes in the structure. If, for example, some small void paths that are visible on the photomask disappear during the lithographic process, the whole connectivity and, therefore, the transport parameters of the sample will be different from that of the structure on the photomask. The good news is that since the dyed water will flow into every part of the accessible pore space it can be unambiguously checked whether the connectivity of the sample and the structure on the mask is identical. In most cases the topological parameters of the sample and the structure on the mask are in agreement. The structures very close to the percolation threshold are more sensitive to small changes in the structure, because they have a lot of small features which could be lost during the lithographic process. So, these structures should be carefully checked for deviations from the corresponding structures on the mask.

Further details about the used materials, like colloidal suspension, will be given when the respective measurements are discussed in the next two chapters.

5. Measurement of flow properties in porous structures

In this chapter particle tracking velocimetry (PTV), which enables us to visualize the flow field with the help of small tracer particles, is explained step by step. The complexities arising from the fact that the tracers are of finite size and the related problems with the calibration of velocity measurements are discussed next. Two methods to measure the fluid velocity in the porous samples, and hence the permeability, are introduced: The constant-head method uses empty reference channels with known permeability in addition to the channel that contains the structure to calibrate the measurement. The falling-head method only uses the proportionality between mean particle velocity and applied pressure and makes use of the exponential decay of the applied pressure that results from the fluid flow through the structure to determine its permeability. Both methods have advantages and disadvantages which will be explained.

5.1. Particle tracking velocimetry

When a fluid is flowing through a structure, the flow field cannot be directly seen, as the individual fluid molecules are not visible. One can, for example, only tell that a river is flowing, because some features that can be distinguished from the fluid, like dirt particles, foam, air bubbles or a swimming piece of wood, are advected by the fluid. Thus, if the water in the river was crystal clear without any of the above-mentioned features, it would be necessary to introduce some visible objects to investigate the flow of the river. The fluid in the microfluidic samples used in this work is "crystal clear". Consequently, the injection of small tracer particles that can be followed as they are advected through the sample is obligatory.

In this work we used aqueous suspensions of small tracer particles with a diameter between $1\,\mu m$ and $5.2\,\mu m$ to perform particle tracking velocimetry [110, 111, 112, 113]. In short, the objective of PTV is the precise quantitative measurement of a fluid velocity field of an extended volume or area by recording videos of flowing particles with the help of conventional video microscopy and a consequent reconstruction of individual particle trajectories that allow for a calculation of the mean particle velocity of the whole field of view by averaging over many particle trajectories. The resulting particle velocity field can be used to get information about the fluid velocity field.

First of all, we have to make clear what is meant by fluid velocity at a specific point in space, e.g., inside a porous sample. This will also automatically illustrate the challenges that PTV poses. Certainly, the fluid velocity we are talking about is not the velocity

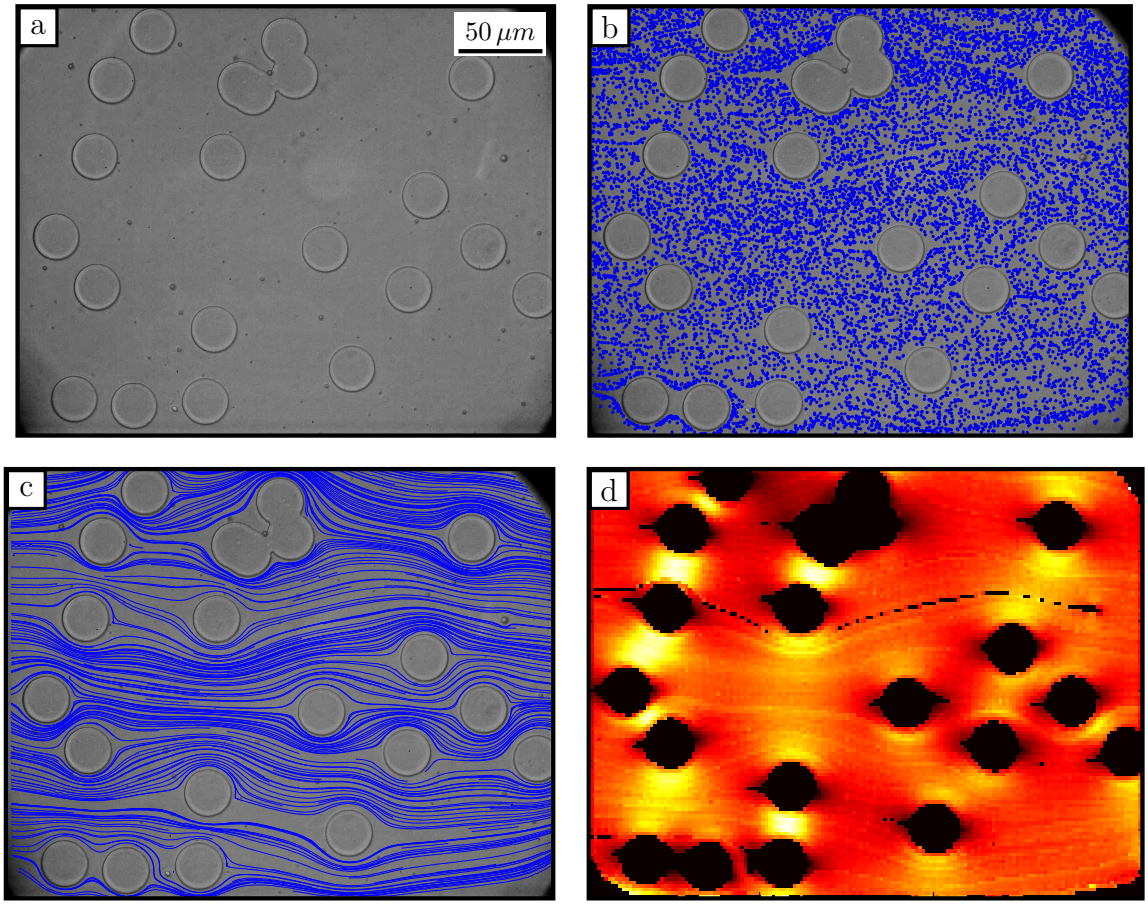

Figure 5.1.: Required steps for particle tracking velocimetry: (a) A video of small particle of different diameters travelling through a ROMC structure is recorded. (b) Image by image the individual particle coordinates are tracked. (c) The coordinates are connected to reconstruct the trajectories of the particles. (d) The field of view is divided into small cells and the mean velocity of the particles therein is calculated which gives the particle velocity field that can be related to the fluid velocity. Bright colors correspond to high velocities.

of a single water molecule as the velocity of one particle will be strongly affected by its Brownian motion and will fluctuate strongly. If we look at a large number of molecules at a certain point in space and take the average of their respective velocities, we will get a quantity that does not show any measurable variations over time, because the effect of Brownian motion will cancel out. So, by fluid velocity at a certain position we mean the average velocity of a large number of individual fluid molecules. This is also the intuitive notion one has when speaking of flow velocity and it is also the quantity that one wants to measure with the help of some tracer particles.

This task, as plain as it may sound, is far from simple, because any particle of finite size, i.e., any real object that is advected by a fluid will alter the properties of the surrounding flow field or even the fluid itself, e.g., by generation of a shear in a non-Newtonian fluid, and will not exactly follow the motion of the fluid. That means that any finite particle is a nonideal tracer. The whole concept of an ideal tracer that faithfully follows the mean flow and does not disturb the fluid is only a theoretical construct that is not reproducible in an experiment. It should also be clear that by using smaller and smaller particles, their diffusion coefficients would get larger and larger which would also make them less valuable as a probe for the flow field as one cannot measure trajectories of a very large number of such very small particles and average their properties to end up with very accurate data. The use of very small particles is also only a hypothetical thought for another reason, because in an actual experiment the microscope has a limited resolution and, thus, the used tracer particles must have a certain minimum size to be visible. Such finite-sized particles, as stated above, cannot probe the fluid's properties at their center of mass, as they have to average over the flow field in a complicated and not fully understood way, whereby they also disturb the surrounding fluid. In addition to the effects that are exclusively caused by their finite size, sedimentation or buoyancy due to a mass density that differs from the fluid's mass density or interactions with the porous matrix can also lead to complications. At high flow rates, i.e., high Reynolds numbers, hydrodynamic effects which cause so-called lift forces can lead to the accumulation of particles in certain regions [114, 115, 116, 61]. Whenever one is dealing with tracers, one should keep all these complications in mind and must not mistake the movement of the particles for the movement of the fluid.

Summing up, ideally particles should be significantly smaller than the smallest relevant flow field length scale, but also large enough to minimize errors due to Brownian motion for PTV to give satisfactory results with regards to information about the actual fluid flow velocity [117]. Such a compromise cannot always be realized due to experimental restrictions by the equipment or by the investigated structure, which can have extremely narrow paths that would call for even smaller particles, which may not be traceable. For the permeability measurements of the structures in this work we used particles that were comparable in size to the height of the sample, that is, the relevant length scale of the sample. In section 5.3 we will explain how the two methods that were employed to measure the permeabilities work around the problem of finite-sized tracers and determine the permeability independently of the size of the used tracers.

The principal steps for PTV are shown in figure 5.1. The first step is to acquire a video of the colloidal suspension flowing through a structure, as shown in (a), where a

mixture of particle of diameter $1.2, 2.4, 3.4$ and $5.2\,\mu m$ was used. Next, the coordinates of individual particles are tracked (b) and their trajectories are reconstructed (c). In (b) and (c) only a small fraction of the total coordinates and trajectories are shown. From the trajectories the particle velocity field can be calculated by dividing the field of view into small cells and averaging over the velocities of the particles that pass these cells. A resulting velocity field is shown for particles with a diameter of $5.2\,\mu m$ in (d). In the following we describe each step and the occurring problems.

Video microscopy

As probes for the fluid motion we used suspensions of deionized water and different colloidal particles made of melamine or polystyrene with diameters between $1\,\mu m$ and $5.2\,\mu m$. For the measurements in chapter 7 we used fluorescent polystyrene particles with a diameter of $1\,\mu m$. The suspensions are injected into the sample to be studied and a pressure is applied. The flowing particles are recorded with the setup that has been described in the last chapter. Particles appear as dark rings or dots depending on their size, as shown in figure 5.1 (a). In the case of fluorescent particles the particles show as bright dots on a black background. A few important remarks for the experimenter: The used frame rate must be high enough so that even the particles that flow through the fastest parts of the structure, normally corresponding to small bottlenecks, can still be tracked accurately. On the other hand the frame rate should also be as low as possible to avoid having a truckload of frames that do not contain useful information. When the applied pressure is doubled, clearly, the frame rate must also be doubled, because particles at the same position will on average travel twice as far during the same time. Also make sure that the exposure time of the camera is set to a constant value (lower than fps^{-1} of the scene with the highest frame rate) so that all measurements have the same brightness and can later be tracked using the same tracking parameters.

Particle tracking

After a video of the flowing particles has been captured, the coordinates of every particle have to be determined frame by frame. For the non-fluorescent particles, which appear darker than the background, the background can be identified by choosing three frames of the video and generating a new frame by picking only the brightest of the three pixels at each point. Every frame of the video is now subtracted from this background frame so that the particles show as bright rings or dots in a grayscale image. Next, a brightness threshold is applied which gives a binary image for each frame in which the particle rings or dots show up as white regions on a black background. To get rid of the noise in the binary images, first an erosion operation is performed during which all the small isolated white pixels are removed. After that the remaining white parts are dilated to merge separated regions that belong to one particle. The dilation operation can, unfortunately, also lead to the merging of areas which belong to different particles. This can happen frequently, if the particle density is high and therefore the mean particle distance is low. Logically, the experimenter must choose the right particle

concentration to minimize this problem. The white regions are now classified according to their area. Regions in a certain area range belong to particles of a certain size. The centers of mass of the regions which fall into such a range are determined and are used as particle coordinates. The whole particle tracking process was implemented in a MATLAB program[1].

In case of the fluorescent particles the background subtraction is not needed, as the whole background apart from noise is dark and the particles appear as bright dots, which can be tracked by application of a brightness threshold.

Coordinate tracing

The tracked coordinates are now combined to generate the individual particle trajectories by a well-established tracing algorithm [118], which has been implemented in another MATLAB program[2]. In the program several parameters can and have to be adjusted for each tracked coordinate file to end up with accurate trajectories of the particles. The most important parameters are the number of frames a fitting next coordinate for a particle is searched, i.e., how long a particle is kept in memory, and the maximum distance a particle can travel during this interval. Keeping "lost" particles in memory is necessary since not every particle is tracked in every frame during particle tracking due to noise. The restriction of the distance a particle can travel during this interval must be conducted with caution. If the value is too small, trajectories of particles in fast regions will be disconnected. So, this restriction sets the lower limit. On the other hand, the value must not be too high, because this would lead to false connections between trajectories that do not belong to the same particle. Choosing a value that is too high will also make the tracing process very slow, as the program has to check more and more potentially fitting coordinates. Just like for the particle tracking a relatively low particle density will make the tracing process a lot easier, more reliable and will require less computational effort, i.e., less main memory and time. Because, if the particle density is too high, the tracing algorithm will not be able to decide which coordinate belongs to which particle as they are so close that several choices fulfill the criteria that the algorithm checks. The parameters must be optimized by trial and error. The arising trajectories must be carefully checked each time to guarantee accurate results.

Calculation of particle velocity field

The calculation of the particle velocity field or just a mean particle velocity in a sample seems to be more straightforward than it actually is. The problem is the weighting of the velocities of different trajectories that pass the small cells, that the structure is subdivided into, to calculate the velocity field. The first and simplest possibility is to just go through each trajectory frame by frame and calculate the velocity during each time step by subtracting the coordinate of that frame from the coordinate of the frame before and dividing it by the time interval between the two frames. This can be done

[1] Kudos and thanks to Hans-Jürgen Kümmerer for writing and constantly improving the code.
[2] In this case Christian Scholz was responsible for the programming.

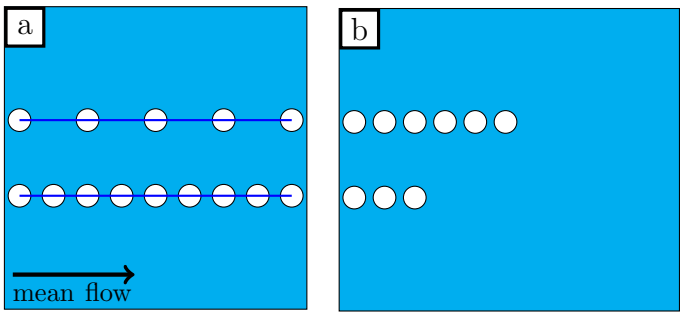

Figure 5.2.: (a) Exemplary snapshots of two particles flowing through a cell in the field of view. The slower particle (lower one) will give more data points than the fast one at constant frame rate, because it stays in the field of view for a longer time. (b) Biased-sampling problem illustrated by two lines of particles travelling with different velocities. The upper particle line travels on a streamline where the flow is twice as fast as for the lower particle line. If the particle density is homogeneous, twice as many fast particles are observed in the field of view during the same time, which will lift the average particle velocity.

for all trajectories that pass a certain part of the structure. When all these velocities have been calculated, their mean value can be used as mean velocity in that part.

There is principally nothing wrong about this method, but it suffers from a grave disadvantage. The problem can be easily understood by looking at figure 5.2 (a). There, consequent snapshots of particles travelling with different velocities are shown. Let us assume that the upper particle travels with $2\,\mu m/s$ and the lower one with $1\,\mu m/s$. So, it seems clear that the average particle velocity should be $1.5\,\mu m/s$. This, however, is not the case, if the method described above is used. If the videos of the particles are captured with the same frame rate, of course, the slower particle will show up in more frames, in direct proportion to its velocity. Therefore, the velocity of the slower particle will have a higher weight for the mean particle velocity. In the discussed case, the velocity of the slower particle will be weighed twice as much as the velocity of the faster one and, consequently, the mean value will work out to $1.\bar{3}\,\mu m/s$[3]. In this example, the difference is not extreme but still important. A more extreme case would be one particle travelling with $0.001\,\mu m/s$ and the other with $1\,\mu m/s$. The mean value would give $0.002\,\mu m/s$, very close to the velocity of the slow particle, as it gives a thousand times more data points, and also a huge difference to the intuitively expected value of $0.5005\,\mu m/s$. This problem is quite a real one for the experiments conducted in this work, because particle velocities can differ substantially as we will later see. Just one very slow particle can totally dominate and, thus, distort the calculated mean particle velocity. In an experiment it happens frequently that some particles are moving very slowly, because they are, probably due to imperfections in their surface functionalization, just creeping at the bottom of a microfluidic sample. Such particles would certainly result in a vast underestimation of the mean particle velocity. Clearly, another more robust approach to the mean particle velocity is needed.

[3] $(1 \cdot 2\,\mu m/s + 2 \cdot 1\,\mu m/s)/3 = 1.\bar{3}\,\mu m/s$

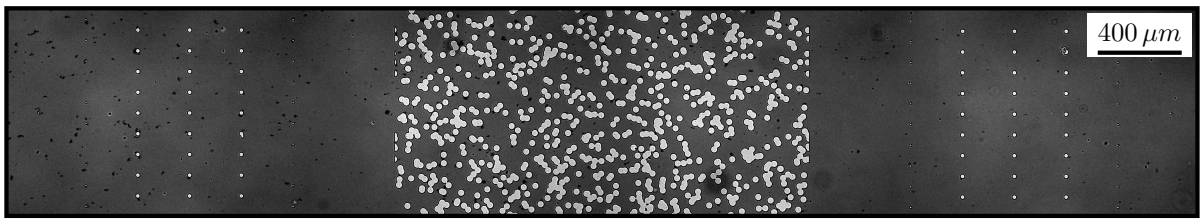

Figure 5.3.: Microscope image of a typical PDMS structure that is used for permeability measurements. The sample consist of an inner part which contains the actual porous structure and two outer parts which are basically just flat empty channels, that are needed to measure the mean fluid velocity through the sample.

The solution is very simple. Throughout this work the individual velocities of different particles will be weighed by the length of their trajectories to determine the mean particle velocity $\bar{\boldsymbol{u}}$:

$$\bar{\boldsymbol{u}} = \frac{\sum_i \boldsymbol{u}_i L_i}{\sum_i L_i}, \tag{5.1}$$

where $\boldsymbol{u}_i$ is the velocity of a particle[4] and L_i the length of its trajectory. By length the distance between starting coordinate and end coordinate is meant. Following this formula for $\bar{\boldsymbol{u}}$ will avoid the trouble of overweighting slow particles and make the calculated values more reliable.

5.2. Particle transport in porous structures

In this section the specific complications for the permeability measurements that are caused by the finite size of the used tracer particles will be discussed. In the microfluidic samples used in this work the influence of the size of the particles is substantial, since in every case they are comparable in size to the relevant fluid field length scale, i.e., the diameter of the particles is never less than 10% of either the sample height or the smallest pore throat of the sample.

A typical PDMS structure with a porous segment in the middle part surrounded by two empty outer parts that are used to determine the mean particle velocity is shown in figure 5.3. It will first be shown how the finite size of the particles affects their transport in a simple empty channel and then consider their motion in a more complicated porous structure.

5.2.1. Influence of particle size in an empty channel

Even in an empty channel where no obstacles hinder the fluid flow and where the particles are just advected along straight lines, besides some small deviations due to Brownian motion, the relation between particle velocity and fluid velocity is far from simple.

[4]It is the average velocity of the particle during the considered part of its trajectory, to be precise.

Table 5.1.: Mean particle velocity $\bar{u}$ and calculated $\tilde{u}$ for different sized polystyrene particles of diameter d and corresponding gravitational length λ within an empty channel of height $h = 6.5 \pm 0.3\mu$m and length $L = 8600 \pm 50\mu$m. The theoretical value of the mean fluid velocity for a channel of this hight at a pressure drop of $\Delta P = 479Pa$ is calculated to be $196 \pm 20\mu$m/s.

d (μm)	λ (μm)	$\bar{u}$ (μm/s)	$\tilde{u}$ (μm/s)
1.2	8.75	270.6 ± 1.4	240 ± 36
2.4	1.09	246.6 ± 3.3	224 ± 32
3.4	0.383	234.3 ± 4.6	194 ± 32
5.2	0.107	215.7 ± 3.6	176 ± 59

Assuming that the no-slip condition holds on the particle surface, it is clear that the particle-fluid interplay must be very complicated, as the particle can be viewed as a moving obstacle around which the fluid has to flow.

For the measurements of mean particle velocities an aqueous suspension[5] of four different polystyrene particles of diameters $d = 1.2, 2.4, 3.4, 5.2\,\mu m$ was injected into a microfluidic sample that consisted of an empty channel of height $h = 6.5 \pm 0.3\mu$m and length $L = 8600 \pm 50\mu$m. A pressure of $\Delta P = 479Pa$ was applied. A theoretical value for the mean fluid velocity of $196 \pm 20\mu$m/s can be calculated with Darcy's law (3.8) and the permeability of a flat channel $k = h^2/12$. The mean particle velocities for different particle diameters $\bar{u}(d)$ were determined. The results are summarized in table 5.1. The values for $\bar{u}(d)$ differ significantly and show a monotonous decrease for increasing particle diameters. This already makes it clear that our particles are far from being perfect tracers and that the average particle velocity $\bar{u}$ is, in general, different from the mean fluid velocity $\bar{v}$.

It is the interplay of several effects that leads to this deviation: First, the particles disturb the flow field and also interact hydrodynamically with the walls. The result is that the velocity of the center of the particle at a certain height does not equal the velocity of the fluid at that height. One can easily imagine a sphere in a cylindrical tube that has about the same diameter as the tube. The sphere would move considerably slower than the average fluid velocity, because of the proximity of its surface to the surface of the tube. If the no-slip condition holds for both surfaces there must be strong gradients in the space between both surfaces, i.e., high shear rates and, thus, a strong drag against the movement of the particle. A particle that is not located in the middle of a channel (see figure 5.4) will clearly also feel a torque and rotate as a consequence. The flow field around the particle cannot be symmetric if the particle is not in the center of the channel and, therefore, the velocity at the top of the particle is different from

[5] A suspension of $1\,\mu l$ of IDC 1-1200 with $d = 1.2\,\mu m$, $10\,\mu l$ of IDC 1-2400 with $d = 2.4\,\mu m$, $30\,\mu l$ of IDC 1-3500 with $d = 3.4\,\mu m$, $60\,\mu l$ of IDC 1-5000 with $d = 5.2\,\mu m$ (all products of Life Technologies) and $400\,\mu l$ of deionized water was prepared. Note that one has to take larger volumes of larger particles, because, if the content value is the same, their number density will decrease proportional to d^{-3}.

the velocity at the bottom of the particle, which will cause a torque. The velocities of different-sized particles at different positions in a flat channel have been calculated by a boundary-integral algorithm [119] and have also been investigated experimentally [120]. It was found that the average particle velocity decreases monotonously with increasing particle size, which is in agreement with our results. Second, for particles that have a different mass density than the surrounding fluid the probability to find a particle at a certain height is given by the barometric height distribution $p(z) = \exp(-\frac{mgz}{k_B T})$, where m is the volume of the particle multiplied by the difference of the mass density of the particle ($\rho_p = 1.05\, g/cm^3$) and the fluid ($\rho_f = 1.00\, g/cm^3$), k_B Boltzmann's constant, g the gravitational acceleration and T the absolute temperature [121]. A characteristic gravitational length $\lambda = \frac{k_B T}{mg}$, which gives the mean height of the particles, can be defined. Ceteris paribus, λ will be smaller for larger particles, implying that larger particles will on average be closer to the bottom of a cell than smaller ones. This, certainly, will have a big effect on the mean particle velocity obtained by using particles of different sizes[6]. Third, the limited field of view in the experiment will lead to a biased sampling of fast particles, because fast particles pass the field of view more frequently than slow particles, which will shift $\bar{u}$ to higher values. To understand this point one can imagine (also see figure 5.2 (b)) having a homogeneous particle distribution in the channel, that is, the spatial distance between particles at each height in the channel is the same and, consequently, more particles in the fast parts of the flow profile will pass by and contribute to the mean particle velocity, which will evidently lift its value. This effect persists as long as the particles do not have enough time during their passage of the field of view to diffuse across the whole velocity profile. So, basically the problem of a small field of view is that the particles will stay on the same streamline so that each particle passing through will have a different velocity. In a very large field of view all particles (averaged over their trajectories) would have the same velocity, because they could diffuse into slow and fast regions and sample the whole profile equally well.

Table 5.1 also shows calculated values for the mean particle velocity $\tilde{u}$. These values were calculated by assuming the barometric height distribution for the particles and using an interpolation of the numerical results given in [119][7]. The obtained values for $\tilde{u}$ follow the same trend for increasing particle diameter and are close to the measured values for $\bar{u}$. What catches the eye is that the calculated values are lower than the measured one for every particle size. A logical explanation for this discrepancy is given by the fact that the assumed particle distribution is definitely too simple to describe our system. For instance, both the surface of the particles and the surface of the walls of the cell are charged so that the particles are repelled from the walls which would push

[6] For very small particles the height distribution will always be homogeneous.

[7] The calculated values for the velocities $\tilde{u}$ were obtained by using the numerical values from [119] for the velocity $u_d(z)$ for particles of diameter d at height z. The barometric height distribution $p(z) = \exp(-z/\lambda)$ was multiplied by the velocity $u_d(z)$ to obtain an effective particle distribution $p_{eff}(z) = u_d(z)p(z)$ that takes biased sampling of faster particles into account as the inception rate is proportional to the particle velocity. Combining these equations, the calculated mean particle velocity is $\tilde{u}(d) = \int_{d/2}^{h-d/2} u_d(z) p_{\mathrm{eff}_d}(z) dz / \int_{d/2}^{h-d/2} p_{\mathrm{eff}_d}(z) dz$.

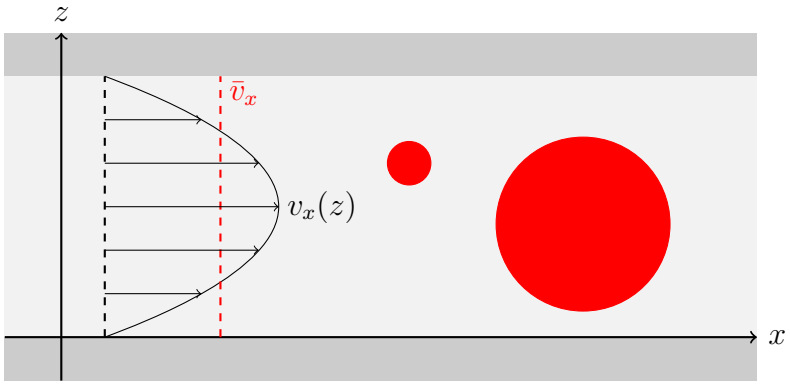

Figure 5.4.: Illustration of particles (red) of different sizes in a flat channel. If the particle mass density is higher than the fluid's, smaller particles will on average move farther away from the bottom. Smaller particles will also average over a smaller volume of the flow field and not affect the fluid's flow field as much as a larger one.

them towards the center of the channel and, thus, away from the slowly flowing parts near the channel walls.

5.2.2. Influence of particle size in a porous structure

All of the aforementioned complications, evidently, also arise in a complex porous structure, as there is still a variation in the fluid velocity from bottom to top of the cell. But due to the random porous structure the velocity field will now also be nonhomogeneous for particles that travel at the same height. The resulting motion of the particles becomes even more complex and the different particle sizes can lead to totally new effects that vastly alter their transport characteristics. Some readily understandable differences in the transport behavior of particles of small and large size can be seen in figure 5.5, where a small part of the investigated structure (the one that is also shown in figure 5.1) was magnified. (a) and (c) show trajectories of particles with a diameter of $d = 1.2\,\mu m$, and (b) and (d) of particles with $d = 5.2\,\mu m$. The trajectories in the upper row, (a) and (b), were captured at an applied pressure of $\Delta P = 479\,Pa$, whereas for the lower ones, (c) and (d), the pressure $\Delta P = 19\,Pa$ was significantly lower. At both pressures the mean direction of flow was from right to left. The obvious difference, which is caused by the simple restriction that the center of the particles cannot get closer to the obstacles than their radius, is that smaller particles sample a larger region than the large ones[8]. This volume exclusion can lead to a faster transport of large particles in a porous structure, because the large particles cannot come as close to the surface of the obstacles as the small particles and will, therefore, stay on faster streamlines [122]. The phase space for larger particles is smaller and is mainly restricted to areas of fast flow, i.e.,

[8]It is a little more complicated, because by sampling we mean that their center of mass, and not the whole particle, samples a smaller region. The phase space accessible for a particle can be obtained by eroding the pore space by a disc that has the radius of the particles.

wide pores and throats, so that it is intuitively clear that they are transported faster on average, even if the small particles might travel faster at the same spot than the large ones. Although this effect has been observed experimentally, it can, obviously, not be generally true and will depend, e.g., on the structure used as well as its height and the particles' gravitational length. In 3.3.1 we have already shown that steric repulsion can also lead to crossing of streamlines and break the time-reversibility of particle transport at low Reynolds numbers. This streamline crossing can also lead to "shadows" behind an obstacle, i.e., a certain region that a large particle will not reach and which, hence, will not be sampled in the velocity field. This shadowing becomes less and less pronounced as the Péclet number is lowered and Brownian motion can counteract and move particles into excluded regions. In (c) it is seen that the small particles diffuse very strongly and can even enter a stagnant part and diffuse around until they escape again and are advected by the fluid flow. This temporary trapping in stagnant areas has a vast effect on the particles' retention times, which will be discussed in chapter 7. For the large particles (d) the difference in our example is not that pronounced, solely the particle trajectories exhibit stronger fluctuations, since their diffusion coefficient is significantly lower, not only due to their larger size but also because of hydrodynamic interactions with the walls [105].

5.3. Permeability measurement

The last section made clear that it would be flawed to assume that the mean particle velocities measured by PTV are just equal to the mean fluid velocity, since particles of different sizes will average over different areas of the flow field and will also average in different ways. Additionally, one also has to deal with the effect of Brownian motion, which can be accounted for by averaging over many particles. The obvious problem for a permeability measurement that has to be solved is the calibration of the particle velocity, which will allow a measurement of the mean fluid velocity and, thus, the permeability of a porous sample.

Although we have just seen that even in a very simple geometry, that is to say a flat channel, with a parabolic velocity profile, the relation between mean particle velocity and mean fluid velocity is non-trivial, our experiments with particles of different sizes have revealed that there is a straightforward relationship between these two quantities. In figure 5.6 the mean particle velocities $\bar{u}$ for different particle sizes are plotted versus the applied pressure ΔP for particles that are flowing in the empty segment of the channel (circles) and inside the porous structure (squares). Fits to the data points (dashed lines) clearly show that there is a linear relation between $\bar{u}$ and ΔP, which was also shown theoretically [123]. Interestingly, this proportionality also holds inside a porous medium, but it has to be taken with more care, as this need not necessarily be the case for any kind of structure. Volume exclusion might lead to a non-linear relation between $\bar{u}$ and $\bar{v}$. Another point to keep in mind is that the average particle velocity does not necessarily have to be higher inside a porous structure, although the fluid velocity due to continuity requirements clearly has to, because, e.g., volume exclusion could also move particles

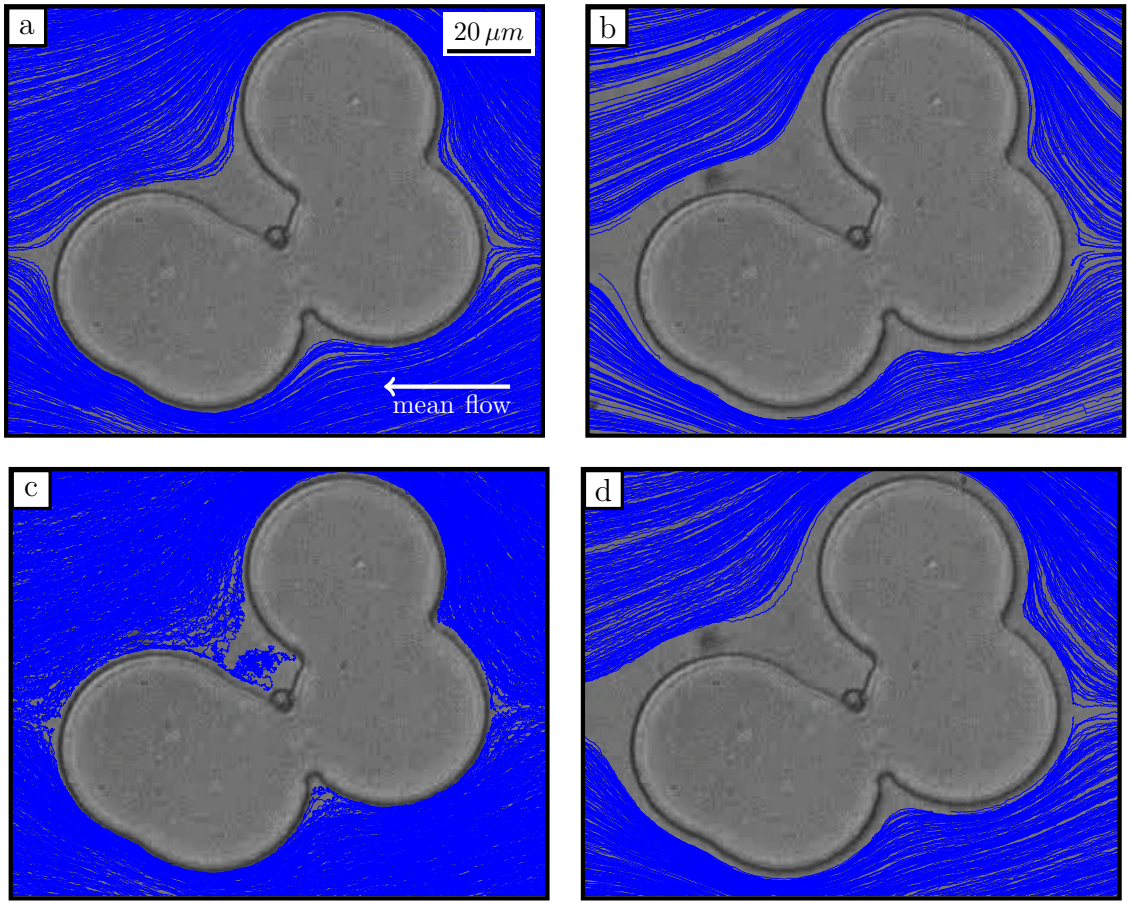

Figure 5.5.: Particle trajectories in a porous medium consisting of randomly overlapping circles for particles with $d = 1.2\,\mu m$ (a,c) and $d = 5.2\,\mu m$ (b,d) at a pressure drop of $\Delta P = 479\,Pa$ (upper row) and $\Delta P = 19\,Pa$ (lower row). Large particles are excluded from the surface of the obstacles, as their center cannot come closer than their radius. The effect of diffusion (c vs. d) is much stronger for small particles and allows them to sample stagnant parts, from which the large particles are prevented by volume exclusion, more frequently.

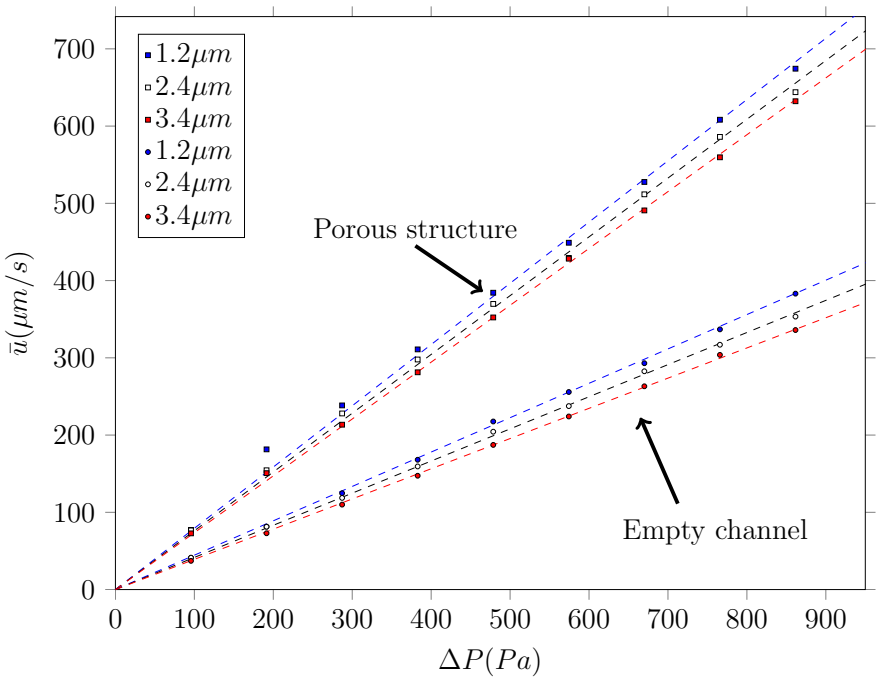

Figure 5.6.: Mean particle velocity $\bar{u}$ vs. applied pressure ΔP in an empty part (circles) and porous part (squares) for particles with diameter $d = 1.2\,\mu m$ (blue), $d = 2.4\,\mu m$ (white) and $d = 3.4\,\mu m$ (red). The dashed lines correspond to linear fits through the origin.

to slower streamlines. If we assume that Darcy's law (3.8) holds in our system, i.e., $\bar{v} \propto \Delta P$, the proportionality between between $\bar{u}$ and ΔP implies that:

$$\bar{u} = c_d \cdot \bar{v}, \tag{5.2}$$

where c_d is a constant for a given particle diameter d. Certainly, c_d will also depend on the type of particles used, because their surface properties and their mass density can differ and would, hence, give different values for c_d. Here, we restrict ourselves to one type of particle and avoid such discussions. The constant c_d can be determined by measuring $\bar{u}$ in an empty reference channel, since at a certain pressure drop ΔP the mean fluid velocity $\bar{v}$ can be calculated analytically[9]. In our experiments $\bar{u}$ was always larger than $\bar{v}$ for all used particle diameters, i.e., $c_d > 1$. This, however, is not generally valid. Just imagine a very high empty channel: all particles would, due to their small gravitational length, travel close to the bottom and, hence, would have a very low velocity. So, in every case the constant c_d has to measured carefully to prevent a misinterpretation of fluid velocities.

[9]Remember, the permeability of a flat channel is well approximated by $k = h^2/12$. Putting this value and the applied pressure ΔP into Darcy's law (3.8) gives the mean fluid velocity $\bar{v}$.

5.3.1. Constant-head method

Figure 5.7 (a) shows a schematic of the channel arrangement (see also figure 4.2 (c)) that was used to simultaneously determine the constant c_d with the help of the two empty reference channels, and to measure the permeability of a porous structure. The two empty channels have the same height[10] as the channel that contains the porous structure and serve as reference channels for the calibration of the velocity measurement. Such an arrangement of channels allows to measure the mean particle velocity of the reference channel and of the channel containing the porous structure at the same time and at the same pressure drop.

Figure 5.7 (b) is a schematic of an equivalent circuit diagram of hydrodynamic resistance, which allows a simple calculation of the permeability of the resistance of the porous structure, which is related to its permeability by simple equations explained below. The middle channel, which contains the porous structure, is a series of three hydraulic resistances and the goal of our measurements is the determination of R_{por} and thereby the permeability k_{por} of the porous structure.

A hydraulic resistance can be defined as:

$$R_{hyd} = \frac{\Delta P}{Q} = \frac{\eta L}{kA}, \tag{5.3}$$

where Darcy's law (3.8) has been used to derive the last equality. The definition here is completely analogous to Ohm's law for the electrical resistance $R_{el} = U/I$ with U the applied voltage and I the flowing current. In hydrodynamics the voltage is replaced by the applied pressure ΔP, which is the potential difference between the two water columns that are connected to the sample, just as the voltage is the difference between the two electrical potentials, and the electrical current by the hydraulic current Q, i.e., the volumetric discharge.

Calculating with the hydraulic resistances is also analogous to their electrical counterparts. For instance, the total resistance R_{tot} of the middle channel is a series circuit of three resistances, namely the two empty segments with resistances R_{in}, R_{out} and the resistance of the porous structure R_{por}:

$$R_{tot} = R_{in} + R_{por} + R_{out} \tag{5.4}$$

This simple assumption requires that the empty segments and the porous structure are well-connected, which is justified for structures with high porosities. At low porosities, however, there might only be a few entrances and exits for the fluid into the porous structure, which will also disturb the flow in the empty segments. The consequent inaccuracies of the permeability measurement can be reduced by measuring at several positions and averaging over the obtained velocities. The most accurate but impractical method for the mean velocity measurement is by determining the whole velocity field

[10] This, certainly, is not an exact statement, but the heights of the channels will not differ by much, since they are created during the same lithographic process. We have measured the height of each channel and taken deviations into account.

across a channel. In any case, due diligence is needed to avoid a false evaluation of the data.

Now, all resistances in (5.4) are replaced by (5.3):

$$\frac{\Delta P}{Q_{por}} = \frac{\eta L_{in}}{k_0 A} + \frac{\eta L_{por}}{k_{por} A} + \frac{\eta L_{out}}{k_0 A}, \tag{5.5}$$

where the left-hand side shows the pressure drop ΔP across the whole channel that contains the porous structure divided by the volumetric flow rate Q_{por} through that channel. On the right-hand side the individual resistances are expressed in terms of the lengths of the three segments and their permeabilities. L_{in} is the length of the inlet, L_{out} the length of the outlet and L_{por} the length of the porous part of the channel. The corresponding permeability for the in- and outlet is k_0, which is assumed to be the same as for the two reference channels, and k_{por} is the wanted permeability of the porous structure in the middle of the channel.

Next, (5.5) is multiplied by $k_0 A/\eta$ followed by replacing k_0 on the left-hand side with (5.3) for a reference channel[11]:

$$\frac{k_{por}}{k_0} = \frac{L_{por}}{L_{ref}\frac{Q_{ref}}{Q_{por}} - (L_{in} + L_{out})}. \tag{5.6}$$

The permeability of the porous structure normalized by the permeability of the empty channel k_{por}/k_0 depends on the ratio of the flow rates of the reference channel Q_{ref} and the channel with the porous structure Q_{por}. As elaborated before, we cannot measure the flow rates directly, but have to use the known geometry of the reference channels to determine c_d, which is related to the flow rate:

$$Q = c_d \bar{u} A \tag{5.7}$$

This can be used to replace Q_{ref} and Q_{por} in (5.6) by the respective mean particle velocities $\bar{u}_{ref}$ and $\bar{u}_{por}$:

$$\frac{k_{por}}{k_0} = \frac{L_{por}}{L_{ref}\frac{\bar{u}_{ref}}{\bar{u}_{por}} - (L_{in} + L_{out})} \tag{5.8}$$

This equation makes clear that the task of the experimenter consists in measuring the mean particle velocities $\bar{u}_{ref}$ in the reference channel and $\bar{u}_{por}$ in the empty segment of the channel containing the porous structure as well as the required lengths and the height of the reference channels, which are needed to calculate $k_0 = h^2/12$.

In the deviation of (5.8) it was assumed that all three channels have the same length and height. This is an oversimplification, as there are slight variations during the sample preparation process, which can lead to varying lengths and heights of the individual channels. So, in case of deviations the ratio of the mean particle velocities $\bar{u}_{ref}/\bar{u}_{por}$ has to be multiplied by $\frac{h_{por}^2 L_{ref}}{h_{ref}^2 (L_{in}+L_{por}+L_{out})}$.

[11] That is, $k_0 = \frac{\eta Q_{ref} L_{ref}}{A \Delta P}$.

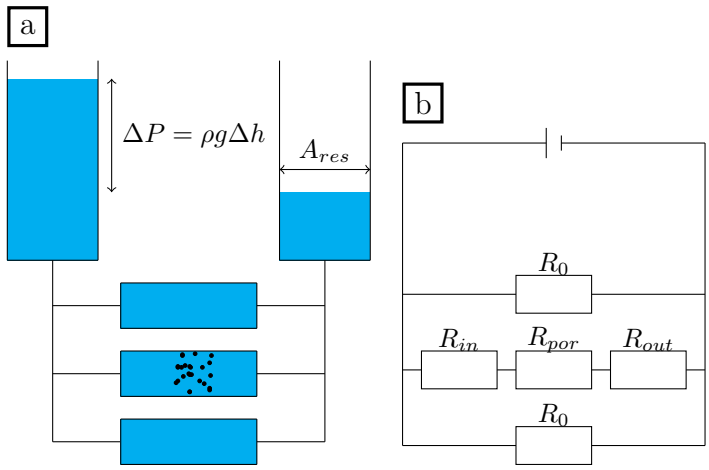

Figure 5.7.: (a) Schematic of the channel geometry of the used microfluidic samples. The middle channel contains the porous structure to be studied, the two empty channels serve as references for the calibration of the velocity measurements. (b) Equivalent circuit diagram with hydrodynamic resistances. The middle channel is split into three resistances. The objective of the permeability measurement is the determination of R_{por}.

The constant-head method yields accurate results, if the permeability k_{por} of the porous structure is low compared to the permeability of the in- and outlets k_0. For porous structures with a permeability that is comparable to k_0, the results are not as reliable. This is similar to the measurement of an electrical resistance which has about the same resistance as the leads that are used for the measurement. For example, in some measurements $\bar{u}_{por}$ can be faster than $\bar{u}_{ref}$ due to inaccuracies. The result of such an error would be a negative permeability for the porous structure, which does not make any sense and, hence, structures with very high permeabilities should be avoided.

5.3.2. Falling-head method

In contrast to the constant-head method, where the fluid reservoirs were so large that there is practically no change in the applied pressure during the time of a typical measurement, the falling-head method uses smaller reservoirs and takes advantage of the resulting decrease in the applied pressure, which is related to an excess volume in one reservoir. When the fluid is flowing through the porous medium, the excess volume in the reservoirs decreases until the two water levels are on equal height and the excess volume is zero. Thinking in analogies, this is comparable to a capacitor that is discharged across a resistance. The decrease in applied pressure will be exponential (see footnote) and since we already know that $\bar{u} \propto \Delta P$, the following differential equation must hold for the mean particle velocity[12]:

[12]The flow is driven by an excess volume $V = A_{res}\Delta h$, which generates the pressure drop $\Delta P = \rho g \Delta h$ across the sample. These two equations give $V = A_{res}\Delta P/(\rho g)$. The time derivative of the excess volume is related to the volumetric flow rate by $dV/dt = 2Q$. The factor of two stems from the fact that if the water column on, say, the left sinks due to the flow through to the structure, the water

$$\frac{d}{dt}\bar{u} = -\tau^{-1}\bar{u}, \tag{5.9}$$

where $\tau = \eta L A_{res}/(2A\rho g k)$ is a characteristic decay time. The decay time can be obtained by measuring the time development of the mean particle velocity. We cannot measure the change of the particle velocity continuously, as we have to average over many particle trajectories to get reliable values for $\bar{u}$. So, we have to measure $\bar{u}$ at several times to capture its decay and determine τ. Principally, two data points would suffice, if the particle density in the sample was high enough, but taking more data points is advisable to get accurate results and also check that there is nothing wrong with the sample, e.g., leakage or clogging. The only restriction is that the measurements must be short compared to the decay time, since otherwise the pressure would also change significantly during the measurement. In addition, the cross-sectional area of the sample A, i.e., its height multiplied by its width, and the cross-sectional area of the water reservoirs A_{res} must also be measured to be able to determine the permeability.

An exemplary measurement of the decay of the mean particle velocity is shown in figure 5.8. For this measurement a colloidal suspension[13] of particles with diameters $d = 2\,\mu m$ and $d = 3\,\mu m$ was injected into a sample that contained a structure of randomly placed circles with porosity $\phi = 0.91$. The sample was similar to the one shown in figure 5.3. A high porosity was chosen to give a high permeability which would result in relatively low decay times that can be measured more easily. The height of the sample was $19 \pm 0.3\,\mu m$ and the length $8150 \pm 50\,\mu m$. As we stated before (see 3.2.1), increasing the height will enhance the fluid flow tremendously and, thus, shorten the decay time, which is proportional to h^{-3}. The time between the first and the last measurement was 3 h. Each data point in figure 5.8 corresponds to a measurement of about $2\,min$, which is a short time span relative to the decay time. This is important, because it avoids that the pressure changes significantly during a measurement. The individual measurements were performed at an interval of $15\,min$. For both particle species an exponential decay of $\bar{u}$ with comparable decay times is observed. The white symbols correspond to particles with $d = 2\,\mu m$ and the red ones to $d = 3\,\mu m$. Fits of exponential decays to the data points, shown as solid lines, give $\tau_{2\mu m} = 4212 \pm 68\,s$ and $\tau_{3\mu m} = 4701 \pm 108\,s$. From the decay times a total permeability[14] for the structure can be calculated, which works out to $k_{tot} = 2.91 \cdot 10^{-11}\,m^2$ for $\tau_{2\mu m}$, and $k_{tot} = 2.60 \cdot 10^{-11}\,m^2$ for $\tau_{3\mu m}$. So, the total permeability for each particle size gives accurate results. These total permeabilities can also be used to calculate the permeability of the porous part of the structure, which gives $k_{por} = 2.07 \cdot 10^{-11}\,m^2$ for $\tau_{2\mu m}$, and $k_{por} = 0.81 \cdot 10^{-11}\,m^2$ for $\tau_{3\mu m}$.

column rises on the right. Putting in the excess volume and using Darcy's law to replace Q yields $d\Delta P/dt = -2A\rho g k/(\eta L A_{res})\Delta P)$. Using $\Delta P \propto \bar{u}$ results in (5.9)

[13] $0.25\,\mu l$ of CML latex particles with $d = 2\,\mu m$ and $0.85\,\mu l$ of CML latex particles with $d = 3\,\mu m$ from Invitrogen were dispersed in $100\,\mu l$ deionized water.

[14] For the determination of the total permeability of the middle channel we first have to calculate the permeability of the whole microfluidic sample which consists of three channels in parallel. The two empty reference channels had lengths of $8020\,\mu m$ and $8428\,\mu m$, and heights of $18.96\,\mu m$ and $19.11\,\mu m$. The channel in the middle which contains the porous structure had a length of $8046\,\mu m$ and a height of $18.89\,\mu m$. The calculation goes along the lines shown for the constant-head method.

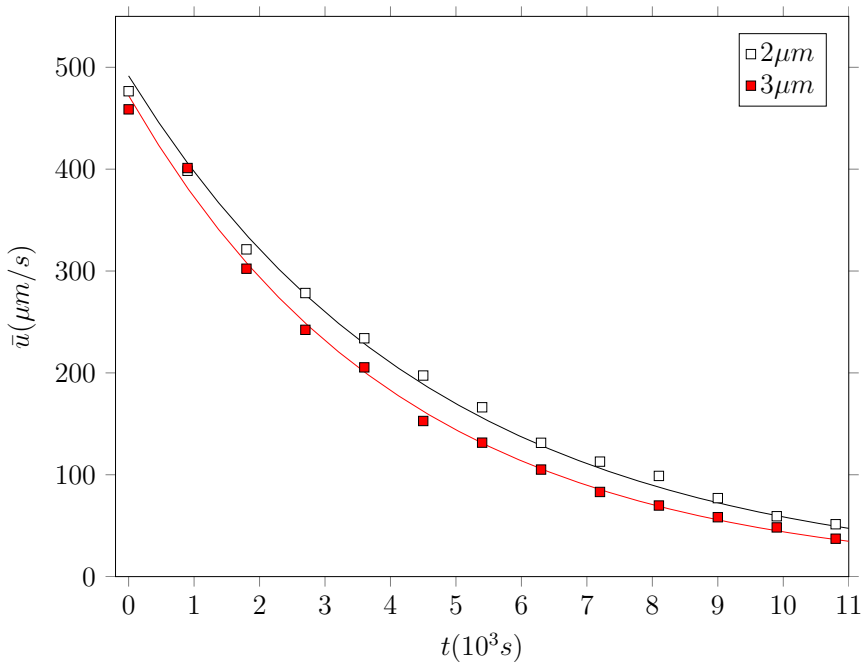

Figure 5.8.: Time development of mean particle velocity $\bar{u}$ for particles of diameter $d = 2\,\mu m$ (white) and $d = 3\,\mu m$ (red). For both particle species an exponential decay of $\bar{u}$ is observed. From the corresponding fits the decay times $\tau_{2\mu m} = 4212 \pm 68\,s$ and $\tau_{3\mu m} = 4701 \pm 108\,s$ can be determined, which allow a calculation of the permeability of the structure.

The large deviation of the two values does not indicate an inaccuracy of the method per se, but is a consequence of the fact that the porous part is very small compared to the total size of the whole sample.

The idea of this experiment was to show that one can obtain the same permeabilities with particles of different sizes and no calibration of the relation between $\bar{u}$ and $\bar{v}$. Of course, using only one particle species would be more practical to measure the permeability, because this would allow for a higher particle density and, consequently, shorter measurement times.

The falling-head method has some clear advantages over the constant-head method. The first one is that the only needed assumption is the proportionality between applied pressure ΔP and the mean particle velocity $\bar{u}$, which we have validated in many experiments. This is the same assumption we use in the constant-head method, but the big difference is that the reference channels for the calibration are not needed. So, the additional requirement that the reference channel geometry and, therefore, the proportionality between ΔP and $\bar{u}$ is the same in both channels is not essential. It is also not necessary to measure in the in- or outlet of the sample, because the proportionality also holds inside the structure. In principle, this implies that any small field of view at any position of the sample can be used. Only parts where Brownian motion and steric repulsion of the particles play a major role should be avoided. The in- and outlet is not needed to perform a permeability measurement which would allow to fill the whole chan-

nel with a porous structure. Theoretically this method can be used for any sample, but in practice a drawback of the falling-head method diminishes its applicability for permeability measurements. For structures with low permeabilities, the characteristic decay times become very large which in turn would increase the required measurement times to impractical levels. One way to circumvent this problem would be to simply make the structures larger and especially higher. The permeability of an empty flat channel is $k = h^2/12$, but in addition to the permeability the cross-sectional area $A = wh$ is also included in the expression for the characteristic decay time τ, which means that by scaling the whole sample up by a factor of 2 the decay would decrease by a factor of 16. In addition, one can also reduce A_{res} to reach arbitrarily low decay times.

In this work we will restrict ourselves to the constant-head method to measure permeabilities.

6. Relation between permeability and pore space structure

The upcoming chapter addresses the permeability measurements of ten porous structures (see figure 6.1) made of either randomly placed overlapping monodisperse circles (ROMC) or randomly placed overlapping monodisperse ellipses (ROME). Furthermore, the permeabilities of another ten structures where the two phases have been exchanged (see figure 6.5), i.e., structures where the void phase consists of circles (EROMC) or ellipses (EROME) were also measured[1]. The results for both types were compared to permeabilities that were obtained by lattice Boltzmann simulations[2].

The permeability is one of the most important and for many purposes, like the design of a drainage ditch [73], the only relevant quantity. We have mentioned several times in chapter 2 and 3 how complicated the prediction of the permeability of a porous structure by simple means is, as its structure can be very complicated. It is, thus, crucial to know which structural information is most important to predict the permeability.

The Katz-Thompson model, which was introduced in 3.2.2, is very successful in predicting the permeability of a porous structure. Its drawback is that it does not exclusively use purely geometrical quantities, but also relies on the conductivity of a structure. We tested the applicability of the Katz-Thompson model by performing simulations of the electrical conductivities of the investigated porous structures that yield the formation factor. The finding is that the Katz-Thompson law yields values that are comparable to our measured permeabilities. It is the objective of this chapter to introduce a formula for the permeability which only uses structural information of the sample. An additional requirement will of course be that only quantities which can be readily determined are used. Since the practical merit of a theory increases with decreasing number of input parameters, we restrict ourselves to a few parameters.

First, the results of the permeability measurements of two series of ROMC and ROME structures covering the full range of porosities, from the percolation threshold on, are presented. A formula for the permeability is proposed, which only uses purely geometrical parameters of the structure, i.e., only parameters that can be obtained by looking at the structure. The parameters used are the Euler characteristic of the sample-spanning fluid phase, the critical pore diameter and the number of grains that form the sample. The main advantage of this formula is its independence of the percolation threshold, which cannot be extracted from single samples.

[1] The measurements for the permeabilities of the ROMC and ROME structures were carried out by Christian Scholz and by Daniel Hirneise in case of the EROMC and EROME structures.

[2] The simulations were performed by Jan Götz in the group of Ulrich Rüde.

The number of grains that form the structure of our samples is only known, since we generate them artificially, that is, grain after grain is added until the desired porosity is reached. This is a problem for naturally occurring or arbitrary porous structures, where one does not know the precise number of grains, because they cannot be clearly distinguished and the precise formation process is unknown. Therefore, an effective number of grains is introduced, which can be determined from the perimeter, area and Euler characteristic of the pore space.

When the number of grains is replaced by the effective number, we still find excellent agreement with the measured permeabilities of the ROMC and ROME structures. Naturally, the question arises, how universal and, therefore, useful such a simple expression can be. So, secondly, we performed permeability measurements on two series of EROMC and EROME structures, which have a totally different morphology, to check if the formula still yields useful predictions of the permeability. It turns out that prediction and measured results far off the percolation threshold are still in fair agreement for the EROME structures, but strongly disagree close to the threshold. For the EROMC structures significant deviations exist over the whole range of porosities. We discuss possible reasons for this discrepancy.

6.1. Permeabilities of Boolean models

In section 2.4 Boolean models were introduced. We said that they show resemblance to naturally occurring porous media and, hence, are of interest to understand flow properties in such media. For our studies we generated ROMC or ROME structures of circles with a radius $r = 30\,\mu\text{m}$ and ellipses of aspect ratio of 8 with a major axis length of $a = 84\,\mu\text{m}$. The size of the structures is $4000\,\text{px} \times 4000\,\text{px}$, which corresponds to $3.5\,\text{mm} \times 3.5\,\text{mm}$ in the experimental realizations. The radius of the circles for the ROMC structures was set to $r = 34\,\text{px}$ corresponding to $30\,\mu\text{m}$ and the major axis length to $a = 96\,\text{px}$ for the ROME structures giving an aspect ratio[3] of 8. The two series that were used for our experiments are shown in figure 6.1. Starting at a value of $\phi = 0.85$ on the very left[4], the porosities decrease from left to right until they are close to the respective percolation threshold, below which there is no sample-spanning cluster of void space and no fluid can flow through the structure. In figure 6.1 only the open pore space, that is, the part that is accessible by the fluid is shown as white area. Similar open porosities for the ROMC and ROME structures were chosen to make the results comparable. As the porosity comes closer to the percolation threshold, the individual grains start to overlap more frequently, until only a few pathways for the fluid remain. This, of course, has a significant influence on the transport properties of these structures.

Table 6.1 summarizes the geometrical and dynamical properties of the ROMC and

[3]The major and minor axes of the ellipses were chosen to result in an equal area for ellipses and circles, so that the same number of ellipses covers, without overlapping, the same area as the circles.

[4]Higher values for the porosities were not studied, because the accuracy of the permeability measurement decreases as the porosity goes up. This issue has been discussed in 5.3.1.

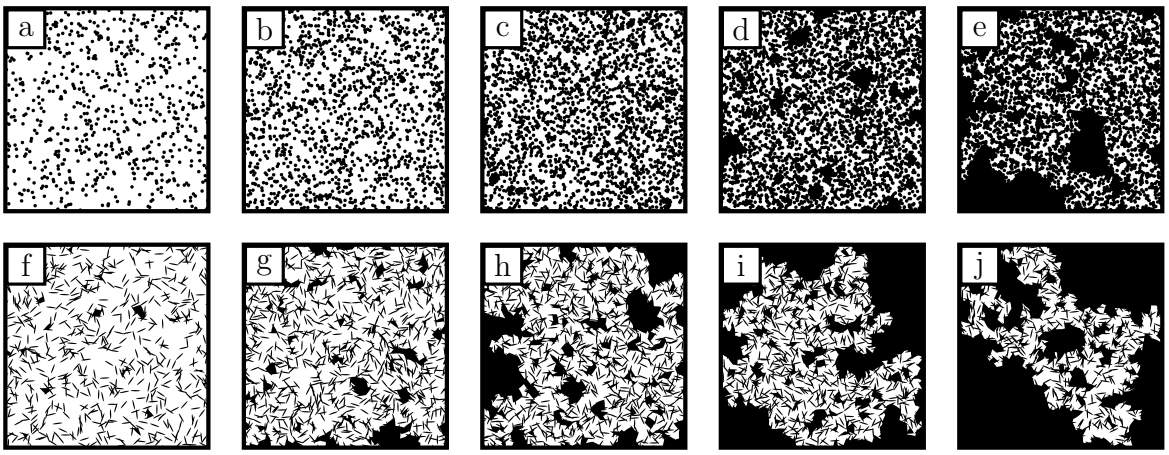

Figure 6.1.: Boolean models generated from randomly placed overlapping monodisperse circles (ROMC) with radius $r = 30\,\mu m$ (a-e) and ellipses with aspect ration of 8 and a major axis length $a = 84\,\mu m$. On the very left the structures (a,f) have a porosity of about $\phi = 0.85$. From left to right the porosities decrease until the respective percolation threshold of about $\phi_{cc} \approx 0.32$ for circles or $\phi_{ce} \approx 0.66$ for ellipses with aspect ratio of 8 is reached.

ROME structures. The geometrical parameters (ϕ, ϕ_o, χ and χ_o) were determined with the open-source software PAPAYA [124] which uses a marching squares algorithm to minimize discretization errors. The critical pore diameters D_c were determined using the Euclidean distance transform [125], which assigns the shortest distance to the next obstacle to each point of the pore space. Next, starting from the largest value of this Euclidean distance map, thresholds for the highest allowed values are lowered until a continuous path through the structure forms. The threshold value for which the first continuous path is obtained is the critical value D_c. The critical value D_c has been calculated for the two-dimensional structure, but since our structures are three-dimensional, the critical pore diameter is limited by the height of the sample, which is set to $8\,px$. Therefore, if $D_c > l_c$, the critical pore diameter is given by l_c.

The experimental realizations of these structures were generated by soft lithography. The length of the resulting sample was $10 - 11\,\mathrm{mm}$, the height $8 - 10\,\mu\mathrm{m}$ and the width $3.5\,\mathrm{mm}$. The porous structures that were investigated were contained in the center of these samples and had a size of $3.5\,\mathrm{mm} \times 3.5\,\mathrm{mm}$.

The permeabilities of the structures were determined by the constant-head method. The applied pressure was in the range $\Delta P = 10 - 50\,\mathrm{Pa}$. As probe for the fluid flow, an aqueous suspension of polystyrene particles with a diameter of $1.3\,\mu\mathrm{m}$ was injected into the samples. The permeability was calculated by measuring the mean particle velocity in the channel containing the structures and in the empty reference channels. Possible local variations in the mean particle velocity were accounted for by measuring at different positions in the channels and averaging over the obtained velocities.

In addition to the experimental values, numerical values for the permeabilities were obtained by the massively parallel lattice Boltzmann application network (WALBERLA). The structures that were used in the experiment were modelled by a lattice of size

Table 6.1.: Geometrical and dynamical quantifiers for ROMC and ROME structures shown in figure 6.1. D_c and l_c are given in units of lattice sites.

	ϕ	ϕ_o	N	χ_o	D_c	l_c	$k_{exp}/(cl_c^2)$	$k_{sim}/(cl_c^2)$	σ/σ_0
ROMC									
a	0.850	0.850	754	-520	100.018	8	0.641	0.6696	0.7031
b	0.701	0.700	1632	-724	51.306	8	0.385	0.3807	0.4405
c	0.551	0.549	2704	-635	21.984	8	0.137	0.1575	0.2107
d	0.418	0.401	3968	-395	11.506	8	0.047	0.0414	0.0764
e	0.365	0.298	4592	-220	2.421	2.421	0.0158	0.0273	0.0118
ROME									
f	0.854	0.850	771	-352	67.429	8	0.3598	0.3333	0.3787
g	0.751	0.700	1387	-275	41.254	8	0.118	0.1193	0.1501
h	0.684	0.549	1840	-146	6.275	6.275	0.0385	0.0355	0.0392
i	0.639	0.400	2176	-80	6.245	6.245	0.02	0.0174	0.0133
j	0.651	0.266	2064	-45	5.957	5.957	0.00696	0.0112	0.00851

$8 \times 4000 \times 4000$. A pressure of $\Delta P = 50\,\mathrm{P}a$, which is comparable to the pressures used in the experiment was assumed.

For a comparison of the obtained simulated and experimental values of different measurements the correct normalization is important. Especially close to ϕ_c where l_c can become very small it is crucial to not compare the raw permeabilities directly, but to first normalize them, that is, compare $k/(cl_c^2)$ of different structures. As we also recall, the Katz-Thompson law (3.10) stated that this value should be equal to the formation factor, i.e., $k/(cl_c^2) = \sigma/\sigma_0$.

In figure 6.2 (a) both the experimentally (blue, red large symbols) and numerical values (small white symbols), which are in good agreement, for the ROMC (squares) and ROME (triangles) structures are plotted versus the porosity. A lower porosity means that there are more obstacles hampering the flow of the fluid and, hence, less space for the fluid flow is available. One can also simply think in terms of boundaries: More obstacles means more boundaries and since the velocity at the boundary (no-slip condition) is zero, these will slow down the fluid flow. Thus, it is intuitively clear that the permeability decreases with decreasing porosity for both types of structures and vanishes around their respective percolation thresholds. Some of the ROME structures (i,j) have porosities slightly below their percolation threshold. Remember that the percolation threshold ϕ_c is only a sharp value in an infinite system. In a finite system, there can be percolation at any porosity different from zero, although the probability decreases substantially once the percolation threshold is crossed.

In figure 6.2 (b) the same permeabilities are plotted versus a rescaled porosity $(\phi - \phi_c)/(1 - \phi_c)$. This rescaling is motivated by Archie's law $\sigma/\sigma_0 = (\phi - \phi_c)^\mu/(1 - \phi_c)$, which relates the porosity to the formation factor appearing in the Katz-Thompson law (3.10). The exponent μ typically depends on the porosity and morphology of the pore

space. In 2D and close to the percolation threshold the exponent is expected to be universal[5], $\mu \approx 1.3$ [127]. The problem with Archies's law is that it is only valid close to the percolation threshold which makes it less applicable to natural porous media that can also have high porosities. After rescaling the permeabilities of the ROMC and ROME structures the data points approximately collapse on a single curve even far off the percolation threshold ϕ_c, which shows that Archie's law gives a good description for these structures. The scattering close to the percolation threshold, however, also shows some limitations of Archie's law. The disadvantage, again, is that Archie's law depends on the percolation threshold, which can, if unambiguously possible at all[6], only be determined, if the diagenetic process of the material is known.

In order to check the applicability of the Katz-Thompson law for our structures we performed numerical simulations for the conductivity with the help of COMSOL. The program solves the Laplace equation to calculate the (electrical) current density in the porous structures which then allows the calculation of the conductivity of the whole structure σ. In figure 6.2 (c) the permeability is plotted versus the formation factor. The dashed line indicates the Katz-Thompson law, i.e., it is a line through the origin with slope one. The very good agreement makes clear that the permeabilities of our structures can be well-approximated by the Katz-Thompson law over the full range of porosities. Thus, by measuring the critical pore diameter and the conductivity of a structure, its permeability can be predicted with very good precision in case of the ROMC and ROME structures.

6.2. Geometrical explanation of permeabilities

It is the objective of this chapter to come up with a new expression for the permeability that only depends on structural parameters of the pore space, which can be obtained from a specific sample, and, most importantly, is independent of the percolation threshold ϕ_c of the studied structures. We have mentioned in 2.4 that the structure of a pore space can be quantified with the help of Minkowski functionals of the pore space, i.e., Euler characteristic χ, surface S, and porosity ϕ or the area A. Here, we do not use the normal Euler Characteristic χ of the void space but the open Euler characteristic of the sample-spanning fluid phase χ_o, because inclusions of fluid inside the pore space make no contribution to the fluid flow and, hence, to the permeability. It is known from several stochastic processes [56, 128] that the Euler characteristic changes its sign close to the percolation threshold. In case of the open Euler characteristic, the value for χ_o converges to -1 as the percolation threshold is approached. Therefore we propose the following expression for the permeability k:

[5] Some groups have also reported deviations [126].

[6] Let us not be too philosophical, but suffice it to say that the determination of the percolation threshold of a specific realization of a model with fully known formation rules is still not unambiguous, because certain assumptions have to be made.

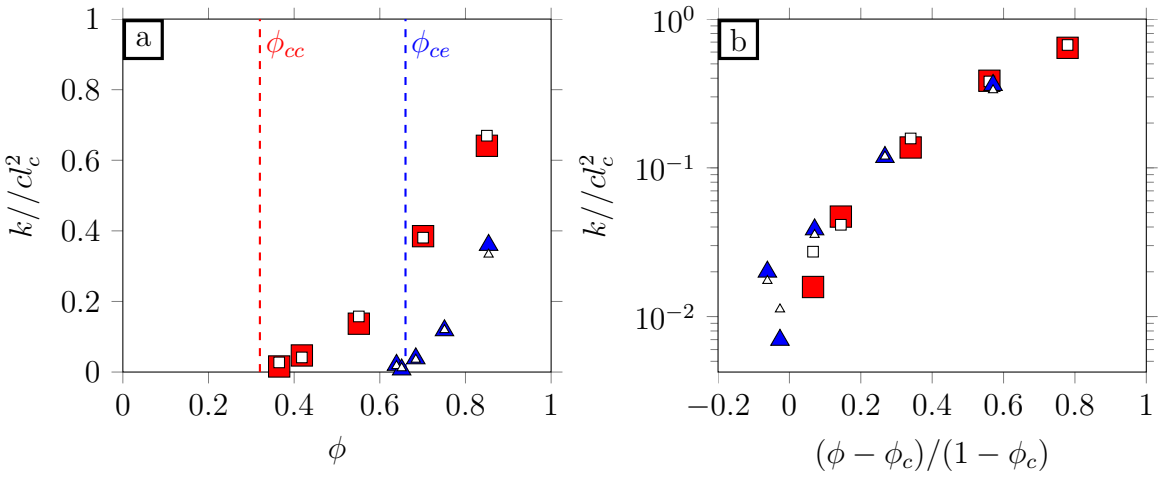

Figure 6.2.: (a) Experimentally (closed symbols) and numerically (smaller open symbols) determined permeabilities of ROMC (squares) and ROME (triangles) structures versus porosity. (b) The same permeabilities versus rescaled porosity. Data points of ROMC and ROME structures collapse approximately onto one curve. Finite-size effects lead to structures with negative rescaled porosities, i.e., porosities below the percolation threshold.

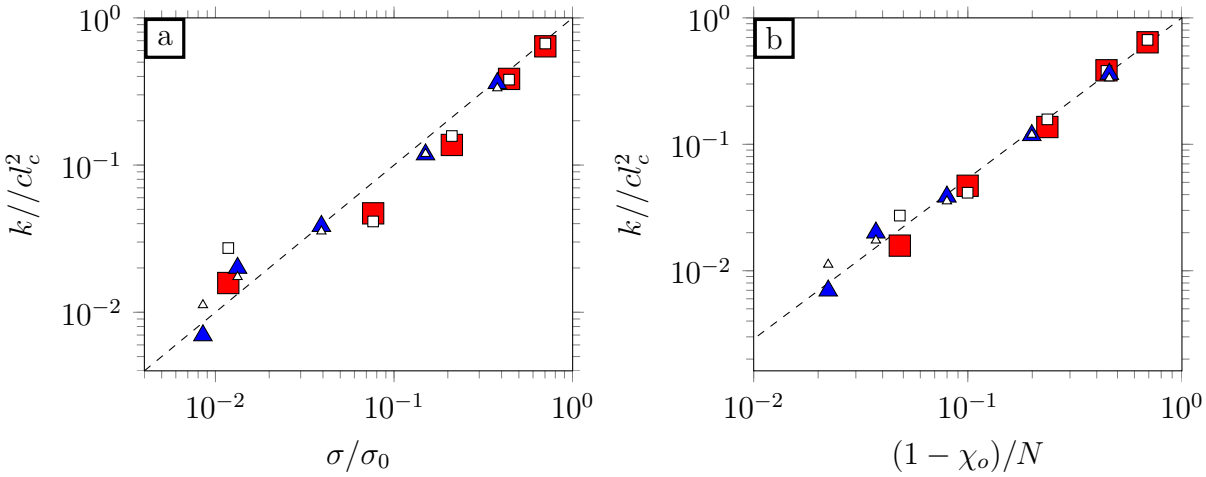

Figure 6.3.: (a) Experimentally determined permeabilities of ROMC (square) and ROME (triangles) structures vs. formation factor. The dashed line, which indicates Katz-Thompson law, is in good agreement with our data. (b) The same permeabilities vs. $(1 - \chi_o)/N$. The dashed line is a fit with $\alpha = 1.27$ of (6.1), which agrees very well with the permeabilities of the structures.

$$\frac{k}{cl_c^2} = \left(\frac{1-\chi_o}{N}\right)^{\alpha} \tag{6.1}$$

In case of our flat-channel geometry, the constant will be $c = 1/12$, because the permeability of an empty channel is $k = h^2/12$. We already know $1 - \chi_o$ from section 2.1.4 and we stated that this quantity, the genus, is a measure of the connectivity of the pore space. Everything else being the same, the higher this number, the better connected the pores are. Since this number is a function of the system size, i.e., it will be larger for larger systems with more grains, we divide it by the total number of grains N[7] that compose the structure and end up with $(1 - \chi_o)/N$, which gives the average number of connections that can be cut per grain. There is also another insightful way to interpret this expression: $1 - \chi_o$ gives the number of grain clusters in the sample and, thus, dividing this value by N corresponds to the number of clusters per grain. The number of clusters per grain will decrease as the grain density gets larger and grains start to overlap. So, it is a measure of the overlapping probability of the grains, which is related to their shape. More compact objects like circles are less likely to overlap and block the fluid flow. The choice of this expression can also be justified by looking at the two limiting cases: In the low-density limit, that is, for $\phi \to 1$, $(1 - \chi_o) \to N$ and finally $k = l_c^2/12$, the result for the flat-channel geometry. For $\phi \to \phi_c$, there will only be one path through the structure left, which leads to $(1 - \chi_o)/N \to 1/N \to 0$, i.e., a vanishing permeability. So, the two limiting cases are reproduced by equation (6.1).

Figure 6.3 (b) shows the permeability versus $(1 - \chi_0)/N$ in a log-log plot. All data collapse onto one curve (dashed line) with a slope of $\alpha = 1.27$. This value for the exponent is also very close to the critical exponent $\mu = 1.3$ for Archie's law. Based on the motivation we gave before, this accordance of (6.1) with the measured permeabilities indicates that it is the formation of grain clusters that results from overlapping grains that determines the permeability of a porous material. This overlapping probability is higher for elongated grains like ellipses. This can also be seen by looking at table 6.1, which shows that χ_o at the same ϕ_o is always substantially lower for ROME structures, i.e., there are fewer pathways for the fluid.

The effect of the overlapping probability and the consequent formation of extended grain clusters can also be seen in the fluid velocity fields that were obtained by simulations. Figure 7.2 shows velocity fields for low- ($\phi_o = 0.400$) and high-porosity structures ($\phi_o = 0.85$) of the ROMC and ROME type. The high-porosity ROMC structure (a) has a very homogeneous velocity field, as few grains overlap and can build large obstacles for the flow, whereas the ROME structure (b) already exhibits a wide spread of velocities due to overlapping ellipses that form dead ends in which the fluid is practically stagnant. The formation of such structures with dead ends leads to a lower fluid velocity and, hence, a lower permeability. The same effect can also be seen at the lower porosity. In (c) the pore space is still better connected relative to (d) and so there are more pathways for the fluid and, consequently, the fluid can flow with more ease, i.e., the permeability is higher. In case of (d) all the fluid that flows through the structure

[7] At constant porosity, increasing the system size also increases N.

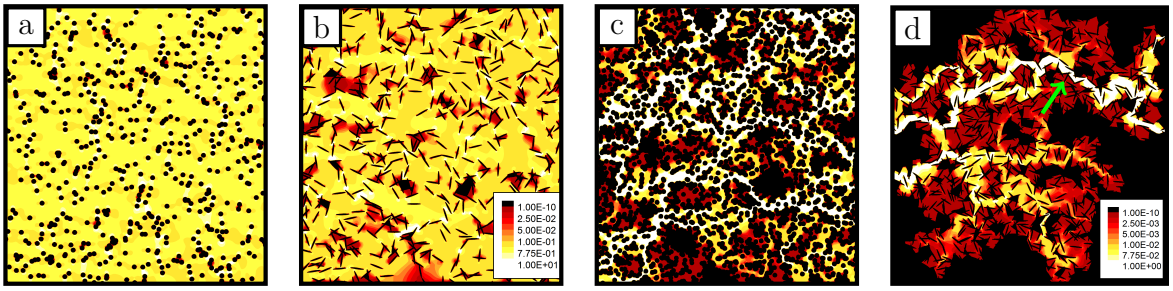

Figure 6.4.: Simulated fluid velocity fields for two ROMC (a,c) and two ROME (b,d) structures with equal open porosities $\phi_o = 0.400$ (a,b) and $\phi_o = 0.85$ (c,d). Clearly, the ROME structures form larger clusters and leave fewer connections in the pore space, which leads to more tortuous paths and larger stagnant areas in the medium, i.e., more resistance to flow. The unit is μm/s. Note that the color bar is logarithmic.

has to take just one small throat that is indicated by the green arrow. It is clear that this will give a large resistance to flow, because the pore space that contributes to fluid flow shrinks significantly.

The agreement between the measured permeabilities of the ROMC and ROME structures with the prediction of (6.1) is very satisfying. However, one problem remains. We stated at the beginning that it is the goal of this chapter to come up with an expression that allows a prediction of the permeability from purely geometrical parameters of the structure. One parameter in (6.1), namely N, can, unfortunately, not be determined by looking at the structure without any knowledge of the formation process. We know the value for N only because we generated the structure by a MATLAB program. Otherwise there would not be an easy way to tell how many grains the structure is composed of. Due to the overlap of individual grains at lower porosities it is generally not possible to determine N for any structure.

We already said in chapter 2 that the transport properties of random structures are similar, if their Minkowski functionals are comparable [55]. A structure with known porosity ϕ (or area A of the pore space) surface S and Euler characteristic χ can be reconstructed by a Boolean model with properly chosen grains, i.e., grains that have an area A_0, surface S_0 that give the best agreement with the given structure.

So, any given structure can be reconstructed by such an appropriately chosen Boolean model[8]. An attractive but bold idea is to use equations (2.5)-(2.7) as a way to define a new effective number of grains $\hat{N}$[9]:

$$\hat{N} = \frac{S^2}{4\pi A\phi} - \frac{\chi}{\phi} \tag{6.2}$$

[8]More details about Boolean models and Minkowski functionals can be found in the PhD thesis of Christian Scholz [129].

[9]The derivation is undemanding. First, (2.5) is used to replace the exponential functions in (2.6) and (2.7). Next, S_0 in (2.7) is substituted with the help of (2.6), which finally gives $N = \frac{\chi}{N} - \frac{S^2}{4\pi L^2\phi^2}$. Since L^2 is the total area of the sample, $L^2\phi = A$ and we have (6.3).

The advantage is that $\hat{N}$ can be calculated unequivocally for any structure with fully known geometry. The next logical step is to replace N by $\hat{N}$ in (6.1) and end up with:

$$\frac{k}{cl_c^2} = \left(\frac{1-\chi_o}{\hat{N}}\right)^{\alpha} \tag{6.3}$$

With the effective grain number, the expression can now be used for any kind of structure.

To judge the merit of (6.3) we calculated $\hat{N}$ for the ROMC and ROME structures and found it to be very close to the actual N[10], which means that equation (6.3) is able to predict their permeabilities just as well as equation (6.1) without full knowledge of the formation process.

The agreement of (6.3) and our measurements is very promising. The next obvious question one must ask is how universal this formula can be or if it is only valid for structures that are formed by some kind of randomly placed grains. To this end one has to use structures with a very different pore space morphology. We decided to use the same type of structures as before, i.e., structures that were composed of randomly placed overlapping monodisperse grains. The only difference this time is that the conducting and obstacle phase are exchanged, which gives completely different morphologies.

6.2.1. Inverted Boolean models

The two series that were used for our experiments are shown in figure 6.5. The open porosities are comparable to the values for the ROMC and ROME structures. The inverted structures show resemblance to porous media made from fused metal beads, wherein, e.g., heat conduction has been studied [130]. An immediately evident difference is that the pore structure which was convex for the ROMC and ROME structures is now concave. The obstacles in the inverted structures also do not have a minimum size like in case of the ROMC and ROME structure where the minimum size is set by the size of the individual grains.

The geometrical and dynamical properties of the EROMC and EROME structures are summarized in Table 6.2. The N that is given in this case has a different meaning than before, it is the number of holes (of elliptical or circular shape) that were punched into the structure. Here the porosity increases with the number of holes. The N for the inverted structures must not be compared with the N for the ROMC and ROME structures. The values are only shown for the sake of completeness.

As a quick intermezzo let us make an important note on the permeability measurement of structures with porosities close to the percolation threshold: The permeability measurement at low porosities is not as simple as for higher porosities, because the formation of only a few principal pathways for the fluid also influences the particle trajectories in the in- and outlet part of the sample (see figure A.1 in the appendix). Yet, these trajectories are used to calculate the mean flow velocity. Since all trajectories in the inlet have to pass through one of the orifices into the structure, they cannot follow straight

[10]The values for $\hat{N}$ can be found in table A.1 in the appendix.

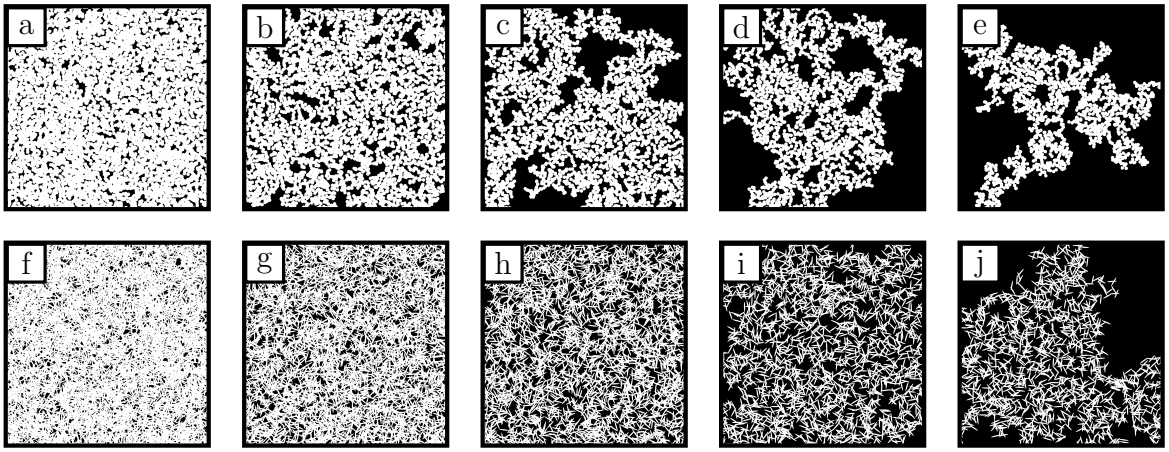

Figure 6.5.: EROMC and EROME structures generated from Boolean models of randomly placed overlapping monodisperse circles (ROMC) with radius $r = 30\,\mu m$ (a-e) and ellipses with aspect ratio of 8 and a major axis length $a = 84\,\mu m$. In contrast to figure 6.1 the fluid phase consists of the individual grains, which results in a very different morphology. On the very left the structures (a,f) have a porosity of about $\phi = 0.85$. From left to right the porosities decrease until the respective percolation threshold of about $\phi_{cce} \approx 0.68$ for circles or $\phi_{cee} \approx 0.34$ for ellipses with aspect ratio of 8 is reached.

Table 6.2.: Geometrical and dynamical quantifiers for EROMC and EROME structures shown in figure 6.5. D_c and l_c are given in units of lattice sites.

	ϕ	ϕ_o	N	χ_o	D_c	l_c	$k_{exp}/(cl_c^2)$	$k_{sim}/(cl_c^2)$	σ/σ_0
EROMC									
a	0.851	0.850	8726	-1842	47.97	8	0.304	0.425	0.478
b	0.742	0.700	6174	-1179	35.93	8	0.21	0.132	0.163
c	0.682	0.550	5273	-791	6.05	6.05	0.04	0.034	0.035
d	0.658	0.400	4835	-574	10.72	8	0.0228	0.021	0.026
e	0.668	0.278	5017	-378	5.85	5.85	0.016	0.019	0.0123
EROME									
f	0.850	0.850	9095	-8657	27.66	8	0.7416	0.536	0.6388
g	0.701	0.700	5822	-6348	21.54	8	0.186	0.297	0.3779
h	0.551	0.549	3882	-3865	18.29	8	0.0964	0.131	0.1724
i	0.417	0.400	2602	-1793	12.91	8	0.044	0.049	0.0636
j	0.388	0.270	2405	-1406	13.73	8	0.0111	0.017	0.0227

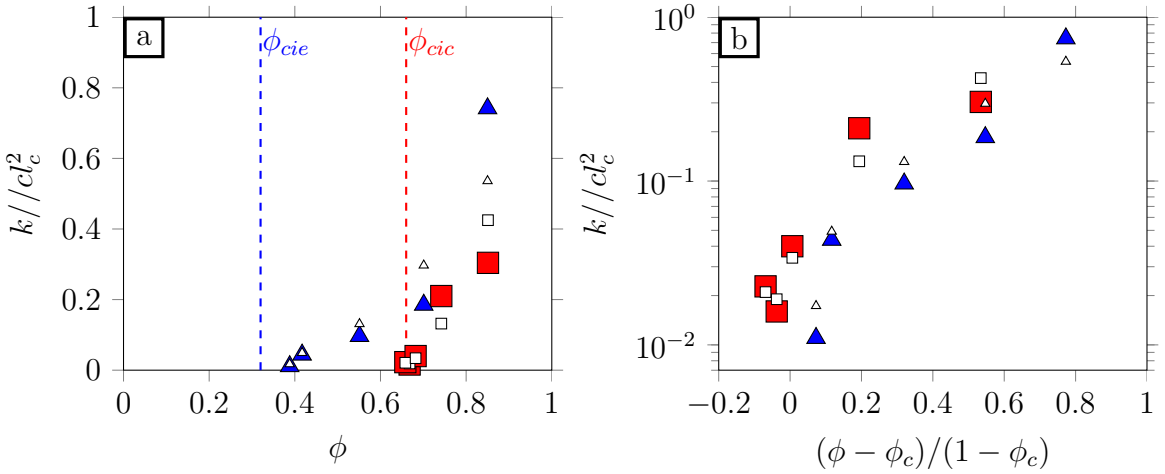

Figure 6.6.: (a) Experimentally (closed symbols) and numerically (smaller open symbols) determined permeabilities of EROMC (squares) and EROME (triangles) structures versus porosity. (b) The same permeabilities versus rescaled porosity. Data points of EROMC and EROME structures deviate strongly from a universal curve. Finite-size effects again lead to structures with porosities below the percolation threshold.

lines which means that the measured velocity will depend on the position in the inlet[11]. These complications make the measurement of the permeability more complicated and more prone to errors, as, in principle, the whole field of view must be measured. We still used the standard approach for the permeability measurement. As a test for the accuracy of this method we tried another method that was not described in chapter 5. We directly measured the flow velocity at the small orifice of the EROMC structure with $\phi_o = 0.278$ by determining the local particle velocity field and calibrating it with the help of the reference channel. By also measuring the area of the orifice and multiplying it by the average fluid velocity across that area the permeability was obtained. With the assumption that for a structure with very low porosity and a correspondingly low permeability the whole pressure drops across the porous part of the sample, a value for the permeability can again be calculated with the help of Darcy's law. This calculated value was in good agreement with the value previously determined with our standard approach.

When the permeabilities of the EROMC and EROME structures are plotted versus the porosity (figure 6.6 (a)), the same general trend as for the ROMC and ROME structures is observed. The permeabilities decrease with decreasing porosity and vanish at the percolation threshold. The percolation thresholds are now, of course, different. The threshold for the EROMC structures is $\phi_{cic} = 1 - \phi_{cc} \approx 0.68$ and $\phi_{cie} = 1 - \phi_{ce} \approx 0.34$[12]

[11] In case of a high-porosity structure these velocity values would be practically the same at any position in the sample. Another problem for low-porosity structures is that equation (5.4) is only valid if the individual resistances are well-connected, which is an unjustified assumption that certainly leads to inaccuracies in our measurements which are hard to estimate.

[12] Since, e.g., the structures ROMC and EROMC are formed by the same algorithm, the EROMC structure starts conducting just when the ROMC stops. Thus, $\phi_{cic} = 1 - \phi_{cc}$. This is generally true

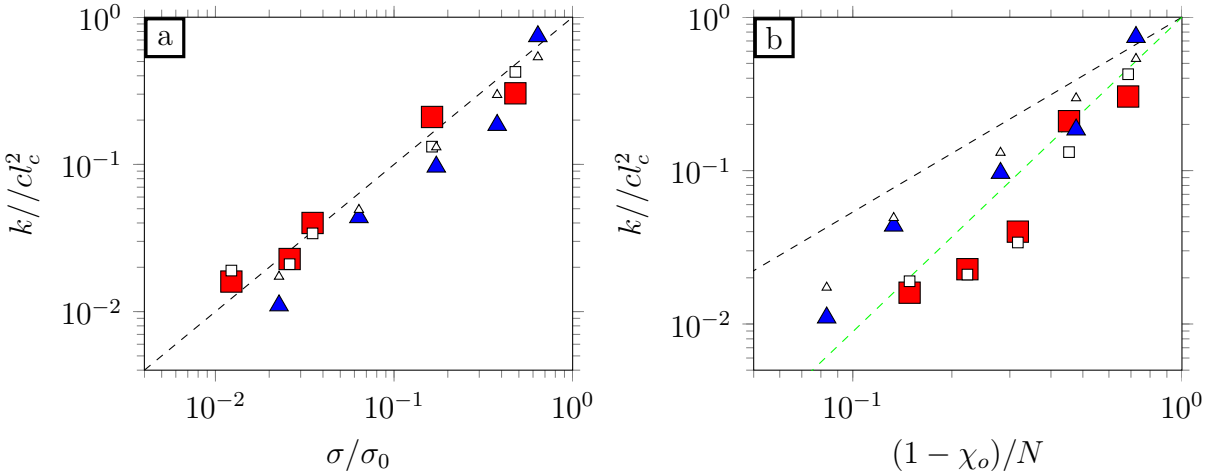

Figure 6.7.: (a) Experimentally (closed symbols) and numerically (open symbols) determined permeabilities of EROMC (square) and EROME (triangles) structures vs. formation factor. The dashed line, which indicates Katz-Thompson law, is in good agreement with our data. (b) The same permeabilities vs. $(1-\chi_o)/N$. The dashed line is the fit of (6.1) with $\alpha = 1.27$ that was used for the ROMC and ROME structures. The agreement with the permeabilities of the structures is bad. The green line corresponds to a fit to the data points yielding and exponent $\alpha_E = 2.05$ that agrees much better with the data.

for the EROME structures. The same reasons (higher probability for overlapping) that led to the formation of large clusters in case of the ROME structures, now leads to an easier formation of conducting clusters where the fluid can flow. As a result, the percolation threshold for the EROME is lower than for the EROMC structures.

Rescaling of the porosities (figure 6.6 (b)) again leads to a more universal behavior for both structure types, but the data points show larger deviations from a single curve than the ROMC and ROME structures. The agreement is again better far off the percolation threshold and exhibits stronger scattering of the data points close to the percolation threshold, which are mainly caused by finite-size effects.

Interestingly, the Katz-Thompson law is still able to predict the permeability with astonishing accuracy, as can be seen in figure 6.7 (a). The measured permeabilities all lie very close to the dashed line that represents the value calculated with the Katz-Thompson law. On the other hand, this is expected, because the values for the conductivity are simulated and take into account all the complexities of the pore space[13].

Figure 6.7 (b) shows the permeabilities versus $(1-\chi_0)/\hat{N}$ in a log-log plot. Unlike the data for the ROMC and ROME structures, there is no clear collapse onto a master curve and, therefore, a precise power-law behavior for the two structure types cannot be identified. The dashed black line corresponds to the fit that was obtained for the ROMC and ROME structures. For the EROME structures this fit still yields a somewhat

in 2D continuum percolation.

[13] At low porosities the simulations require finer and finer grids to give accurate results, i.e., the computational effort also increases.

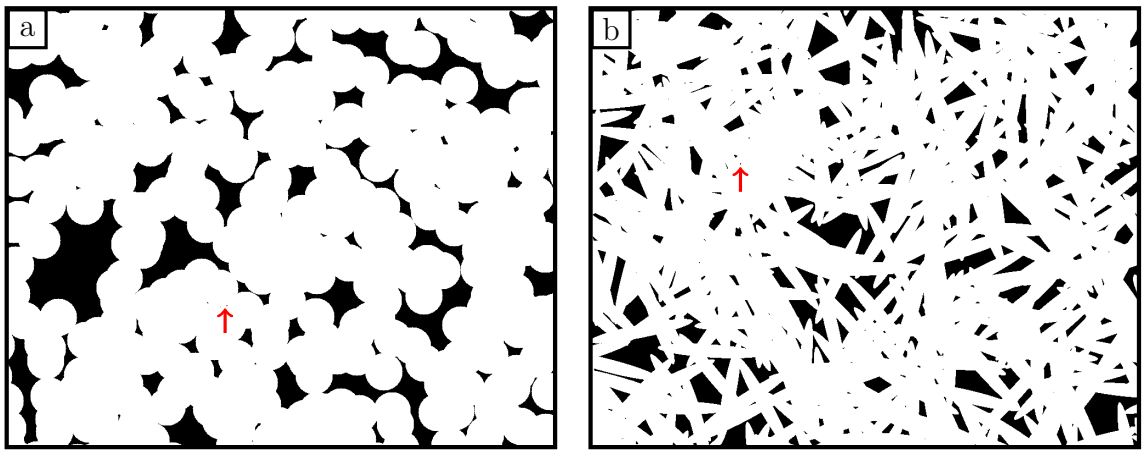

Figure 6.8.: Magnified views of small sections of EROMC (a) and EROME (b) structures with $\phi = 0.85$. As a result of the punching out of circles or ellipses both structures show small isolated obstacles (exemplarily indicated by arrows) that will affect the calculated value for $\hat{N}$. Such small obstacles do not occur in ROMC and ROME structures.

acceptable agreement with the measured data over a large range of permeabilities[14], but fails totally close to the percolation threshold. In case of the EROMC structure, however, there is practically no predictive power left in the fit over the whole range of porosities. Thus, equation (6.3) with a fixed exponent does not seem to be of universal value for any kind of structure and, clearly, further parameters of the pore space morphology must be considered. This is not too surprising, since the morphology of the inverted structures is completely different. The green dashed line corresponds to a fit to the EROMC and EROME data points which yielded an exponent of $\alpha_E = 2.05$, but even this curve does not reproduce the measurements in a convincing manner. This indicates that the motivation which gave rise to (6.3) might no longer be valid, that is, the calculation of $\hat{N}$ from the Minkowski functionals does not give a sound result.

A possible explanation for the stronger deviation as well as for the scattering of the data points and the discrepancy of simulated and measured values is the occurrence of small isolated obstacles in the EROMC and EROME structures (see figure 6.8) which are nonexistent in ROMC and ROME structures. These small obstacles can certainly have a substantial effect on the value of $\hat{N}$ without significantly affecting the permeability of the structure. Often it is also hard to tell, if these small obstacles are present in the experimental realizations of the porous samples as they can be very small and might also not be fully formed.

In order to give a quantitative analysis of the structural differences of the four structure types, we determined the distributions of obstacle sizes for structures with $\phi_o \approx 0.85$ and $\phi_o \approx 0.28$, which are shown in figure 6.9. For both porosities the distributions for the ROMC (black bars) and ROME structures (red bars) both have their maxima around the size of the grains, which is $\pi r^2 = 3632 px^2$ corresponding to $\log(3632) \approx 3.56$ in the

[14] A better agreement could certainly be achieved by using another exponent, but the point here is to show that the behavior that was observed for the ROMC and ROME structures is not universal.

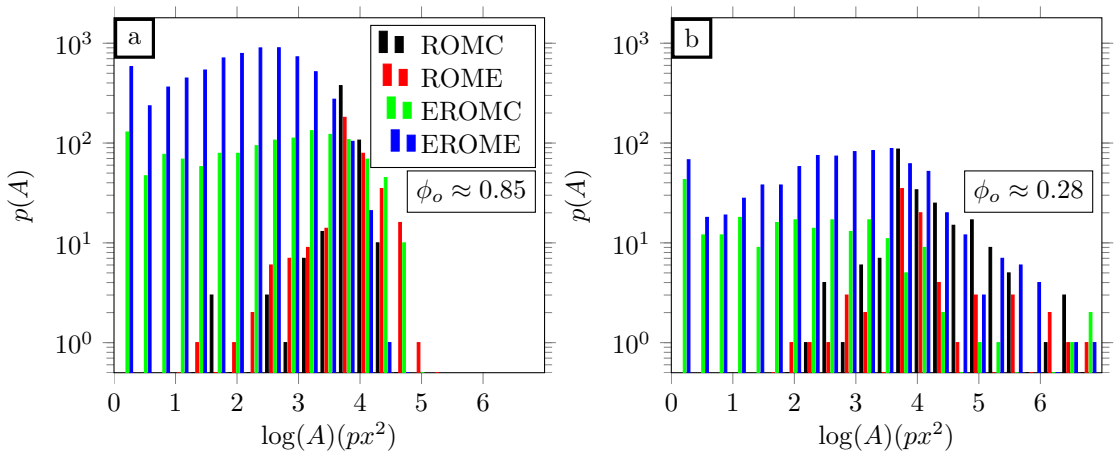

Figure 6.9.: Distribution of logarithmized obstacle sizes for the four different structure types for $\phi_o \approx 0.85$ (a) and $\phi_o \approx 0.28$ (b). The inverted structures (EROMC, EROME) show a huge number of very small obstacles due to the different formation algorithm, whereas the minimum size for the normal structures is set by the grain size.

distributions. The very few smaller obstacles simply stem from grains lying at the edge of the structure that are cut off. At the low porosity (b) the distributions extend to larger values, for larger clusters are formed by overlapping grains.

For the EROMC (green bars) and EROME structures (blue bars) the distributions look very distinct. For both types there are a very large number of tiny obstacles that only cover an area of a few px^2. This very large number of small obstacles might not have a big influence on the flow properties of the structure, but it will surely be accounted for in equation (6.3) which is a possible explanation why our formula does not work so well for EROMC and EROME structures.

We can also rationalize the lacking agreement in another way: In section 6.2 we motivated equation (6.1), or more precisely, the term $\left(\frac{1-\chi_o}{N}\right)$ by interpreting it as an overlapping probability of the individual grains and this could be easily understood for ROMC and ROME structures, where one just adds grain after grain[15] until the desired porosity is reached. When we tried to generalize equation (6.1) by the introduction of $\hat{N}$, which was obtained with the help of the Minkowski functionals, namely the area, surface and Euler characteristic of the pore space, we still had an excellent agreement with the measured data, i.e., $\hat{N}$ obtained from the Minkowski functionals was comparable with N. Yet, for the inverted structures the generalized equation did not produce satisfactory results. Thinking again about the motivation for equation (6.1), we see some complications arising with the inverted structures, as now the obstacles are formed by what is left over after punching out the circles or ellipses. Therefore, the question to be answered is: What is the probability for the left-overs to overlap? This question seems odd, because we cannot count something like the individual grains we had before. Even with full knowledge of the formation process we cannot come up with a number, which

[15]This also means that the number of obstacles one has put into the structure can be counted easily.

could also mean that the simple usage of the Minkowski functionals of the pore space is not the way to go. Maybe the solution to the problem with the inverted structure is to find a suitably chosen Boolean model that best replicates the generated structures and then relate their Minkowski functionals to the permeability.

7. Hydrodynamic dispersion in porous media

In the last chapter we studied the relation between the structure of a porous medium and its permeability, which is an integrated quantity that characterizes a porous medium, i.e., it gives just one number for a specific porous medium that incorporates all the complexities of the fluid transport in the respective porous medium. The tracer particles simply served as probes to determine the mean fluid velocity. The following chapter now investigates the actual motion of particles through the structure on an individual trajectory level.

During the particles' journey through the porous medium they are affected by the spatially varying velocity field generated by the boundaries of the pore structure and the always present Brownian motion. These two effects give rise to a spreading apart of particles that were initially localized in a certain region. The phenomenon is called hydrodynamic dispersion and has already been described in section 3.3. The main goal of the studies described in this chapter is to find the first-passage time distribution of a large number of particles in structures with varying porosities and relate them to the geometry of the porous structure.

We start by showing that it is very hard to capture trajectories of particles of sufficient length in a low-porosity structure by purely experimental means. The reason for this is that some particles enter stagnant parts by diffusion, where they can be trapped for experimentally inaccessible times (up to several days) until they escape again and continue to flow through the structure. These events are, however, crucial as they contain the information about the stagnant areas. As we have shown in chapter 5, it is possible to experimentally determine a particle velocity field of a porous structure with the help of tracer particles, which in turn allows us to solve the problem of the experimental determination of long trajectories by employing the experimentally measured particle velocity fields in an overdamped Langevin simulation to obtain a large number of particle trajectories, from which reliable and meaningful first-passage time distributions can be calculated. Employing this approach, we first study the movement of passive particles through three structures with porosities ranging from close to 1 down to very close to the percolation threshold, where large stagnant parts exist. The general finding is that for low-porosity structures which have stagnant areas the longest first-passage times can be related to the geometry of such areas, that is, their perimeter, area and the size of the transition zone to the flowing part (opening of the stagnant part). In addition, the motion of active particles was studied by slightly modifying the simulation algorithm to account for the motility of the particles. These active particles show a very distinct behavior, i.e., the maximum retention times are substantially lower, because they can

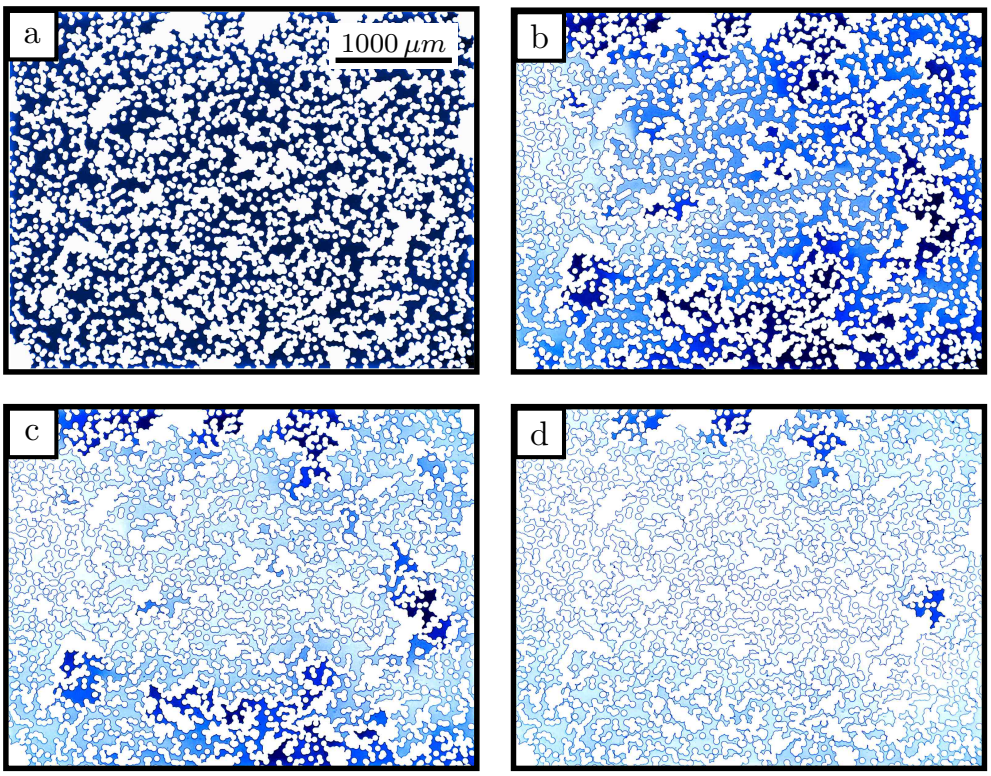

Figure 7.1.: (Color online) (a) Microscope image of a transparent porous structure made from PDMS which is filled with dyed (blue) water. Afterwards, pure water is injected from the left with a flow velocity of about 6 μm/s and displaces the dyed water. Snapshots are shown after (b) 5 min, (c) 10 min and (d) 33 min. Even after more than one hour, dyed water remains trapped in the stagnant regions of the structure.

escape faster out of stagnant regions, but on the other hand they do not necessarily follow the main, that is, fast streamlines through the structures as passive particles do, which increases the shortest transit times. We will explain every point in detail in the following.

7.1. Experimental challenges

The general experimental result, which also reveals the experimental challenges that one is facing, can be illustrated by a simple experiment which is shown in figure 7.1. A ROMC sample with an open porosity $\phi_o = 0.400$ was employed. First, dyed water[1] is injected from the right side into the initially empty sample until the whole porous structure is saturated, as can be seen in (a)[2]. Then, pure water is injected from the opposite side of the sample, whereby the dyed water is quickly displaced out of the

[1] A mixture of deionized water and Methylene Blue by Alfa Aesar was used.

[2] The original image, which was monochrome, has been colorized after improving the contrast to give the blue appearance in the pictures.

flowing parts of the structure, (b) and (c). Yet, even after a long time (33 min) some dyed water is still trapped in the stagnant parts of the structure from where it can only escape very slowly by diffusion (d).

This diffusion process is independent of the flow rate and leads to a measurable time separation of the two processes involved, namely the displacement by advection and the diffusion out of stagnant parts. This simple qualitative experiment already illustrates that the time scales for FPTDs in porous media with stagnant parts can be very long and, hence, experimentally hardly accessible. The diffusion coefficient of tracer particles are, or course, much smaller than of the dye molecules, which means that the time it takes a dye molecule to escape from a stagnant part is significantly smaller than for a small tracer particle. This makes it obvious that it is very impractical to determine the FPTDs by a straightforward experiment; the required time for a measurement would be too long, because the samples are only stable for a few hours, and it would also be hard to never lose a particle during a necessarily long tracing process for the evaluation of its trajectory and, thus, its transit time. However, if we want to gain full information about the transport of particles inside a porous structure, the particles, that enter a stagnant part, which in itself is a rare event, must be accounted for, because their transit times contain the information about the stagnant areas of the structure. An additional problem which renders the purely experimental approach infeasible is that our samples are only stable for a few hours, because the PDMS swells slightly, particles start to stick and bacteria and dirt inevitably enter the sample. Thus, measuring several FPTDs (representing a large enough number of trajectories) with the same sample at different flow rates is not possible. Consequently, we have to follow another route.

7.2. Simulation of particle trajectories

We have just seen that an all-experimental approach is not feasible to get the information we want. We solve the problem of measuring a sufficient number of long particle trajectories to come up with meaningful FPTDs, that is, FPTDs that include particles which enter stagnant areas from which they escape again and are advected to the end of the structure by performing a simulation of particle trajectories with a semi-experimental approach.

The first step, which is performed experimentally, consists of measuring the particle velocity fields of different porous structures with open porosities $\phi_o = 0.232; 0.582; 0.900$, which again are of the ROMC type. To this end, we inject a diluted suspension of fluorescent polystyrene particles[3] with a diameter of $1\,\mu$m into the samples and apply a pressure drop of $\Delta P = 2 - 40\,$Pa. The particle velocity fields were calculated with the procedure outlined in 5.1. The resulting particle velocity fields can then be used as input for an overdamped Langevin simulation. Such a simulation allows us to avoid the problems that the previously shown experiment made obvious, i.e., the trapping of particles inside stagnant regions for experimentally inaccessibly long durations. The particle motion during a time interval Δt is calculated by a simple algorithm:

[3]FluoSpheres yellow-green by Invitrogen.

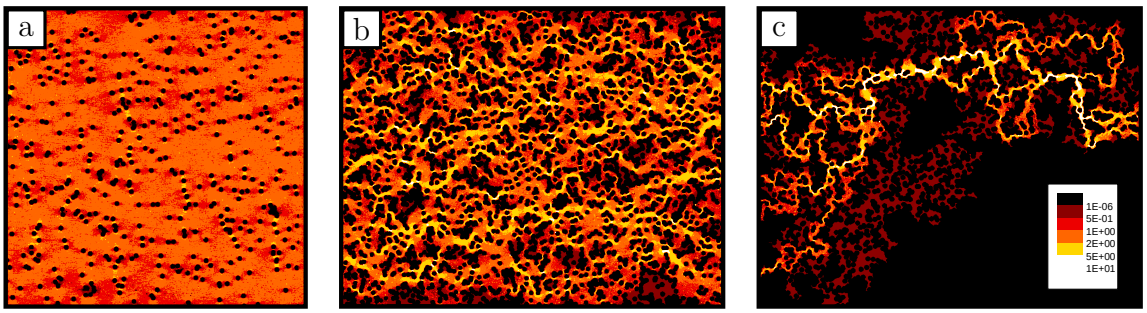

Figure 7.2.: Experimentally measured velocity fields of three porous structures with varying porosities. High velocities correspond to bright colors. Stagnant parts appear as dark brown areas. The shown scale is logarithmic and given in units of μm/s. The high-porosity structure $\phi_0 = 0.900$ (a) has a very homogeneous flow field. At lower porosities $\phi_o = 0.582$ (b) stronger velocity heterogeneities and stagnant parts occur, until at the lowest porosity $\phi_o = 0.232$ (c) only a few principal pathways, surrounded by large stagnant areas, are available.

$$\mathbf{r}(t + \Delta t) = \mathbf{r}(t) + c\mathbf{u}(\mathbf{r})\Delta t + \boldsymbol{\xi}(\Delta t). \tag{7.1}$$

Here, $\mathbf{u}(\mathbf{r})$ is the experimentally determined particle velocity field which represents the deterministic part due to advection by the fluid and $\boldsymbol{\xi}$ stands for a random displacement due to diffusion which is governed by a Gaussian distribution with zero mean and a width of $(4D_0\Delta t)^{1/2}$ with $D_0 = 4.3 \times 10^{-13}\,\mathrm{m}^2/\mathrm{s}$ and $\Delta t = 40\,\mathrm{ms}$. The constant c is used to adjust the flow rate through the structure. Since the flow is in the low-Reynolds number regime (doubling the pressure also means doubling the flow rate) we can use the particle velocity fields that have been determined for one pressure to easily calculate the velocity fields at a different pressure and thereby change the Péclet number. The time interval Δt was chosen to make sure that the largest particle displacements at the largest Péclet number, i.e., particles in the fastest flowing regions of the structure, do not exceed two particle diameters during one time step. This is a compromise between fast simulation and accurate results, which is providing realistic trajectories for our structures.

The mobility, i.e., the response to a force, of the particles will not be the same at any position in the sample. Closer to the boundaries and especially in narrow constrictions the mobility will be smaller. Since the velocity field of the particles is obtained from experimental data, hydrodynamic interactions between the particles and the structure are included when the trajectories are simulated according to equation (7.1). It should also be mentioned, that due to the quasi-two-dimensional sample, hydrodynamic interactions are rather dominated by the upper and lower walls than constrictions in the porous matrix, so that variations in the mobility should be small[4]. Thus, we assume a constant mobility throughout the sample.

[4]Another possible question might address the robustness of our method. We evaluated the effect of initial noise on the velocity field, we added Gaussian-distributed noise with zero mean and a standard deviation corresponding to 25% of the average particle velocity to the velocity field. When comparing the resulting FPTD with noise-free data, no significant deviations were found.

Some exemplary particle trajectories of the structure with $\phi_o = 0.232$ are shown in figure 7.3. In (a) the whole structure with experimentally determined trajectories is shown, whereas (b) shows simulated trajectories. It can be seen that there are many trajectories of diffusing particles in stagnant parts which could not escape during the measurement. The simulated trajectories, however, all start at the left end of the structure and reach the other side, regardless of whether they were trapped for long times in stagnant parts. (c) shows trajectories that were obtained by an experiment that lasted 30 minutes. The trajectories already demonstrate the wide range of velocities in such a structure. Particles move along the main transport paths in a rather straight way, because the velocities along these paths are high and, therefore, diffusion has a small effect. In stagnant areas (see dashed blue and red circle) particles show a clear random walk behavior, that is, the flow velocity therein is negligible. The experimental trajectories again illustrate the problem with the stagnant parts: They are only sampled by too few particles and some of them will not be able to escape during the measurement. An example of a particle that did not escape can be seen inside the black dashed circle. If such trajectories are used to compute a FPTD, these crucial trapping events are underestimated. Simulated trajectories shown in (d)[5] can easily avoid this problem. In the shown case the simulations cover a time interval of 20 h and, thus, include a large number of particles that enter stagnant parts and have enough time to escape again. The simulated trajectories, therefore, can explore stagnant regions and provide realistic information about the structure of the sample. It should also be mentioned that the shown example is not extreme by any means. Some of the simulated trajectories for the FPTDs that will be shown have a length of about 10^7 s or about 116 days. Such time scales are not accessible in our experiments and will, of course, be hard to obtain in any kind of experiment. Depending on the structure, these time scales can also easily be orders of magnitude higher.

The measured velocity fields of the used structures are shown in figure 7.2. The porosity decreases from left to right and, as can be seen, this has a strong effect on the heterogeneity of the velocity field. At a high porosity (a) the velocity field is very homogeneous, which means that all particles are moving through such a structure at a more or less constant velocity. For this kind of structure, one would also expect that the transport can be described by the standard advection-diffusion equation (ADE), because there are no large variations in the velocity field and the given structure is larger than its correlation volume, so that no finite-size effects are expected. When the porosity decreases (b) the velocity field becomes more and more heterogeneous and stagnant parts, which are shown in dark brown, start to occur. At porosities very close to the percolation threshold (c) only a few principal pathways for the fluid flow remain which practically carry all of the flow. These pathways are surrounded by large stagnant areas. Due to the velocity heterogeneities and the stagnant parts[6] the transport in

[5] Only a very small fraction of all the simulated trajectories are shown. In typical simulations more than 10000 trajectories were simulated.

[6] As we mentioned before, the distinction between velocity heterogeneities and stagnant parts is somewhat arbitrary. We could also just use the term "strong velocity heterogeneities" to imply the presence of stagnant parts, which are merely areas where the flow velocity is so slow, that diffusion

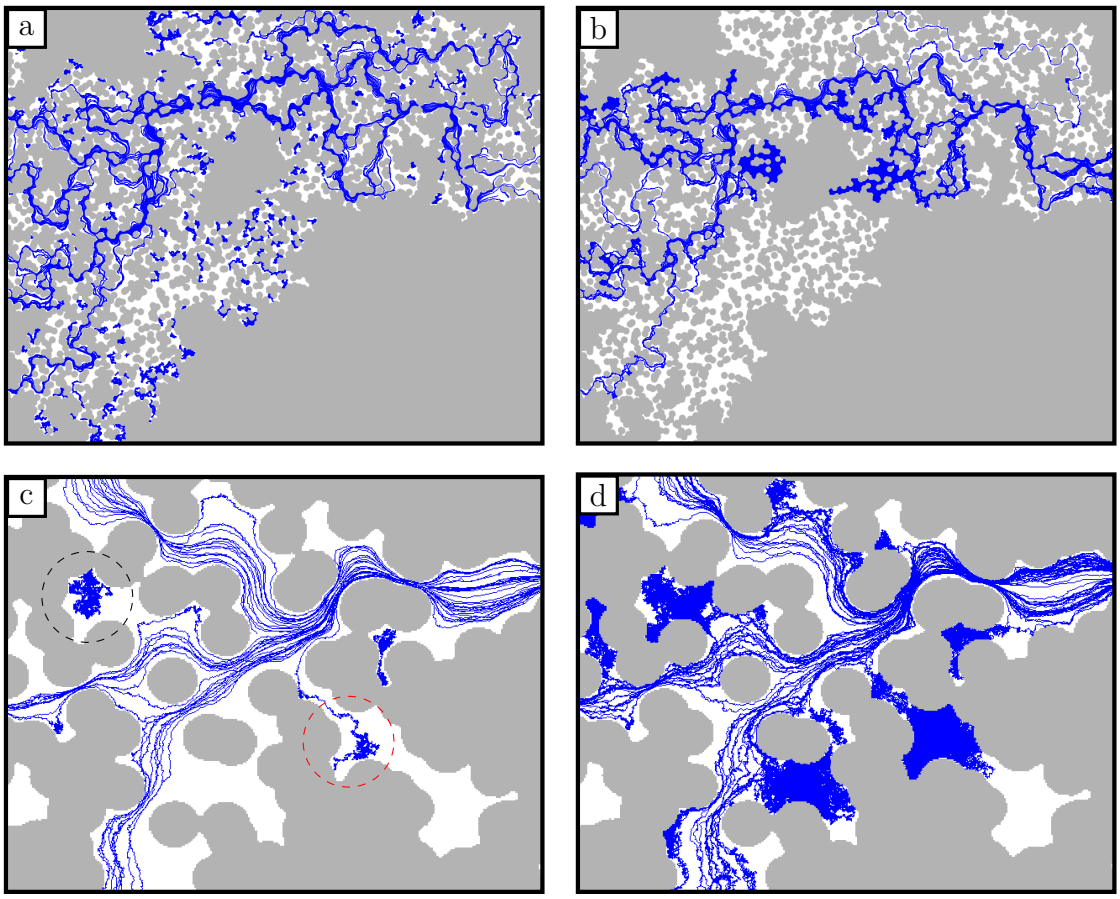

Figure 7.3.: Comparison of experimental (a), (c), and simulated trajectories (b), (d) of the ROMC structure with $\phi = 0.232$. (a) and (b) show the whole structure. The experimental trajectories (a) show particles that are advected along the main paths (compare to figure 7.2 (c)) and also diffusing particles that already were in stagnant parts at the beginning of the experiment and could not escape during the observation time. In the simulated trajectories (b) all particles start at the left and reach the other end of the structure, even if they spend a very long time in stagnant parts. (c) and (d) show a magnified part of the structure. (c) Experimental trajectories captured during 30 min. Mean flow direction is from left to right. The particles inside the dashed circles start in stagnant areas. Only the one in the red circle is escaping during the measurement time. (d) Particle trajectories obtained by a simulation with duration of 20 h. Particles can explore more stagnant areas and all particles that enter them will also be allowed to escape during the simulation.

structures with low porosities, like the ones shown in (b) and (c), is not expected to be well-described by an ADE.

7.3. Dispersion of passive particles

As promised in section 3.3 we will now address the influence of a nonhomogeneous flow field and the presence of stagnant parts on the FPTDs of passive particles. We mentioned in section 3.3 that the standard description of hydrodynamic dispersion is provided by the advection-diffusion equation (ADE), but that the transport that is often observed is anomalous, i.e., cannot be described by the ADE. The reason for this is the complex geometry of porous media which can give rise to a mixture of principal pathways, along which particles are transported by advection, and stagnant parts, wherein particles can only move slowly by diffusion. As a result one has two different time scales: $\tau_\mathrm{A} = L/U$ for advective transport, where L is the length of the porous medium and U a typical particle velocity. The other time scale is $\tau_\mathrm{D} = L_\mathrm{eff}^2/D_0$ for diffusive transport, where L_eff is an effective characteristic length of the stagnant parts and D_0 the diffusion coefficient of the particles. τ_A clearly depends on the flow rate, whereas τ_D is dictated by the morphology of the porous medium. In the past the length scale L_eff has often been used without exactly specifying how it is related to the geometry of the stagnant parts [49, 103, 131, 132][7], which is probably owed to the fact that the precise microscopic structure of the studied samples was not known.

The fundamental difference or better the advantage of our method is that we see the flowing particles inside the porous structure and can identify the stagnant regions by determining the velocity field. In previous studies the porous media remained black boxes and the interpretation of resulting FPTDs were more speculative[8]. The "characteristic" length L_eff, as anyone can tell by intuition, can obviously not just be some mean value of the extent of a stagnant part. Imagine a stagnant part with a circular shape that is connected to the flowing part of the structure by a small hole in its rim. The average time a particle spends in such a stagnant confinement would evidently depend on the size of its hole. So, if the time scale $\tau_\mathrm{D} = L_\mathrm{eff}^2/D_0$, which is only a function of L_eff, shall decrease, L_eff must be lower for the stagnant confinement with the bigger hole. Yet, this immediately reveals that one length scale is not enough to give an estimate for the mean sojourn time in a stagnant part. In section 7.4 we will resort to an equation from statistical physics that relates the perimeter, area, and size of the hole to the mean sojourn time of a stagnant part and, therefore, gives more insight into the transport

is dominating the transport.

[7] The effects of stagnant zones, i.e., "relaxation times independent of the flow rate" [49], were already well understood. We use the term time scale separation to describe the same phenomenon. It was also known that the role of stagnant parts increases strongly at low porosities. We do not want to claim that we figured out these phenomena, since research in this area has been going on for many decades.

[8] This is not meant to be discrediting any of the very decent works by other groups. Our approach also has its drawbacks, for example that the simulation certainly does not use a perfect velocity field, because of unavoidable imperfections in our measurement technique.

process through a porous structure.

The algorithm, which was explained in section 7.2, was used to simulate the motion for a large number (more than 10000 for each Pe) of particle trajectories. The starting positions are distributed uniformly at the left side of the structure. For each structure the Pe varied between 8 and 128. The resulting FPTDs for the three ROMC structures with $\phi_o = 0.900$, $\phi_o = 0.582$ and $\phi_o = 0.232$ are shown in figure 7.4. The Péclet numbers were calculated according to $Pe = LU/D$, where L is the length of the structure, and U the mean velocity of a typical particle[9] that is advected through the pore space. In the left column the resulting FPTDs for each structure are shown for different Pe in a lin-lin plot. For each consecutive FPTD Pe was varied by a factor of two by also changing the constant c in the simulations by the same factor. For the figures in the right column the transit time of each simulated trajectory was logarithmized and the resulting distribution plotted with a logarithmic ordinate to make the long-time tails visible. The corresponding fits to the ADE are shown as open symbols.

The results in figure 7.4 (a) for $\phi_o = 0.900$ are typical for a high-porosity structure where the velocity field is rather homogeneous and practically no stagnant parts exist. The particles are simply advected through the porous medium and do not undergo more complicated processes such as traveling along tortuous flow lines with widely varying velocities and entering stagnant areas. As the good agreement with the fits to equation (3.15) makes clear, these distributions can be explained by the ADE. Figure 7.4 (b) makes it even clearer since the only major change in the FPTD at lower Pe is a shift of the whole distribution to the right, i.e., the shape of the distribution does not depend on Pe. This is in stark contrast to the more interesting distributions of the two other structures with lower porosities. Figures 7.4 (c), (d) and (e), (f) already show long-tailed distributions, which cannot be well described by the fits. Even in the lin-lin plot and especially at high Pe significant deviations between our results and the fits exist. In particular, the tail is considerably underestimated. The disagreement is even more obvious in the logarithmic representation where the fits and the data are orders of magnitude apart. Clearly, the ADE principally fails to give an accurate description. It cannot account for the short-time as well as the long-time behavior of the FPTDs and, furthermore, fails to reproduce the shape of our results. This is no surprise since the ADE does not include any permeability heterogeneities and the effect of stagnant areas. Therefore, when the result of the ADE is fitted to such data, the dispersion coefficient will be wrongly overestimated [100].

The part of the tail, which can be seen in the lin-lin plot is mainly due to permeability heterogeneities, that is, different velocities along different paths through the porous structure. At this point it should be emphasized the mere existence of a long-time tail and the fact that the FPTD cannot be reproduced by the ADE does not automatically imply that there are stagnant parts. A primitive example without stagnant parts would be a medium consisting of parallel pipes with widely varying diameters and, thus, widely varying flow velocities which could easily give rise to a broad distribution of first-passage

[9] This mean value U was determined by dividing the length of the structure L by the time of the maximum in the FPTD, which is the typical advection time τ_{A}.

times. Such permeability heterogeneities, as was pointed out in the past and has been discussed and shown in section 3.3.6, can lead to broad and long-tailed distributions. But mind that the key difference is that such tails would depend on the flow rate and could therefore be identified by conducting measurements at different Pe. This is, of course, what was achieved by varying the Pe in the simulations. As Pe is lowered, the part of the FPTD which is mainly determined by advective transport is shifted to the right, whereas the events whose transit times are dominated by diffusion in stagnant parts are not strongly affected. Consequently, the long-time tails of the FPTDs at different Pe become very similar at long times (above about 10^5 s and 10^6 s in 7.4 (d) and (f), respectively), implying that the tail is only weakly flow dependent. This rather flow independent part, which might appear only at very long and hardly attainable transit times, incorporates the information about the stagnant parts. This also demonstrates that it makes sense to think in term of time scale separation between advective and diffusive processes.

7.4. Geometrical interpretation of long-time tails

The transport of particles through porous media, especially when the porosity is low and the structure is disordered, is a highly complicated process. A particle can be advected at varying velocities through the inhomogeneous flow field, then get trapped in a stagnant part, where it can diffuse around for a long time, until it escapes out of the stagnant region and is advected again. These steps can be repeated several times. Accordingly, no simple relation is to be expected between the FPTD and structural parameters of the structure.

7.4.1. Mean residence time in stagnant parts

The problem of the diffusive motion and the mean time it takes a particle to escape from a confined domain is, fortunately, a very general issue that is of interest in many disciplines. One example are biological processes, where a molecule is diffusing in a restricted area until it, after a certain escape time, reaches a specific target site and triggers a reaction [133]. Theoreticians have studied this mean-escape time problem in detail [134, 135]. The mean escape time of a particle confined in a domain with a small exit pore, in general, depends on the starting position of the particle inside the domain. In [135] it was shown that the mean escape time is proportional to $\ln(r/a)$, where r is the distance between the starting position and the exit pore of size a. Thus, the escape time does depend only weakly on the starting position. In case of exit pores that are small compared to the total boundary of the domain, the mean escape time does not depend on the starting position except for a small boundary layer near the exit pore [136]. A particle that does not diffuse across this boundary layer will escape relatively quickly and will therefore only have a very small effect on the FPTD. For particles that make it across the boundary layer the mean escape time becomes a well-defined quantity that is given by:

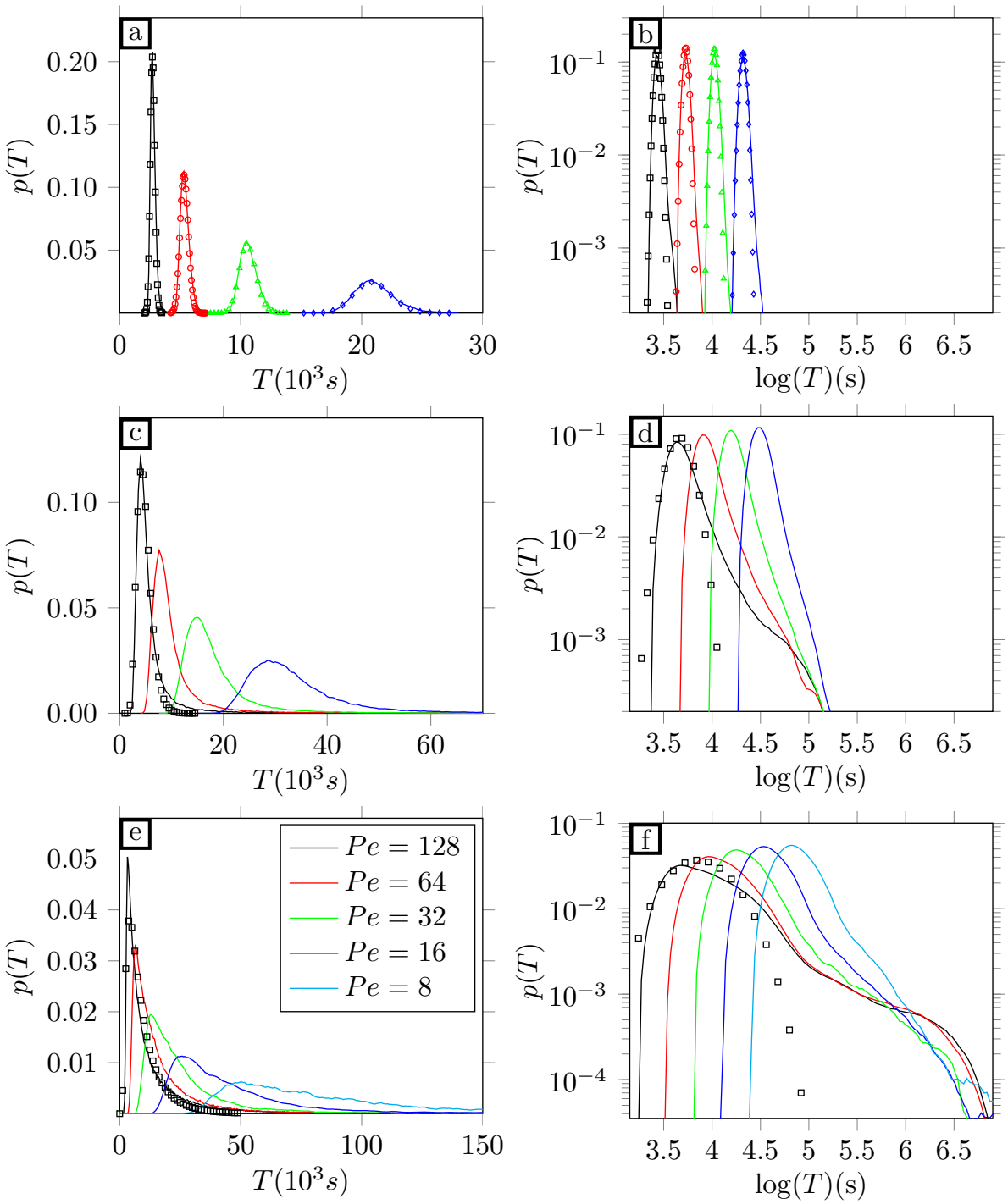

Figure 7.4.: Measured FPTDs for different Pe for three different structures (solid lines). The insets show the same data with a logarithmic time scale. (a) corresponds to $\phi_o = 0.900$, (b) to $\phi_o = 0.582$ and (c) to $\phi_o = 0.232$. The open symbols correspond to fits to the ADE. The highest Pe (black line) was 128 and each consecutive Pe decreases by a factor of two. The FPTDs of the low-porosity structure is in agreement with the ADE and shows no flow-independent long time tails, whereas the FPTDs for the two other structures show long-time tails that collapse for different Pe.

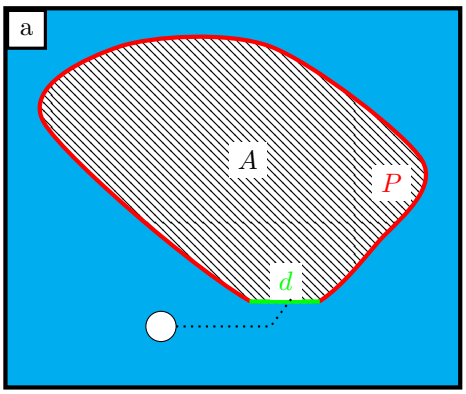

Figure 7.5.: A stagnant part with a small opening inside a porous medium. The cyan part correspond to areas where there is a considerable flow velocity. The stagnant part can be characterized by three quantities, namely its area A (hatched), its perimeter P (red) and the size of the small pore (green) that connects stagnant and flowing part d. A particle that is advected close to the stagnant part can enter by diffusion and will spend an average time τ in the stagnant part.

$$\tau = \frac{A}{\pi D_0} \ln\left(\frac{P}{d} + 1\right), \tag{7.2}$$

where A is the area of the domain, P its perimeter and d the length of the exit pore at the transition from stagnant to flowing part (see figure 7.5). The stagnant parts in our low-porosity structures were first identified by application of a velocity threshold to the velocity field, which gives a binary image, where stagnant and flowing regions are clearly distinguished. Of course, there is no really sharp transition from a flowing to a stagnant region, because in a disordered porous medium the flow velocity never drops exactly to zero, but becomes so small that diffusion totally dominates the transport of particles in stagnant parts on our time and length scales. Since we are measuring the particle velocities by following the trajectories of individual particles, even in a totally stagnant part a diffusing particle will result in a non-zero velocity field. Only by averaging over many particles or one diffusing particle over a long time, the velocity field would approach zero everywhere. However, this is not achievable in our experiments, because of low particle densities in stagnant parts and short measurement times. Still, the stagnant parts can be identified by looking at the particle trajectories and at the resulting velocity field[10]. As with the geometrical parameters of the porous structures in chapter 6, A, P and d were determined after identifying the stagnant areas by a marching squares algorithm, which generates contours for a binary image and minimizes discretization errors.

Equation (7.2) was used to calculate the mean escape time for every stagnant part of the structure with $\phi_o = 0.582$ and $\phi_o = 0.232$[11]. The resulting (logarithmized)

[10]The robustness was checked by varying the threshold by a factor of two which resulted only in very small changes in the size of the stagnant regions.

[11]The values of equation (7.2) were validated by numerical simulation where we released diffusing

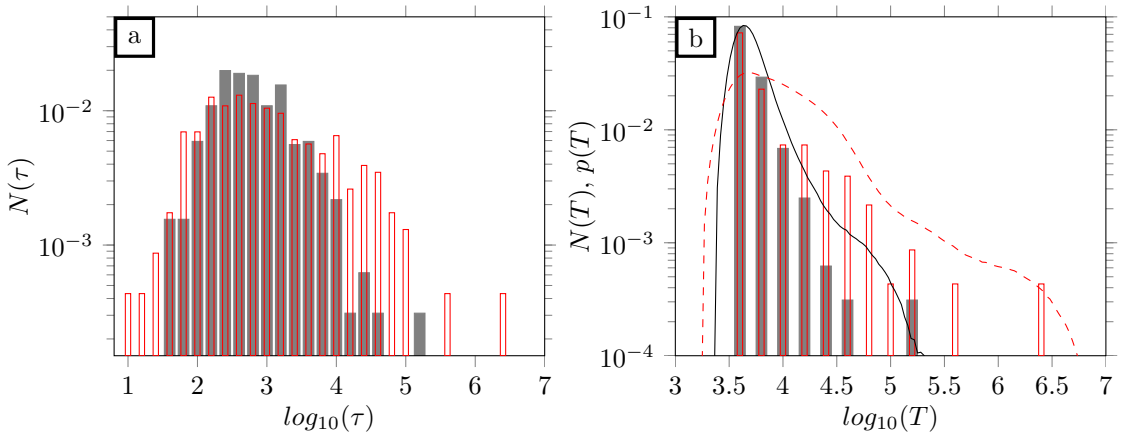

Figure 7.6.: (a) Calculated mean escape time distributions of the stagnant parts for the structure with $\phi_o = 0.582$ (gray bars) and $\phi_o = 0.232$ (red bars). After adding a mean advection time τ_A to every mean escape time, a theoretical FPTD results for both structures. For comparison, the measured FPTD for $Pe = 128$ of both structures are also shown as black solid line for $\phi_o = 0.582$ and as red dashed line in case of $\phi_o = 0.232$. The agreement between largest measured and calculated times is remarkable.

distribution of mean escape times $N(\tau)$ of colloidal particles in the stagnant areas of our samples are shown in figure 7.6 (a). The grey bars belong to $\phi_o = 0.582$ and the red bars belong to $\phi_o = 0.232$. It can clearly be seen that the stagnant parts of the structure with $\phi_o = 0.232$ have a higher mean escape time and, more importantly, the maximum times are about an order of magnitude larger than for the structure with $\phi_o = 0.582$. Now, with this information we are already able to understand, on a quantitative basis, the extent of the long-time tails of the two structures. The large number of stagnant parts with low escape times is not of great importance since the time scale of the largest stagnant parts is markedly larger and, thus, dominates in the long-time tail[12]. The maximum times for the FPTD of about $10^{5.2}\,s$ and $10^{6.4}\,s$ of each structure are in very good agreement with the largest mean escape times of the corresponding stagnant areas. This already points to the relevance of trapping events for the transit time of particles in low-porosity structures.

The raw distribution of mean escape times, of course, does not capture the full transport process of the particles in the structure, because the actual advection of the particle, i.e., the time it takes a particle to flow through the structure without being trapped, has been neglected so far. For a very simple calculation of a FPTD including the diffusion inside the stagnant parts and the advection along the flowing parts of the structure, we simply added a typical advection time τ_A (see definition of the Pe), which is just the

particles at random positions within stagnant parts and calculated their mean escape times. For large stagnant areas only small deviations were found. In case of smaller areas, where the equation might not be applicable, the deviations were sometimes larger, but these small stagnant areas have a small effect on the total retention times of the particles and are not important for our findings.

[12]Remember that the mean escape times were logarithmized for the shown distributions, i.e., one event on the right end of the distribution can make up for many events on the left end.

time a particle needs to travel through the structure[13], to each mean escape time and get new calculated distributions which are shown as gray and red bars in figure 7.6 (b). For a comparison we also included the measured FPTD for $Pe = 128$ of both structures taken from figure 7.4 (d) and (e) as solid black and dotted red lines.

Although the calculated and measured FPTD evidently do not collapse onto each other, again, the main point to realize is that the largest values in both distributions are almost identical. Such a good agreement is remarkable given the simplicity of our model and the width of the retention time distributions. The good accordance also suggests that thinking in terms of two competing processes, namely flow independent diffusion in stagnant parts and flow dependent advection, is well justified. One should also understand that the sharp bars of the calculated FPTD must not be understood as sharp values, because they only represent mean escape times which cannot be expected to agree better with measured data than their standard deviation, which equals the mean escape time. With this in mind one can even appreciate the fact that the calculated FPTD resembles the measured FPTD to some extent over a larger time range.

Before we close this section we would like to mention some implication for the applicability of the ADE. This topic was also addressed in [131] in some detail yet without discussing the role of the precise geometry of the stagnant parts. Certainly the separation of both time scales, i.e., the advection time τ_A and the diffusion time τ_D that is set by the largest mean escape time, becomes less and less important as Pe is decreased. This can best be understood by contemplating figure 7.4 (d) again. For the highest Pe (black curve) the distribution is strongly asymmetric, because the time it takes a particle to travel through the structure is much smaller than the mean escape time of the large stagnant areas. So, $\tau_A \ll \tau_D$ and clearly the ADE is not applicable. Decreasing the Pe, as discussed before, leaves the long-time tail almost unaffected, but as τ_A increases and, therefore, approaches τ_D more and more, the distribution becomes more symmetric resembling the distributions of the low-porosity structure in figure 7.4 (b). Once $\tau_A \gg \tau_D$ the distribution will be in agreement with the ADE. This, however, would occur at extremely low flow rates[14] for our low-porosity structures and might in many cases of such media be of no practical importance. The fact that the effect of stagnant parts can only be clearly seen if $\tau_A \ll \tau_D$ also implies that the effect of smaller and smaller stagnant areas of the studied structure will show up in the FPTD as the flow rate is increased. In some sense this is similar to the use of particles with high energies to gain information about finer and finer structural features of some piece of matter, although this analogy is a little far-fetched.

[13] Here, we again simplified the process by just adding the same time τ_A, although in reality the advection times of particles are also distributed over a wide range.

[14] Making the sample longer would also result in an increasing τ_A without affecting τ_D. The effect of trapping in stagnant parts could average out in a long sample and lead to a FPTD in agreement with the ADE. In that case the porous medium would be considered homogeneous.

7.4.2. Influence of multiple trapping

During their journey through a low-porosity structure with a large amount of stagnant parts, particles can and often will visit several of such areas. The simple model we used to calculate the FPTDs assumes that particles become trapped only once during their transit and also that trapping in each stagnant part is equally likely which, certainly, is an oversimplification.

Even with our rather simple model we had a good agreement between the calculated and measured FPTD. Especially the longest times that were observed can be explained by this model. For an understanding why this model, despite its seemingly unrealistic assumptions, still gives useful results, we also extracted from the simulated trajectories how often and for how long the particles are trapped in stagnant areas. For the low-porosity structure ($\phi_o = 0.900$) there are no stagnant areas. For the structure with the medium porosity ($\phi_o = 0.582$) multiple trapping of particles occurred relatively rarely. For example, at the highest Péclet number the average number of visited stagnant areas amounted to only $\bar{n} = 0.80$, albeit the structure contains more than 200 stagnant areas. Hence, in case of this structure most of the particles only spend a very short time in stagnant areas with the exception of the largest stagnant parts which then clearly have a huge effect on their retention times. To clarify the role of multiple trapping, we will only study the frequency with which the particles visit stagnant parts for the structure with the lowest porosity ($\phi_o = 0.232$).

The results are shown in figure 7.7. (a) shows the probability distribution of the number of visited stagnant areas n for the simulated trajectories. The black histogram represents the distribution for $Pe = 128$, i.e., a fast flow velocity, and the histogram in cyan corresponds to $Pe = 8$. As can clearly be seen, the mean number of visited stagnant areas and also the maximum number of visited stagnant areas is significantly higher at the lower Pe. This makes sense, because at lower flow rates the particles have more time to diffuse into stagnant areas. The Pe-dependence of $\bar{n}$ is plotted in (b), which displays a sharp and monotonous decrease from $\bar{n} = 10.6$ at $Pe = 8$ to $\bar{n} = 4.4$ at $Pe = 128$. As just explained, particles that travel more slowly are also enabled to sample a larger part of the sample by diffusion and, thus, visit more stagnant areas.

We have seen that the distributions in figure 7.6 of mean residence times of stagnant regions are not uniform. Most of the stagnant parts have very low residence times and can only make a very small contribution to the total retention time of the particles. Yet, a few stagnant areas have very large mean residence times and, ergo, dominate the largest first-passage times. Therefore, it seems reasonably to neglect most of the trapping events in small stagnant areas to calculate a transit time of a particle.

To quantify how dominant single trapping events, i.e., trappings in only one stagnant part, are, we used the simulated trajectories and determined the amount of time the particles spend in every stagnant part of the structure along each trajectory. The probability distribution of the fraction ϵ of the total time in stagnant parts that is spent in the stagnant part with the largest escape time for $Pe = 128$ and first-passage times $T \geq 10^5\, s$ is shown in figure 7.7 (c). The distribution elucidates that for such events in the long-time tail single trapping events in large stagnant areas dominate the overall

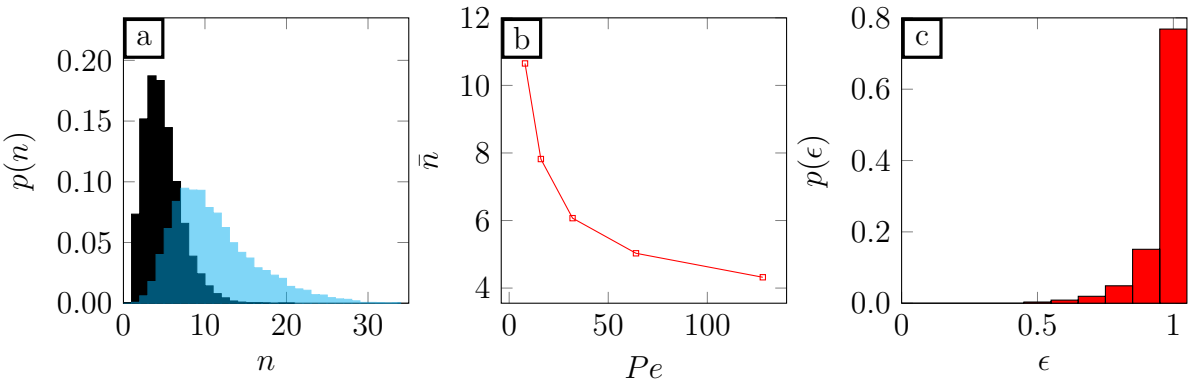

Figure 7.7.: (a) Frequency distribution of number of visited stagnant regions for the low-porosity structure ($\phi = 0.232$) for $Pe = 128$ (black) and $Pe = 8$ (cyan). More stagnant parts are visited at lower flow rates. (b) Average number of visited stagnant parts $\bar{n}$ vs. Pe. At lower Pe the particles have more time to diffuse into stagnant areas. (c) Fraction of time spent in largest stagnant parts for $Pe = 128$. Obviously single trapping events dominate the total time spent in stagnant areas.

residence time[15]. In other words, the transit times of the slowest trajectories, that is, the events in the long-time tails, can be fully explained by single trapping events in large stagnant areas. Given this information our simple model seems to be very sensible when it comes to an interpretation of the events in the long-time tail of the FPTD.

Since the calculated values for the mean escape times of the largest stagnant areas according to equation (7.2) are in good agreement with the largest first-passage times we observe in the measured FPTD, information about the presence and extent of stagnant parts can be gathered from it. Especially in combination with other methods like capillary pressure measurements or adsorption-desorption experiments, FPTDs can deliver information about the microscopic structure of porous media that can lead to useful prediction about, e.g., the amount of trapped liquid in a porous formation.

We conclude this section with a few comments about the Péclet number, which measures the relative importance of advection and diffusion for the underlying transport process. In the commonly used definition of the Péclet number, the one we also used, the characteristic length is assumed to be the grain diameter [3]. In our measurements the calculated Péclet number was substantially larger than unity, so that, solely by this measure, we would expect the transport to be dominated by advection. This, however, is only true for the low-porosity structure with $\phi = 0.900$, where stagnant parts are not present and the particle transport is determined by advection, which is revealed by the FPTDs shifting without changing their shape, when Pe is changed. In case of the structures with lower porosities we found that a large number of particles are temporarily trapped in stagnant parts and spend a long time diffusing in these regions until they escape again. For these structures the FPTDs do not just shift, if the Pe is changed,

[15]This domination of single trapping events is also valid over the whole range of first-passage times with the mean value of ϵ amounting to about 0.8.

but the long-time tails persist independently of the Pe[16], which means that albeit the Pe is high, the transport is still not dominated by advection. An idea for a definition of the Péclet number for the first-passage processes we studied would be to use the largest mean escape time given by equation (7.2) to give the time scale for transport by diffusion and the mean advection time $\tau_{adv} = L/U$ for transport by advection. This number would directly compare the important time scales for diffusive and advective transport in a porous structure and indicate the dominating transport mechanism.

7.5. Dispersion of active particles

Up to this point we have only studied the transport of passive tracer particles in a porous structure. Yet, in nature and in many technical applications the transport of active particles, that is, particles that have some means of self-propulsion, which allows them to move through the structure in the absence of any external force, are often encountered. Transport of active particles, like bacteria, in porous media is of importance in many different fields, ranging from bioremediation, groundwater contamination and enhanced oil recovery to blood perfusion inside the body [137, 138, 139].

We study the motion of active particles in our artificially created low-porosity structure ($\phi_o = 0.232$) by basically the same semi-experimental approach that we employed for the passive particles. We will again use the experimentally determined velocity fields to capture the effect of the fluid motion on the particles. The difference now is that we will give each particle a certain self-propulsion velocity V and an angle that is subject to rotational diffusion, i.e., the angle changes in a random non-correlated fashion (see figure 7.8). The active motion of the particles has a pronounced effect on their transport behavior inside porous structures, which will manifest itself in FPTDs that differ substantially from the passive-particle case.

The motion of the active particles is modelled with basically the same equation as before (equation (7.1)). Only an angle and the self-propulsion velocity of the particle are added:

$$\mathbf{r}(t + \Delta t) = \mathbf{r}(t) + c\mathbf{u}(\mathbf{r})\Delta t + \boldsymbol{\xi}(\Delta t) + V\hat{\mathbf{n}}\Delta t, \tag{7.3}$$

$$\phi(t + \Delta t) = \phi(t) + \boldsymbol{\zeta}(\Delta t). \tag{7.4}$$

In addition to the terms we had before, we now have the active velocity term $V\hat{\mathbf{n}}$, where $\hat{\mathbf{n}} = (\sin(\phi(t)), \cos(\phi(t))$ splits the velocity into x and y component. The orientation of the particle is given by the angle ϕ. $\boldsymbol{\zeta}(\Delta t)$ is a Gaussian distribution with zero mean and a mean squared value of $2D_r\Delta t$, where $D_r = k_B T/(8\pi\eta a^3)$ is the rotational diffusion coefficient of the particle. Assuming particles with a diameter of $1\,\mu m$ a rotational diffusion coefficient of $D_r = 1.28\,s^{-1}$ results.

On time scales that are short compared to the rotational time $\tau_r = 1/D_r$ of the particle, the motion is ballistic. This is the major difference between active and passive

[16] At least for our Pe range. Lowering the Pe by a factor of 100 would lead to totally diffusion dominated transport.

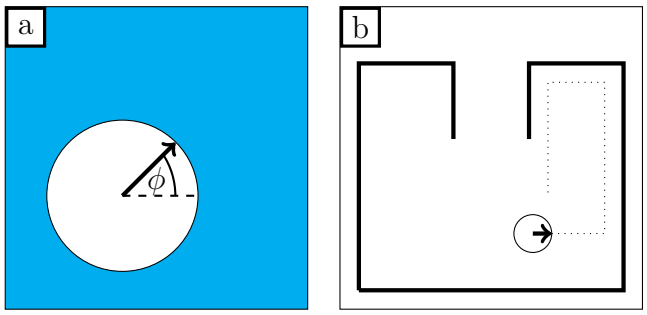

Figure 7.8.: (a) Illustration of an active particle that is swimming in water. The direction of the velocity vector **V** is subject to changes by rotational diffusion. The direction of motion is given by the angle ϕ. (b) One example of a stagnant part that can lead to "active" trapping of particles with a high motility. The particle slides along the boundary and is not be able to escape easily out of such a geometry. The indicated particle trajectory (dotted line) neglects diffusion and is only meant to be illustrative.

particles. In the long-time limit, the motion will show the same characteristics as normal diffusion, i.e., a mean squared displacement that is proportional to time. Hence, a long-time effective diffusion coefficient can be defined by [140]:

$$D_{\text{eff}} = D_{\text{m}} + \frac{V^2}{2D_{\text{r}}}, \tag{7.5}$$

where D_{m} is the diffusion coefficient of the passive particles.

Equations (7.3) and (7.4) were used to simulate the motion through the low-porosity structure ($\phi_0 = 0.232$) for a large number of active particles. The procedure is the same as for the passive particles. The constant c was kept constant in every run and corresponds to $Pe = 128$. The only parameter that was varied is the magnitude of the self-propulsion velocity V. This variation has a substantial effect on the resulting FPTDs which are shown in figure 7.9 (a).

The black line corresponds to the FPTD for passive particles which was also shown in figure 7.4 (f). The other FPTDs belong to active particles with increasing motility, i.e., increasing self-propulsion velocity V. As the particle motility increases the long-time tail gets shorter, i.e., the slowest particles take less time to travel through the structure. On the other hand, the breakthrough times and the maxima of the distributions shift toward higher values, implying that a typical particle takes a longer time to pass through the structure.

The reasons for the distinctive behavior of the active particles compared to the passive ones might seem to be quite obvious, but then again some seemingly sound explanations for their behavior can also run into difficulties. Certainly one simple fact about the active particles is that their long-time translational diffusion coefficient D_{eff} can be orders of magnitude higher than for passive ones, depending on the velocity of the particle and its rotational diffusion coefficient. This alone can in an intuitively simple manner explain why the longest transit times in the FPTDs of active particles are considerably shorter. We calculated the effective diffusion coefficients D_{eff} for every V according to equation

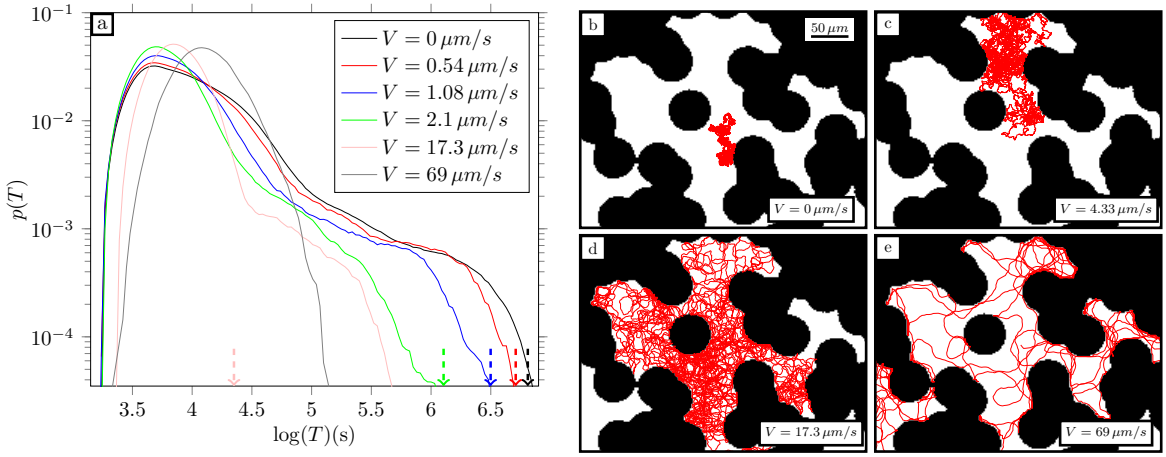

Figure 7.9.: (a) Measured FPTDs in the low-porosity structure ($\phi_o = 0.232$) for active particles with different self-propulsion velocities V. With increasing V the largest transit times become shorter. The breakthrough times and the maximum of the FPTD shift toward longer times. The arrows indicate the expectation for the largest transit times according to the respective effective diffusion constants. Exemplary trajectories for a passive (b) and active particle with increasing motility (c)-(e) in a stagnant area. The higher the motility the larger region during the same time interval is sampled and the higher the probability of presence close to the pore boundary due to sliding along the surface.

(7.5). The values that are obtained by rescaling the largest transit times of the passive particle case (black) are indicated by dashed arrows in figure 7.9. For low motility (red, blue, green) the rescaling describes the decrease in the maximum transit times very well, which shows that dealing with active particles as if they were passive particles with a higher diffusion coefficient makes sense in some regime. Yet, for high motility (pink) this concept does not work, because, to a large extent, a stagnant part loses its meaning, for a highly motile active particle will hardly see any difference between stagnant and flowing areas, if its self-propulsion velocity is a lot higher than the flow velocity. Another intuitively clear point is that active particles sample a larger region during the same time (see figure 7.9 (e)) and can, therefore, escape out of stagnant regions faster than their passive counterparts[17]. This is true for our structures, but it does not have to hold universally, because if the boundary of the exit of a stagnant part is bent inwards, particles with sufficient motility might not be able to leave. A possible geometry for such an active-particle trap is shown in figure 7.8 (b). Particles with high motility are sliding along the wall, so that their velocity vector always strives to be perpendicular to the boundary. In the shown example they will, thus, not be able to leave the confinement, as they are transported back to the inner part of the domain. Such a behavior of active particles in a structured geometry, and in particular in circular pores, has also been demonstrated experimentally [141]. Due to these complications active

[17] By the way, this also implies that active particles enter more stagnant areas, because they can deviate more easily from the streamlines. This arguments explains an increase in the breakthrough time as we will discuss.

particles do not just behave like passive particles with a higher diffusion constant, there are more subtle differences. In contrast to passive particles, an active particle moves ballistically on time scales smaller than the rotational time τ_r and travels a distance $L_\mathrm{p} = \tau_\mathrm{r} V$, the so-called persistence length, during which it does not change its direction significantly, that is, it more or less moves along a straight line. This implies[18] that there are basically two regimes for active particle transport in a porous medium: If the persistence length is a lot smaller than the size of the pores in the porous medium, the active particles will practically behave like passive particles with a higher diffusion coefficient, i.e., they will be found with equal probability at every position in space. If, however, the persistence length is large compared to the pore sizes, the particles will spend most of their time sliding along the pore surfaces, which could also lead to trapping of particles in stagnant areas that could also increase the maximum transit times significantly. As a consequence of this trapping, particles would start to accrue in such stagnant regions. In principle, appropriately designed structures could then also be used to filter out particles of a specific motility. So, simple arguments do not hold generally for any structure. Besides the decrease in the longest transit times we have also seen that the breakthrough time, i.e., the time it takes the fastest particles to cross the whole sample, is higher for active particles. To explain why that is, one only has to think about the fastest passive particles travelling through the structure. These particles just travel along the main paths through the structure, where the flow velocity is highest. An active particle due to its self-propulsion will be able to deviate and, thus, leave such a main path more easily and will therefore travel in slower regions, which in turn decreases their transit times.

In conclusion, the transport of particles in a low-porosity structure is even more complicated when the particles have some means of self-propulsion. Whether the resulting transit times increase or decrease due to the self-propulsion depends on the specific situation. We have seen that self-propulsion can lead to a reduction of the transit times if particles can escape out of stagnant parts faster, because they sample a larger area in the same time. On the other hand, it would also be possible that such active particles become trapped if their motility is so high that they slide along the boundaries and the stagnant parts are bent inwards. The shortest transit times can also be increased when active particles leave the main paths for fluid transport and enter regions where the flow velocity is lower. As mentioned in section 3.3.1 large particles can be excluded from some stagnant parts due to their exclusion from the slowly flowing fluid layers close to the pore surfaces. This effect could also be counteracted by the self-propulsion which would lead to a higher probability of these particles to enter stagnant parts that would also slow down their transport.

[18] The implications are a little complicated, because it is not only the size of the pores but also their shape and especially their curvature.

8. Conclusion and outlook

Finally the time has come to give the reader the elevator pitch distilling the most important findings into a few sentences. The general topic of this work can be summed up in one sentence: This thesis is about the effect of the pore geometry of porous media on their flow and transport properties. A good understanding of the relation between pore geometry and these properties is indispensable for biological, technical, chemical, agricultural and many other problems that depend on a fluid that is flowing through a complicated environment.

Since the structure of naturally occurring porous media is neither known completely nor easily adjustable, we use soft lithography to artificially create porous structures with fully-known and arbitrary geometry. Aqueous colloidal suspensions are used to, on one hand, visualize and quantitatively determine the fluid velocity field, but, on the other hand, also to directly study the transport properties of the suspended colloidal particles.

The individual particles in our samples are advected by the surrounding flow. Individual particles are traced by video microscopy during their journey through the porous medium which allows a reconstruction of the particle trajectories. The resulting trajectories can be used to determine quantities like local average particle velocities, from which the velocities of the fluid can be deduced. As it turned out, the determination of the fluid velocity field by means of such small dispersed colloids is not as straightforward as it might seem for several reasons: First, the microfluidic cells used in this work are long and flat rectangular channels, which implies that the velocity profile therein is parabolic, i.e., particles at the center of the channel travel faster than particles closer to the top or bottom of it. For particles of the same size but with different densities that are higher than the density of the surrounding fluid, heavier particles will on average be closer to the bottom and, therefore, be advected at different velocities as the lighter ones. Second, any particle of finite size will also act as a moving obstacle, i.e., change the boundary conditions of the surrounding flow. The center of mass velocity, which is the measured variable, will be the result of an averaging process across the particle surface and, thus, will generally not be identical to the fluid velocity at that point. In short, the values for the particle velocities one gets depend on the size and density or, more general, on the particle height distribution of the particles which can also be influenced by, e.g., surface charges.

The goal of one of our studies, namely the experimental determination of the permeability k of porous structures, which involves a measurement of the mean flow velocity through a porous sample, was achieved with the help of a calibration method that employs reference channels of known geometry. The mean fluid velocity in such a channel can be calculated analytically. By also measuring the mean particle velocity in a refer-

ence channel, a proportionality factor between particle and fluid velocity can be obtained. This calibration circumvents the problem of the size-dependent velocity of the particles and allows for a calculation of the mean flow velocity. The calibration factor was used to measure the permeability of the investigated porous structures, which consisted of a number N of randomly placed overlapping circles (ROMC) or ellipses (ROME). Moreover, we measured the permeabilities of structures where the conducting and obstacle phase have been exchanged resulting in structures of conducting circles (EROMC) and ellipses (EROME) that have a very different pore space geometry. The measured permeabilities were complemented by permeabilities obtained by lattice Boltzmann simulations that were in good agreement with the measured data.

The measured permeabilities were in excellent agreement with the values predicted by the well-established Katz-Thompson model (KTM) that relates the permeability to the conductivity and a critical pore diameter l_c (diameter of the largest sphere that can pass through the structure) of the structure. The problem with the KTM is that it does not allow a prediction of the permeability without knowledge of its conductivity. We introduced an expression that uses the Euler characteristic χ_o of the sample-spanning conducting pore space and the number of obstacles N to predict the permeabilities of the investigated structure:

$$\frac{k}{cl_c^2} = \left(\frac{1-\chi_o}{N}\right)^{\alpha}. \tag{8.1}$$

The expression, which can also be understood as an overlapping probability of individual grains, gave very good agreement with the results of the ROMC and ROME structures. The question of the universal applicability of this expression naturally arose.

To make the expression universally applicable, an effective number $\hat{N}$ of obstacles that can be determined from the perimeter, area and Euler characteristic of the pore space, was introduced. After replacing N by $\hat{N}$ in (8.1), the agreement between measured and predicted values for the ROMC and ROME structures was still very good. For the EROME structures an acceptable agreement was found for high porosities, which, however, deteriorated close to the percolation threshold. In case of the EROMC structures the expression did not yield useful values over practically the whole range of porosities. So, the expression does not generally hold for arbitrary structures.

A seemingly reasonable explanation for the deviation is given by the occurrence of very small obstacles in the EROME and EROMC structures, which do not occur in the ROMC and ROME structures. These tiny obstacles might not have a strong influence on the flow properties of the structures, but have a strong effect on the value of $\hat{N}$.

It still remains an obvious objective for the future to find a universal expression that can relate purely geometrical quantifiers to the permeability of an arbitrary porous structure. Possibly, a reconstruction of the considered porous structure by an appropriately chosen Boolean model could provide more universal agreement.

In another set of experiments and simulations the transport properties of small colloids in porous media with varying porosities were studied on an individual particle level

instead of looking at averaged quantities like the permeability. Particles that are transported through a porous medium are advected by the surrounding fluid and also undergo diffusion. Since the fluid velocity field in a porous medium can be highly heterogeneous, particles will travel at different velocities across the sample which can, therefore, give rise to a wide first-passage time distribution (FPTD) of the particles, much wider than would be expected by normal diffusion. The presence of stagnant parts, that is, areas in the medium where the flow velocity is practically zero, can have a huge effect on the resulting FPTDs, as particles can be trapped in such regions for very long times. Our objective was to shed some light on the question how the structure of the porous medium and the FPTDs are related.

We measured the FPTDs by a semi-experimental approach where we first experimentally determined the particle velocity field of three porous structures and then used the velocity fields to perform an overdamped Langevin simulation to get a large number of particle trajectories which allowed us to determine FPTDs. As expected, the FPTDs for a high-porosity structure can all be described by the well-established advection-diffusion equation, which holds for macroscopically homogeneous structures. For low-porosity structures, which also contain stagnant areas, the FPTDs show long-time tails that are independent of the flow rate and can be related to the stagnant parts of the structure. An equation from statistical physics was used to calculate the mean escape time for every stagnant part:

$$\tau = \frac{A}{\pi D_0} \ln\left(\frac{P}{d} + 1\right). \tag{8.2}$$

Here, A is the area of the stagnant part, P its perimeter, and d the size of the small exit pore that connects the stagnant part to the flowing part of the structure.

The longest times that are observed in the FPTDs agree very well with the calculated values for the mean escape times of the largest stagnant areas, which means that information about the presence and extent of stagnant areas can be obtained by looking at the long-time tails in FPTDs.

In addition, we also performed simulations of active particles, i.e., particles that can propel themselves, in a low-porosity structure. The resulting FPTDs were mainly affected in two ways. First, the maximum times compared to the passive particles were lowered, which can, in a certain motility regime, be explained by a higher effective diffusion coefficient for active particles since they sample a larger region during the same time and can, consequently, escape out of stagnant regions faster. Second, for active particles with high motility the shortest times in the FPTDs increased due to their ability to leave the main paths where the fluid flow is fastest and travel along regions with lower flow velocities.

In the future it would also be interesting to investigate transport of active particles in structures with a totally different morphology which could, e.g., lead to a slowing down of their transport by trapping in stagnant parts of a particular geometry. Also a more in-depth study of the detailed motion of the active particles in a porous medium and their probabilities of presence could yield useful information, since active agents, like bacteria, are often used to facilitate bioremediation in complex environments. According

to the given structure the agents properties, such as their motility, could be adjusted to increase their efficiency.

Another idea would be to add an external force to the system that pulls, like gravitation, particles in one direction. In case of passive particles one would expect to see a threshold effect, i.e., particles would only be able to make it through the structure, if a certain flow rate or pressure is reached. When particles additionally have some self-propulsion mechanism they could still cross some critical parts of the structure and be, therefore, transported preferably.

There cannot be any doubt that both the study of the relation between the structure of porous media and their permeability as well as the transport behavior of passive and active particles offers will continue to offer a rich field for decades to come. The facets addressed in this work might indeed have raised more new questions than answered long-standing ones.

A. Appendix

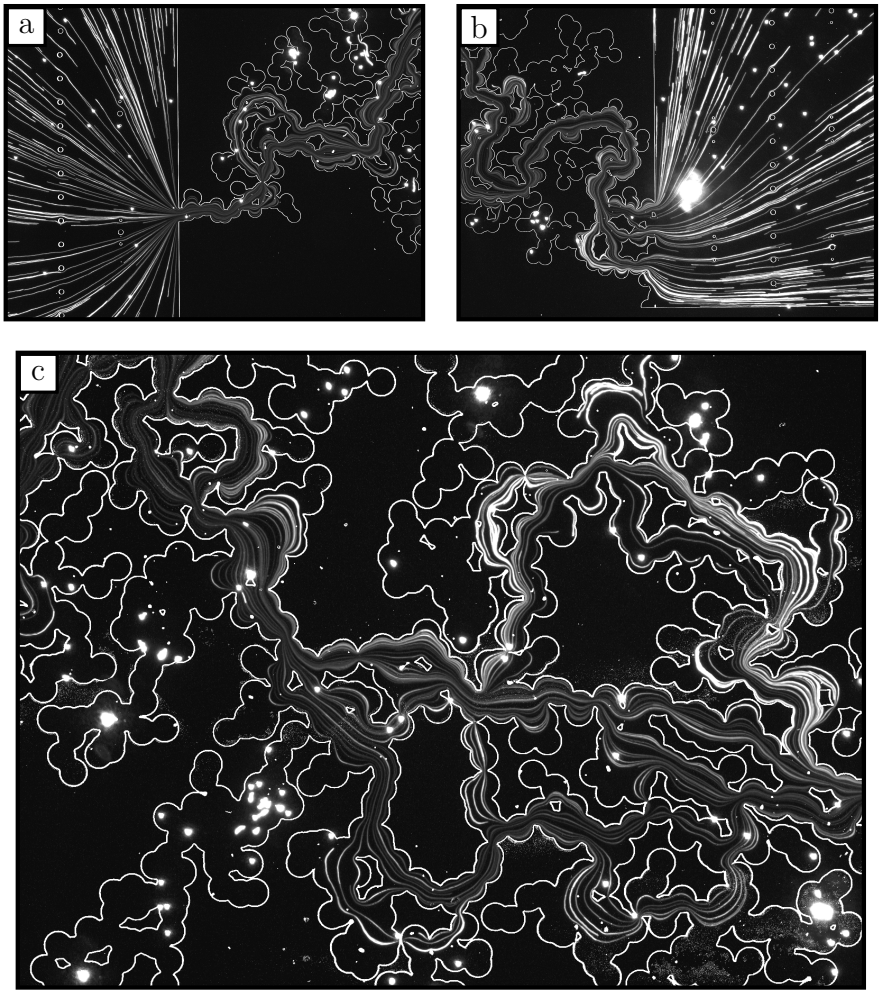

Figure A.1.: Particle streak images of fluorescent particles in a low-porosity EROMC structure with $\phi_o = 0.278$. The images were obtained by using a long exposure time. The particle streaks represent the trajectories of individual particles. The brighter the streaks the slower the particles are at that point. As can be seen at the small entrance (a), the trajectories in the inlet are not moving on parallel trajectories. The same is true on the other side of the structure (b). Inside the porous structure (c) flowing regions and stagnant regions can be distinguished. In stagnant regions particles only diffuse and, thus, show up as bright spots.

Table A.1.: Geometrical and dynamical quantifiers for the investigated structures shown in figure 6.1. D_c and l_c are given in units of lattice sites.

	ϕ	ϕ_o	N	$\hat{N}$	χ_o	D_c	l_c	$k_{exp}/(cl_c^2)$	$k_{sim}/(cl_c^2)$	σ/σ_0
ROMC										
a	0.850	0.850	754	688	-520	100.018	8	0.641	0.6696	0.7031
b	0.701	0.700	1632	1496	-724	51.306	8	0.385	0.3807	0.4405
c	0.551	0.549	2704	2553	-635	21.984	8	0.137	0.1575	0.2107
d	0.418	0.401	3968	3999	-395	11.506	8	0.047	0.0414	0.0764
e	0.365	0.298	4592	4593	-220	2.421	2.421	0.0158	0.0273	0.0118
ROME										
f	0.854	0.850	771	712	-352	67.429	8	0.3598	0.3333	0.3787
g	0.751	0.700	1387	1283	-275	41.254	8	0.118	0.1193	0.1501
h	0.684	0.549	1840	1714	-146	6.275	6.275	0.0385	0.0355	0.0392
i	0.639	0.400	2176	2151	-80	6.245	6.245	0.02	0.0174	0.0133
j	0.651	0.266	2064	2014	-45	5.957	5.957	0.00696	0.0112	0.00851
EROMC										
a	0.851	0.850	8726	2685	-1842	47.97	8	0.304	0.425	0.478
b	0.742	0.700	6174	2600	-1179	35.93	8	0.21	0.132	0.163
c	0.682	0.550	5273	2496	-791	6.05	6.05	0.04	0.034	0.035
d	0.658	0.400	4835	2579	-574	10.72	8	0.0228	0.021	0.026
e	0.668	0.278	5017	2547	-378	5.85	5.85	0.016	0.019	0.0123
EROME										
f	0.850	0.850	9095	11941	-8657	27.66	8	0.7416	0.536	0.6388
g	0.701	0.700	5822	13310	-6348	21.54	8	0.186	0.297	0.3779
h	0.551	0.549	3882	13811	-3865	18.29	8	0.0964	0.131	0.1724
i	0.417	0.400	2602	13586	-1793	12.91	8	0.044	0.049	0.0636
j	0.388	0.270	2405	13382	-1406	13.73	8	0.0111	0.017	0.0227

Bibliography

[1] J. Bear, *Dynamics of fluids in porous media*. Courier Dover Publications, 2013.

[2] F. A. Dullien, *Porous media: fluid transport and pore structure*. Academic press, 1991.

[3] M. Sahimi, *Flow and transport in porous media and fractured rock: from classical methods to modern approaches*. John Wiley & Sons, 2012.

[4] A. Hunt and R. Ewing, *Percolation theory for flow in porous media*, vol. 771. Springer, 2009.

[5] A. Katz and A. Thompson, "Fractal sandstone pores: implications for conductivity and pore formation," *Physical Review Letters*, vol. 54, no. 12, p. 1325, 1985.

[6] D. Avnir, D. Farin, and P. Pfeifer, "Surface geometric irregularity of particulate materials: the fractal approach," *Journal of Colloid and Interface Science*, vol. 103, no. 1, pp. 112–123, 1985.

[7] R. E. Collins, "Flow of fluids through porous media," *Reinhold, New York*, p. 59, 1961.

[8] P. Spanne, J. Thovert, C. Jacquin, W. Lindquist, K. Jones, and P. Adler, "Synchrotron computed microtomography of porous media: topology and transports," *Physical Review Letters*, vol. 73, no. 14, p. 2001, 1994.

[9] M. A. Knackstedt, A. P. Sheppard, and M. Sahimi, "Pore network modelling of two-phase flow in porous rock: the effect of correlated heterogeneity," *Advances in Water Resources*, vol. 24, no. 3, pp. 257–277, 2001.

[10] H. Ritter and L. Drake, "Pressure porosimeter and determination of complete macropore-size distributions. pressure porosimeter and determination of complete macropore-size distributions," *Industrial & Engineering Chemistry Analytical Edition*, vol. 17, no. 12, pp. 782–786, 1945.

[11] P. De Gennes and E. Guyon, "Lois générales pour linjection dun fluide dans un milieu poreux aléatoire," *J. Mec*, vol. 17, no. 3, pp. 403–432, 1978.

[12] H. Meyer, "Pore distribution in porous media," *Journal of Applied Physics*, vol. 24, no. 5, pp. 510–512, 1953.

[13] I. Chatzis, F. Dullien, *et al.*, "Modelling pore structure by 2-d and 3-d networks with applicationto sandstones," *Journal of Canadian Petroleum Technology*, vol. 16, no. 01, 1977.

[14] R. Larson, L. Scriven, and H. Davis, "Percolation theory of residual phases in porous media," 1977.

[15] J. N. Roberts and L. M. Schwartz, "Grain consolidation and electrical conductivity in porous media," *Physical review B*, vol. 31, no. 9, p. 5990, 1985.

[16] J. Bernal and J. Mason, "Packing of spheres: co-ordination of randomly packed spheres," 1960.

[17] M. Patsoules and J. Cripps, "A quantitative analysis of chalk pore geometry using resin casts," *Energy Sources*, vol. 7, no. 1, pp. 15–31, 1983.

[18] V. Schmidt, "The role of secondary porosity in the course of sandstone diagenesis," 1979.

[19] W. C. Krumbein and L. L. Sloss, "Stratigraphy and sedimentation," *Soil Science*, vol. 71, no. 5, p. 401, 1951.

[20] D. K. Todd, "Ground water hydrology, 336," 1959.

[21] R. DeHoff, E. Aigeltinger, and K. Craig, "Experimental determination of the topological properties of three-dimensional microstructures," *Journal of microscopy*, vol. 95, no. 1, pp. 69–91, 1972.

[22] C. D. Tsakiroglou and A. C. Payatakes, "Characterization of the pore structure of reservoir rocks with the aid of serial sectioning analysis, mercury porosimetry and network simulation," *Advances in Water Resources*, vol. 23, no. 7, pp. 773–789, 2000.

[23] C. Lin and M. Cohen, "Quantitative methods for microgeometric modeling," *Journal of Applied Physics*, vol. 53, no. 6, pp. 4152–4165, 1982.

[24] I. Fatt *et al.*, "The network model of porous media," 1956.

[25] N. Wardlaw and J. Cassan, "Estimation of recovery efficiency by visual observation of pore systems in reservoir rocks," *Bulletin of Canadian Petroleum Geology*, vol. 26, no. 4, pp. 572–585, 1978.

[26] W. G. Dow, "Kerogen studies and geological interpretations," *Journal of Geochemical Exploration*, vol. 7, pp. 79–99, 1977.

[27] A. Koponen, M. Kataja, and J. Timonen, "Permeability and effective porosity of porous media," *Physical Review E*, vol. 56, no. 3, p. 3319, 1997.

[28] E. E. Underwood, "Quantitative stereology," 1970.

[29] P. Alexandroff and D. Gilbert, *Einfachste grundbegriffe der topologie*. Berlin, 1932.

[30] P. Pathak, H. T. Davis, L. Scriven, *et al.*, "Dependence of residual nonwetting liquid on pore topology," in *SPE Annual Technical Conference and Exhibition*, Society of Petroleum Engineers, 1982.

[31] D. Lymberopoulos and A. Payatakes, "Derivation of topological, geometrical, and correlational properties of porous media from pore-chart analysis of serial section data," *Journal of colloid and interface science*, vol. 150, no. 1, pp. 61–80, 1992.

[32] V. Ambegaokar, B. Halperin, and J. Langer, "Hopping conductivity in disordered systems," *Physical review B*, vol. 4, no. 8, p. 2612, 1971.

[33] T. R. Madden, "Random networks and mixing laws," *Geophysics*, vol. 41, no. 6, pp. 1104–1125, 1976.

[34] J. Long and D. M. Billaux, "From field data to fracture network modeling: an example incorporating spatial structure," *Water Resources Research*, vol. 23, no. 7, pp. 1201–1216, 1987.

[35] A. Katz and A. Thompson, "Quantitative prediction of permeability in porous rock," *Physical review B*, vol. 34, no. 11, p. 8179, 1986.

[36] A. Katz and A. Thompson, "Prediction of rock electrical conductivity from mercury injection measurements," *Journal of Geophysical Research: Solid Earth (1978–2012)*, vol. 92, no. B1, pp. 599–607, 1987.

[37] M. Sahimi and S. Mukhopadhyay, "Scaling properties of a percolation model with long-range correlations," *Physical Review E*, vol. 54, no. 4, p. 3870, 1996.

[38] S. P. Friedman and N. A. Seaton, "Critical path analysis of the relationship between permeability and electrical conductivity of three-dimensional pore networks," *Water Resources Research*, vol. 34, no. 7, pp. 1703–1710, 1998.

[39] A. Hunt and T. Skinner, "Longitudinal dispersion of solutes in porous media solely by advection," *Philosophical Magazine*, vol. 88, no. 22, pp. 2921–2944, 2008.

[40] D. Stauffer and A. Aharony, *Introduction to percolation theory*. Taylor and Francis, 1991.

[41] P. J. Flory, "Molecular size distribution in three dimensional polymers. i. gelation1," *Journal of the American Chemical Society*, vol. 63, no. 11, pp. 3083–3090, 1941.

[42] W. H. Stockmayer, "Theory of molecular size distribution and gel formation in branched-chain polymers," *The Journal of Chemical Physics*, vol. 11, no. 2, pp. 45–55, 1943.

[43] S. R. Broadbent and J. M. Hammersley, "Percolation processes," in *Mathematical Proceedings of the Cambridge Philosophical Society*, vol. 53, pp. 629–641, Cambridge Univ Press, 1957.

[44] L. Torelli and A. E. Scheidegger, "Three-dimensional branching-type models of flow through porous media," *Journal of Hydrology*, vol. 15, no. 1, pp. 23–35, 1972.

[45] R. Larson and N. Morrow, "Effects of sample size on capillary pressures in porous media," *Powder technology*, vol. 30, no. 2, pp. 123–138, 1981.

[46] G. Wall and R. Brown, "The determination of pore-size distributions from sorption isotherms and mercury penetration in interconnected pores: The application of percolation theory," *Journal of Colloid and Interface Science*, vol. 82, no. 1, pp. 141–149, 1981.

[47] M. Sahimi, B. D. Hughes, L. Scriven, and H. Ted Davis, "Dispersion in flow through porous mediai. one-phase flow," *Chemical engineering science*, vol. 41, no. 8, pp. 2103–2122, 1986.

[48] M. Sahimi, H. T. Davis, and L. Scriven, "Dispersion in disordered porous media," *Chemical Engineering Communications*, vol. 23, no. 4-6, pp. 329–341, 1983.

[49] E. Charlaix, J. Hulin, and T. Plona, "Experimental study of tracer dispersion in sintered glass porous materials of variable compaction," *Physics of Fluids (1958-1988)*, vol. 30, no. 6, pp. 1690–1698, 1987.

[50] J. Hulin, E. Charlaix, T. Plona, L. Oger, and E. Guyon, "Tracer dispersion in sintered glass beads with a bidisperse size distribution," *AIChE Journal*, vol. 34, no. 4, pp. 610–617, 1988.

[51] E. T. Gawlinski and H. E. Stanley, "Continuum percolation in two dimensions: Monte carlo tests of scaling and universality for non-interacting discs," *Journal of Physics A: Mathematical and General*, vol. 14, no. 8, p. L291, 1981.

[52] H. Wang and S. Shaler, "Computer-simulated three-dimensional microstructure of wood fibre composite materials," *Journal of Pulp and Paper Science*, vol. 24, no. 10, pp. 314–319, 1998.

[53] A. P. Roberts and E. J. Garboczi, "Elastic properties of model porous ceramics," *Journal of the American Ceramic Society*, vol. 83, no. 12, pp. 3041–3048, 2000.

[54] A.-S. Dequiedt, M. Coster, J.-L. Chermant, and D. Jeulin, "Towards a model of concrete mesostructure," *Cement and Concrete Composites*, vol. 23, no. 2, pp. 289–297, 2001.

[55] C. Arns, M. Knackstedt, and K. Mecke, "Reconstructing complex materials via effective grain shapes," *Physical review letters*, vol. 91, no. 21, p. 215506, 2003.

[56] K. Mecke and H. Wagner, "Euler characteristic and related measures for random geometric sets," *Journal of statistical physics*, vol. 64, no. 3-4, pp. 843–850, 1991.

[57] R. Schneider and W. Weil, *Stochastic and integral geometry*. Springer, 2008.

[58] J. Hörrmann, D. Hug, M. Klatt, and K. Mecke, "Minkowski tensor density formulas for boolean models," *Advances in Applied Mathematics*, vol. 55, pp. 48–85, 2014.

[59] Y.-B. Yi and A. Sastry, "Analytical approximation of the two-dimensional percolation threshold for fields of overlapping ellipses," *Physical Review E*, vol. 66, no. 6, p. 066130, 2002.

[60] J. A. Quintanilla and R. M. Ziff, "Asymmetry in the percolation thresholds of fully penetrable disks with two different radii," *Physical Review E*, vol. 76, no. 5, p. 051115, 2007.

[61] R. P. Feynman, R. B. Leighton, and M. Sands, *The Feynman Lectures on Physics, Desktop Edition Volume I*, vol. 1. Basic Books, 2013.

[62] S. Redner, *A guide to first-passage processes*. Cambridge University Press, 2001.

[63] H. Bruus, "Theoretical microfluidics. oxford master series in condensed matter physics," 2008.

[64] R. Doll, R. Peto, J. Boreham, and I. Sutherland, "Mortality in relation to smoking: 50 years' observations on male british doctors," *Bmj*, vol. 328, no. 7455, p. 1519, 2004.

[65] E. M. Purcell, "Life at low reynolds number," *Am. J. Phys*, vol. 45, no. 1, pp. 3–11, 1977.

[66] T. M. Squires and S. R. Quake, "Microfluidics: Fluid physics at the nanoliter scale," *Reviews of modern physics*, vol. 77, no. 3, p. 977, 2005.

[67] H. Darcy, H. Darcy, and H. Darcy, *Les fontaines publiques de la ville de Dijon*. 1856.

[68] S. Whitaker, "Flow in porous media i: A theoretical derivation of darcy's law," *Transport in porous media*, vol. 1, no. 1, pp. 3–25, 1986.

[69] J. Rubinstein and S. Torquato, "Flow in random porous media: mathematical formulation, variational principles, and rigorous bounds," *Journal of fluid mechanics*, vol. 206, pp. 25–46, 1989.

[70] J. Andrade Jr, U. Costa, M. Almeida, H. Makse, and H. Stanley, "Inertial effects on fluid flow through disordered porous media," *Physical Review Letters*, vol. 82, no. 26, p. 5249, 1999.

[71] S. Whitaker, "The forchheimer equation: a theoretical development," *Transport in Porous media*, vol. 25, no. 1, pp. 27–61, 1996.

[72] P. Forchheimer, "Wasserbewegung durch boden," *Z. Ver. Deutsch. Ing*, vol. 45, no. 1782, p. 1788, 1901.

[73] P. Basak, "Non-darcy flow and its implications to seepage problems," *Journal of the irrigation and drainage division*, vol. 103, no. 4, pp. 459–473, 1977.

[74] A. Sangani and A. Acrivos, "Slow flow through a periodic array of spheres," *International Journal of Multiphase Flow*, vol. 8, no. 4, pp. 343–360, 1982.

[75] E. Hinch, "An averaged-equation approach to particle interactions in a fluid suspension," *Journal of Fluid Mechanics*, vol. 83, no. 04, pp. 695–720, 1977.

[76] S. Kim and W. B. Russel, "Modelling of porous media by renormalization of the stokes equations," *Journal of Fluid Mechanics*, vol. 154, pp. 269–286, 1985.

[77] A. Scheidegger, "The physics of flow through porous media," 1974.

[78] Y. Bernabé and C. Bruderer, "Effect of the variance of pore size distribution on the transport properties of heterogeneous networks," *Journal of Geophysical Research: Solid Earth (1978–2012)*, vol. 103, no. B1, pp. 513–525, 1998.

[79] A. Haji-Sheikh and E. Sparrow, "The floating random walk and its application to monte carlo solutions of heat equations," *SIAM Journal on Applied Mathematics*, vol. 14, no. 2, pp. 370–389, 1966.

[80] S. Havlin and D. Ben-Avraham, "Diffusion in disordered media," *Advances in Physics*, vol. 36, no. 6, pp. 695–798, 1987.

[81] L. H. Zheng and Y. C. Chiew, "Computer simulation of diffusion-controlled reactions in dispersions of spherical sinks," *The Journal of chemical physics*, vol. 90, no. 1, pp. 322–327, 1989.

[82] L. M. Schwartz and J. R. Banavar, "Transport properties of disordered continuum systems," *Physical Review B*, vol. 39, no. 16, p. 11965, 1989.

[83] L. Oger, J. Troadec, D. Bideau, J. Dodds, and M. Powell, "Properties of disordered sphere packings i. geometric structure: statistical model, numerical simulations and experimental results," *Powder technology*, vol. 46, no. 2, pp. 121–131, 1986.

[84] A. Hunt, T. Skinner, R. Ewing, and B. Ghanbarian-Alavijeh, "Dispersion of solutes in porous media," *The European Physical Journal B-Condensed Matter and Complex Systems*, vol. 80, no. 4, pp. 411–432, 2011.

[85] J. Fried and M. Combarnous, "Dispersion in porous media," *Adv. Hydrosci*, vol. 7, no. 169, 1971.

[86] L. R. Huang, E. C. Cox, R. H. Austin, and J. C. Sturm, "Continuous particle separation through deterministic lateral displacement," *Science*, vol. 304, no. 5673, pp. 987–990, 2004.

[87] D. W. Inglis, J. A. Davis, R. H. Austin, and J. C. Sturm, "Critical particle size for fractionation by deterministic lateral displacement," *Lab on a Chip*, vol. 6, no. 5, pp. 655–658, 2006.

[88] K. Loutherback, J. Puchalla, R. H. Austin, and J. C. Sturm, "Deterministic microfluidic ratchet," *Physical review letters*, vol. 102, no. 4, p. 045301, 2009.

[89] S. Sirivithayapakorn and A. Keller, "Transport of colloids in saturated porous media: A pore-scale observation of the size exclusion effect and colloid acceleration," *Water Resources Research*, vol. 39, no. 4, 2003.

[90] A. Einstein, "Über die von der molekularkinetischen theorie der wärme geforderte bewegung von in ruhenden flüssigkeiten suspendierten teilchen," *Annalen der physik*, vol. 322, no. 8, pp. 549–560, 1905.

[91] A. Griffiths and C. Knowles, "The resistance to the flow of water along a capillary soda-glass tube at low rates of shear," *Proceedings of the Physical Society of London*, vol. 24, no. 1, p. 350, 1911.

[92] G. Taylor, "Dispersion of soluble matter in solvent flowing slowly through a tube," *Proceedings of the Royal Society of London. Series A. Mathematical and Physical Sciences*, vol. 219, no. 1137, pp. 186–203, 1953.

[93] R. Aris, "On the dispersion of a solute in a fluid flowing through a tube," *Proceedings of the Royal Society of London. Series A. Mathematical and Physical Sciences*, vol. 235, no. 1200, pp. 67–77, 1956.

[94] T. Perkins, O. Johnston, *et al.*, "A review of diffusion and dispersion in porous media," *Society of Petroleum Engineers Journal*, vol. 3, no. 01, pp. 70–84, 1963.

[95] S. Silliman and E. Simpson, "Laboratory evidence of the scale effect in dispersion of solutes in porous media," *Water Resources Research*, vol. 23, no. 8, pp. 1667–1673, 1987.

[96] M. Levy and B. Berkowitz, "Measurement and analysis of non-fickian dispersion in heterogeneous porous media," *Journal of contaminant hydrology*, vol. 64, no. 3, pp. 203–226, 2003.

[97] A. Arya, T. Hewett, R. Larson, and L. Lake, "Dispersion and reservoir heterogeneity," *SPE Reservoir Engineering*, vol. 3, no. 1, pp. 139–148, 1988.

[98] B. Berkowitz and H. Scher, "Theory of anomalous chemical transport in random fracture networks," *Physical Review E*, vol. 57, no. 5, p. 5858, 1998.

[99] X. Zhang and M. Lv, "Persistence of anomalous dispersion in uniform porous media demonstrated by pore-scale simulations," *Water Resources Research*, vol. 43, no. 7, 2007.

[100] K. Coats and B. Smith, "Dead-end pore volume and dispersion in porous media," *Old SPE Journal*, vol. 4, no. 1, pp. 73–84, 1964.

[101] L. Baker, "Effects of dispersion and dead-end pore volume in miscible flooding," *Old SPE Journal*, vol. 17, no. 3, pp. 219–227, 1977.

[102] H. Deans, "A mathematical model for dispersion in the direction of flow in porous media," *Old SPE Journal*, vol. 3, no. 1, pp. 49–52, 1963.

[103] G. Gist, A. Thompson, A. Katz, and R. Higgins, "Hydrodynamic dispersion and pore geometry in consolidated rock," *Physics of Fluids A: Fluid Dynamics*, vol. 2, p. 1533, 1990.

[104] J.-C. Bacri, N. Rakotomalala, and D. Salin, "Anomalous dispersion and finite-size effects in hydrodynamic dispersion," *Physics of Fluids A: Fluid Dynamics*, vol. 2, p. 674, 1990.

[105] J. Happel and H. Brenner, *Low Reynolds number hydrodynamics: with special applications to particulate media*, vol. 1. Springer, 1983.

[106] R. Ghez, "A primer of diffusion problems," 1988.

[107] R. B. Bird, W. E. Stewart, and E. N. Lightfoot, *Transport phenomena*. John Wiley & Sons, 2007.

[108] D. Qin, Y. Xia, J. A. Rogers, R. J. Jackman, X.-M. Zhao, and G. M. Whitesides, "Microfabrication, microstructures and microsystems," in *Microsystem technology in chemistry and life science*, pp. 1–20, Springer, 1998.

[109] Y. Xia and G. M. Whitesides, "Soft lithography," *Annual review of materials science*, vol. 28, no. 1, pp. 153–184, 1998.

[110] R. J. Adrian, "Twenty years of particle image velocimetry," *Experiments in fluids*, vol. 39, no. 2, pp. 159–169, 2005.

[111] A. K. Prasad, "Particle image velocimetry," *CURRENT SCIENCE-BANGALORE-*, vol. 79, no. 1, pp. 51–60, 2000.

[112] A. Melling, "Tracer particles and seeding for particle image velocimetry," *Measurement Science and Technology*, vol. 8, no. 12, p. 1406, 1997.

[113] Y. Stegeman, "Particle tracking velocimetry," 1995.

[114] G. Segre and A. Silberberg, "Behaviour of macroscopic rigid spheres in poiseuille flow part 2. experimental results and interpretation," *Journal of Fluid Mechanics*, vol. 14, no. 01, pp. 136–157, 1962.

[115] D. Oliver, "Influence of particle rotation on radial migration in the poiseuille flow of suspensions," 1962.

[116] P. Saffman, "The lift on a small sphere in a slow shear flow," *Journal of Fluid Mechanics*, vol. 22, no. 02, pp. 385–400, 1965.

[117] R. Lindken, M. Rossi, S. Große, and J. Westerweel, "Micro-particle image velocimetry (μpiv): recent developments, applications, and guidelines," *Lab on a Chip*, vol. 9, no. 17, pp. 2551–2567, 2009.

[118] J. C. Crocker and D. G. Grier, "Methods of digital video microscopy for colloidal studies," *Journal of colloid and interface science*, vol. 179, no. 1, pp. 298–310, 1996.

[119] M. E. Staben, K. P. Galvin, and R. H. Davis, "Low-reynolds-number motion of a heavy sphere between two parallel plane walls," *Chemical engineering science*, vol. 61, no. 6, pp. 1932–1945, 2006.

[120] M. E. Staben and R. H. Davis, "Particle transport in poiseuille flow in narrow channels," *International journal of multiphase flow*, vol. 31, no. 5, pp. 529–547, 2005.

[121] D. Frenkel, "Soft condensed matter," *Physica A: statistical mechanics and its applications*, vol. 313, no. 1, pp. 1–31, 2002.

[122] A. A. Keller and M. Auset, "A review of visualization techniques of biocolloid transport processes at the pore scale under saturated and unsaturated conditions," *Advances in Water Resources*, vol. 30, no. 6, pp. 1392–1407, 2007.

[123] C. Pozrikidis, "The motion of particles in the hele-shaw cell," *Journal of Fluid Mechanics*, vol. 261, pp. 199–222, 1994.

[124] G. E. SCHRÖDER-TURK, S. Kapfer, B. Breidenbach, C. Beisbart, and K. Mecke, "Tensorial minkowski functionals and anisotropy measures for planar patterns," *Journal of microscopy*, vol. 238, no. 1, pp. 57–74, 2010.

[125] P.-E. Danielsson, "Euclidean distance mapping," *Computer Graphics and image processing*, vol. 14, no. 3, pp. 227–248, 1980.

[126] A. Bunde, H. Harder, and S. Havlin, "Nonuniversality of diffusion exponents in percolation systems," *Physical Review B*, vol. 34, no. 5, p. 3540, 1986.

[127] J. Tobochnik, D. Laing, and G. Wilson, "Random-walk calculation of conductivity in continuum percolation," *Physical Review A*, vol. 41, no. 6, p. 3052, 1990.

[128] R. A. Neher, K. Mecke, and H. Wagner, "Topological estimation of percolation thresholds," *Journal of Statistical Mechanics: Theory and Experiment*, vol. 2008, no. 01, p. P01011, 2008.

[129] C. Scholz, "Fluss und transport in mikrofluidischen porösen medien," 2014.

[130] G. Hwang and C. Chao, "Heat transfer measurement and analysis for sintered porous channels," *Journal of heat transfer*, vol. 116, no. 2, pp. 456–464, 1994.

[131] J. Koplik, S. Redner, and D. Wilkinson, "Transport and dispersion in random networks with percolation disorder," *Physical Review A*, vol. 37, no. 7, p. 2619, 1988.

[132] J.-C. Bacri, N. Rakotomalala, and D. Salin, "Experimental evidence of disorder effects in hydrodynamic dispersion," *Physical review letters*, vol. 58, no. 20, p. 2035, 1987.

[133] D. Holcman and Z. Schuss, "Control of flux by narrow passages and hidden targets in cellular biology," *Reports on Progress in Physics*, vol. 76, no. 7, p. 074601, 2013.

[134] D. Holcman and Z. Schuss, "Escape through a small opening: receptor trafficking in a synaptic membrane," *Journal of Statistical Physics*, vol. 117, no. 5-6, pp. 975–1014, 2004.

[135] O. Bénichou and R. Voituriez, "Narrow-escape time problem: Time needed for a particle to exit a confining domain through a small window," *Physical review letters*, vol. 100, no. 16, p. 168105, 2008.

[136] Z. Schuss, A. Singer, and D. Holcman, "The narrow escape problem for diffusion in cellular microdomains," *Proceedings of the National Academy of Sciences*, vol. 104, no. 41, pp. 16098–16103, 2007.

[137] P. Reynolds, P. Sharma, G. Jenneman, and M. McInerney, "Mechanisms of microbial movement in subsurface materials.," *Applied and environmental microbiology*, vol. 55, no. 9, pp. 2280–2286, 1989.

[138] H. Lappin-Scott, F. Cusack, and J. Costerton, "Nutrient resuscitation and growth of starved cells in sandstone cores: a novel approach to enhanced oil recovery," *Applied and environmental microbiology*, vol. 54, no. 6, pp. 1373–1382, 1988.

[139] G. E. Jenneman, M. J. McINERNEY, and R. M. Knapp, "Microbial penetration through nutrient-saturated berea sandstone," *Applied and environmental microbiology*, vol. 50, no. 2, pp. 383–391, 1985.

[140] B. ten Hagen, S. van Teeffelen, and H. Löwen, "Brownian motion of a self-propelled particle," *Journal of Physics: Condensed Matter*, vol. 23, no. 19, p. 194119, 2011.

[141] G. Volpe, I. Buttinoni, D. Vogt, H.-J. Kümmerer, and C. Bechinger, "Microswimmers in patterned environments," *Soft Matter*, vol. 7, no. 19, pp. 8810–8815, 2011.

Acknowledgement

The self-made man as well as the self-made woman in its literal sense is a myth. We all rely on the services, knowledge and the cooperativeness of our fellow men, colleagues and friends, and I am no exception. I also "get by with a little help from my friends". So, this is now the occasion to thank the many people who were indispensable for the completion of my thesis.

First and foremost, I want to thank my knowledgeable and helpful thesis adviser Prof. Clemens Bechinger who has always been an outstanding leader and teacher. Not only did he push my project forward, he also showed me how to best present my results.

I also want to thank Prof. Wolfgang Bolse and Prof. Christian Holm for making my PhD examination a very pleasant experience.

Credits also belong to Christian Scholz for introducing me to all the experimental techniques and for the constant exchange we had during our time as PhD students.

Jakob Mehl served as a first-class office mate and kept boredom out of our office. Thanks, bro.

His successor Celia Lozano also raises the spirit of our work group.

My two next-door neighbors Felix Kümmel and Lamiss Zaidouny need to be acknowledged for constantly "diffusing" into my office.

I also need to thank all the other members of the institute for the good work environment. The list is long and I hope I don't forget anybody: Carmen Groben, Ivo Buttinoni, Giovanni Volpe, Juan Rubén Gomez-Solano, Ulrike Offenbeck, Maria Aristov, Olga Zvyagolskaya, Parmida Shabestary, Uwe Rau, Valentin Blickle, Thorsten Brazda, Christoph July, Kilian Dietrich, Wilhelm Kiefer, Jannick Fischer, Arthur Grupp, Laurent Helden, Daniel Hirneise, Maximilian Mußotter, Hans-Jürgen Kümmerer, Thomas Klumpp, Christa Mayer, Mahsa Sahebdivani, Tobias Bäuerle, and Thomas Bohlein. Thank you all.

Let us also not forget the next generation, our new bachelor and exchange students Alex Blokhuis, Stefan Jesenski, Philipp Konzelmann, Lea Kopf, Jakob Steiner and Moritz Tritschler who bring new life to our working hours.

It has been a pleasure meeting and working with all of you.

On a final note, I want to give thanks to my parents Gabriele and Karl Wirner and to my whole family for always supporting me.

Erklärung

Hiermit erkläre ich, dass ich die vorliegende Arbeit selbständig verfasst und keine anderen als die angegebenen Quellen und Hilfsmittel verwendet habe.

Stuttgart, den 8. März 2015

Frank Wirner